Computational Design and Modeling of Molecular Organic Semiconductors for Solar Cell and Lighting Applications

by

Xiao Ma

A dissertation submitted in partial fulfillment
of the requirements for the degree of
Doctor of Philosophy
(Materials Science and Engineering)
in The University of Michigan
2015

Dissertation Committee:

Professor John Kieffer, Chair
Associate Professor Jinsang Kim
Assistant Professor Emmanouil (Manos) Kioupakis
Assistant Professor Paul Zimmerman

© Xiao Ma

2015

Acknowledgements

This is for the many people who helped and supported me in the pursuit of knowledge, and this thesis: Dr. Kieffer, my advisor and mentor, introducing me to computational materials with great patience and support; my parents and my girlfriend, Mo Chen, for always believing in me and backing me up; my friend and colleague, Dr. Changgua Zhen, Dr. Hossein Hashemi, Dr. Arun Kumar Upadayay, Dr. Chen Shao, Ms. Katherine Sebeck for their selfless research help and valuable suggestions.

Table of Contents

List of figures

List of tables

List of appendices

Abstract

In this thesis, we study the optoelectronic properties, including energy levels, charge transport, and optical emission, of organic semiconductors by computational methods.

By functionalizing octasilsesquioxanes (SQ_8) with pentacene, we construct two organic-inorganic hybrid molecules, i.e. dipentacene-SQ_8 and monopentacene-SQ_8. Unlike the herringbone pattern in crystalline pentacene, the pentacene segments in the predicted crystal structures of the hybrid molecules assume parallel configurations, leading to enhanced orbital overlap between pentacene segments. A multi-scale hopping model based on Fermi's golden rule is developed to simulate the charge transport in these crystals. The simulated hole mobility in crystalline dipentacene-SQ_8 can be as high as 11775 cm^2/Vs at room temperature, compared to 17 cm^2/Vs for crystalline pentacene.

We use density functional theory (DFT) to identify design principles for energy level tuning in donor/acceptor conjugated polymers (CPs). We observe that increasing the electron withdrawing strength of the acceptor unit for a given donor drops the lowest unoccupied molecular orbital (LUMO) level, but keeps the highest occupied molecular orbital (HOMO) level almost unchanged. Conversely, increasing the electron donating strength of the donor unit for a given acceptor raises the HOMO level while keeping the LUMO level unchanged. We identify strong correlations between the frontier orbital

energy levels, the amount of charge transfer between the donating and accepting units and the degree orbital localization in CPs.

We investigate the influence of the conjugation length of organic molecules on phosphorescence. In experiments phosphorescence efficiency decreases as the conjugation length increases. Our time-dependent density functional theory (TDDFT) calculations reveal that the intersystem crossing (ISC) rate between first singlet (S_1) and first triplet (T_1) is reduced when increasing the conjugation length. Molecular orbital analysis shows that singlets are more localized than triplets over the conjugation backbone. This results in a larger spatial separation between singlets and triplets when increasing the conjugation length, leading to diminished ISC efficiency and eventually reduced phosphorescence.

These discoveries help us identify the underlying design principles of organic semiconductors, thus enhancing the efficiency of new material development.

Chapter 1. Characteristics of organic semiconductors

1.1. Introduction

Organic semiconductors have been of great interest for the past half a century.[1] Using organic semiconductors in place of silicon-based semiconductors is motivated by obtaining a unique combination of properties: ease of fabrication, flexibility, tunability, lightweight, and the possibility of large surface coverage.[2,3] Unlike conventional inorganic semiconductors, which involve a continuous configuration of covalent bonds between neighboring atoms, organic semiconductors assemble into extended structures based on weak van der Waals forces between molecules.[4] These weak intermolecular forces allow for the fabrication of flexible organic semiconductor films. To achieve similar flexibility with conventional inorganic semiconductors, they would have to be fabricated with sub-micron thickness, which is significantly more costly. As with conventional inorganic semiconductors, the performance of organic semiconductors depends on the long-range molecular order and the degree of crystallinity they possess. For example, in organic photovoltaics (OPV) applications, a P3HT polymer with a higher degree of self-organizing and order is believed to bear a larger quantum efficiency as a result of increasing carrier mobility,[5] while in other cases, like organic light-emitting diode (OLED), ordered π-π stacking results in low quantum efficiency because of self-quenching.[6] Thus, it is critical to understand how to control the molecular arrangements during growth on a substrate or precipitation from solution.

By their mere nature, organic molecules can easily be modified through specific functionalization to obtain desired properties. For instance, researchers use electron-donating and electron-accepting groups to alter the energy levels and spatial location of the corresponding frontier orbitals of the highest occupied molecular orbital (HOMO) and lowest unoccupied molecular orbital (LUMO) of the organic molecule, and thereby tune the optical band gap (i.e., the energy gap between HOMO and LUMO levels) of the material and achieve functional compatibility with other device components.[7] A series of recent studies demonstrate that adding bromide (Br) and carbonyl (CHO) to the aromatic ring of conjugated oligomers leads to systems rich with opportunity for investigating metal-free phosphorescent materials.[8-10] Subtle changes in chemistry and molecular structure of organic materials can induce significant variation in chemical, electrical and optical properties. In that regard, organic semiconductors offer an infinite variety of functionalities by engineering the design of the molecular structures.

Different organic semiconductor materials systems are actively being investigated. On the one hand, the research is motivated by the fact that the performance of many organic semiconductors is significantly below that of their inorganic counterparts. For example, the maximum power conversion efficiency of OPV is in the range of 10%-15%,[11] while inorganic photovoltaics recently achieved as much as 44.7% efficiency.[12] The dramatic improvement of OPV performance depends on the development of new materials, e.g. small optical energy gap[13] and highly conductive materials,[14] and the growing understanding of OPV device operation. On the other hand, the effort is driven by the challenges of upgrading experimental techniques and computational models to address new questions related to the intrinsic properties of organic semiconductors. For example,

the molecular mechanism of singlet exciton fission is extensively investigated as a means to circumvent the Shockley–Queisser limit in OPV for the recent years.[15-17] The limited understanding of the fission process drives the development of modern techniques for time-resolved spectroscopy, quantum chemistry, and small-molecule device fabrication, as well as the innovation of new organic semiconductors.

As mentioned above, the intrinsic properties of materials play a crucial role in controlling the performance of organic semiconductors. However, experimental investigations are hindered by material instabilities and structural defects (due to environmental conditions and processing methods) that obstruct the measurement and understanding of the intrinsic properties of the organic materials. Moreover, while the flexibility of the synthesis of organic molecules provides infinite possibilities of molecular design, it also brings the challenge of a vast multivariable search in order to achieve the desired properties. Fortunately, in the past five decades, the growing power of computers has sparked the development of methods and code interfaces, enlarging the potential of atomistic simulations to tackle a number of scientific issues. The optoelectronic properties of organic semiconductors are extensively studied by various computational methods, e.g. density functional theory (DFT), molecular dynamics (MD), Monte Carlo method (MC) and so on. Their progressive emergence makes the multivariable search from an entire family of molecular systems more affordable both in time and cost. Above all, computation is now standing alongside theoretical and experimental methods in value. In my thesis research, I explore the efficient strategies for molecule design used in organic semiconductors with the method of computation.

1.2. Organic semiconductor materials and devices

1.2.1. Conjugated materials

Conventionally, organic semiconductor materials can be divided into two major classes: small molecules (usually processed in vacuum) and polymers (usually processed in solution).[18] Their semiconductor properties originate from the conjugated π-electron systems, most commonly seen as rigid aromatic rings. Figure 1.1 shows the commonly used conjugated materials in OPV and OLED devices.

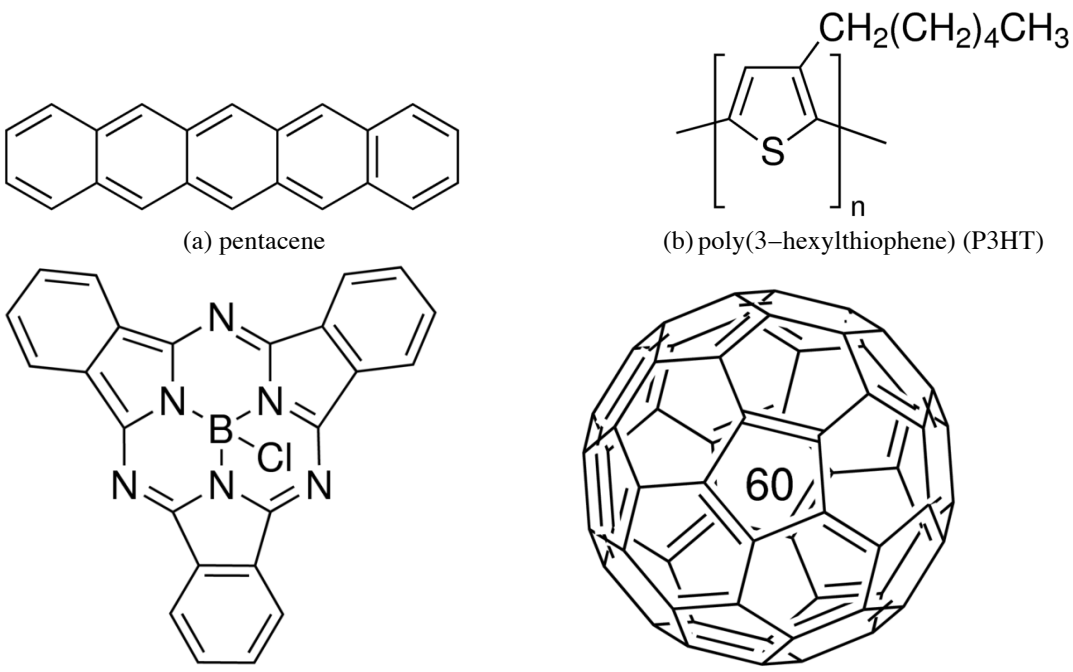

(a) pentacene

(b) poly(3–hexylthiophene) (P3HT)

(c) boron subphthalocyanine chloride (SubPc)

(d) fullerene (C_{60})

Figure 1.1. Typical conjugated materials used in organic semiconductors

In conjugated materials, carbon p_Z orbitals overlap and the π electrons become delocalized on the molecule, forming the so-called π-conjugated system.[19] The backbone of a conjugated material consists of alternating single and double carbon bonds, representing those π electrons. Directional conductivity can be produced along the axis

of the conjugation backbone, e.g. poly(3−hexylthiophene) (P3HT) has theoretically shown excellent intramolecular charge transport property along the backbone.[20] Besides the optoelectronic properties, rigid conjugation systems also play a role in the morphology of a system through π-π stacking interaction. Maximizing π-orbital overlap by reducing the freedom of rotation in the molecules/polymers can induce a densely packed crystal structure with potential face-to-face π-stacking motifs.[21] Eventually, the crystal packing will affect the intermolecular charge transport and hence the bulk electronic properties. For example, the herringbone structure of pentacene single crystal[22] and the lamellar structure of P3HT crystal as a result of π-π stacking,[23] are both well known for their high carrier mobilities. As another consequence of the strong π-π stacking interaction, conjugated systems tend to be insoluble in the majority laboratory solvents.[24] Long and flexible alkyls are conventionally used to enhance the solubility. Overall, the unique electronic properties and the feasibility of chemical modification, as well as the good stability under various substrates facilitate wide application of conjugated materials in organic semiconductors.

1.2.2. Organic photovoltaics

Finding clean and renewable energy in place of the fossil fuel is one of the most important scientific challenges of the 21st century. The abundant availability of sunlight could satisfy any future energy demand, by acquiring power through photovoltaics.

Extensive research on photovoltaic effects in organic materials began in 1950s.[25] In 1975, Tang first presented an OPV device with a single layer of organic materials sandwiched between two metal electrodes of different work functions.[26] However, a

single-layer organic material suffers two major problems: (1) a large electric field is required to overcome the exciton-binding energy, in order to dissociate the exciton, an electron-hole pair bound by Coulomb interaction; (2) both electron and hole travel in the same material after exciton dissociation, leading to a dramatic recombination loss. A bilayer heterojunction OPV was developed by Tang in 1986,[27] and consists of a donor (p-type semiconductor) and an acceptor (n-type semiconductor) organic material. The

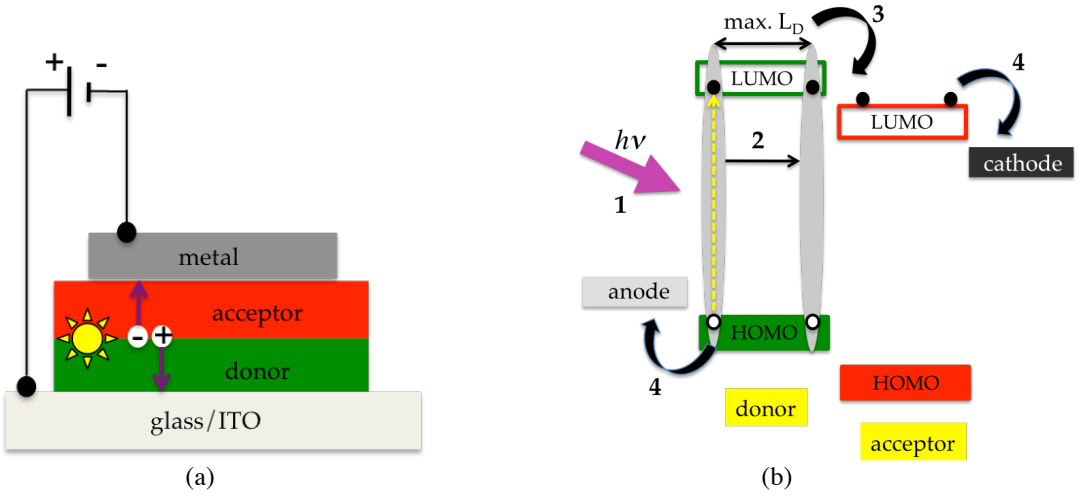

Figure 1.2. (a) Configuration of OPV bilayer heterojunction devices; (b) Fundamental steps occurring in donor–acceptor heterojunction solar cells: 1) Photoexitation of the donor to generate an exciton (electron–hole pair bound by Coulomb interactions). 2) Exciton diffusion to the D–A interface. Excitons that do not reach the interface do not contribute to the photocurrent (longer diffusion length, L_D). 3) Dissociation of bound excitons at the D–A interface to form a geminate electron–hole pair (increased interfacial charge separation requires optimal energy offset between LUMO of the donor and LUMO of the acceptor material). 4) Free charge carrier transport and collection at the external electrodes (require high charge carrier mobility). From Mishra *et al*. (2012)

photogenerated excitons are dissociated at the organic/organic interface, where a built-in electric field is strong enough to overcome the exciton-binding energy, and then free electrons and holes migrate in the separate materials towards the electrodes where they

are collected. Figure 1.2 shows the basic process of photovoltaic effects in a donor-acceptor bilayer heterojunction device.[28] To further improve the performance, multilayer heterojunction devices were invented by adding a few functional layers to facilitate the photovoltaic process, e.g. the Forrest group introduced an exciton-blocking layer to increase the optical intensity at the D-A interface and thereby increase the light absorption efficiency.[29] The major disadvantage of layered OPV devices is the limited D-A interfacial area (photocurrent generation region). Because of the short exciton diffusion length ($L_D \approx$ 5-10 nm) compared with the optical absorption length ($1/\alpha$), characteristic of most organic thin film materials, only excitons generated within a short distance from the interface can dissociate into free carriers and contribute to the photocurrent.[30] Therefore, the thickness of the D-A layers is limited as the same magnitude of exciton diffusion length. Yu *et al*. proposed the concept of "bulk heterojunction" in which a blend of donors and acceptors is used to create interpenetrating phase domains.[31] This approach increases the interfacial area substantially so that excitons have a better chance of diffusing to the interface and dissociating to free carriers, while each phase domain is continuous for carrier transport. The performance of bulk heterojunction OPV depends largely on the carrier mobility and blend morphology.[32]

The power conversion efficiency (PCE) is the most important parameter to measure the quality of an OPV device. The PCE is only 0.001% for the first published OPV device in 1975, and then was further improved to above 1% with the same single-layer sandwich structure.[33] Since the birth of multilayer/bulk heterojunction OPV device, the maximum PCE has exceeded 10%. To evaluate the PCE of a certain OPV device, current-voltage (*J*-*V*) stands as an important characterization method (Figure 1.3). The open-circuit voltage (V_{OC}), short-circuit current density (J_{SC}) and maximum power out ($(V \times J)_{\max}$, the shadow area) under illumination are also illustrated. The fill factor (*FF*) and PCE (η) are defined as

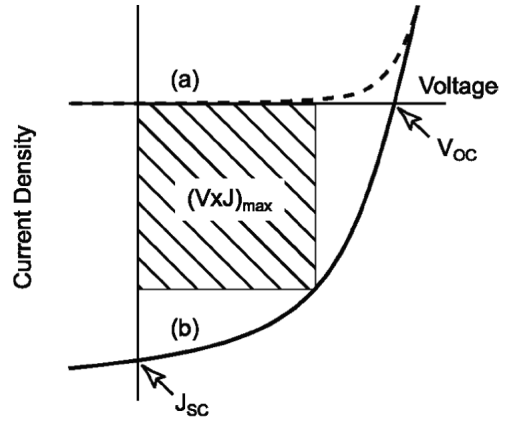

Figure 1.3. Schematic *J*-*V* cure of OPVs: (a) in dark (b) under illumination.

$$FF = \frac{(V \times J)_{\max}}{V_{OC} \times J_{SC}} \tag{1.1}$$

$$\eta = \frac{(V \times J)_{\max}}{P_{in}} = \frac{V_{OC} \times J_{SC} \times FF}{P_{in}} \tag{1.2}$$

where P_{in} is the incident light power. As shown above, PCE is proportional to V_{OC}, J_{SC}, and *FF*.

V_{OC} and J_{SC} represent the maximum photovoltage and photocurrent measured in an OPV device. The magnitude of V_{OC} is confirmed to correlate with the energy difference between the HOMO level of the donor and the LUMO level of the acceptor molecules that form the multilayer or bulk heterojunction.[34] However, the inevitable charge

recombination processes can lower the V_{OC}.[35] J_{SC} can be increased by harvesting more photons within the solar spectrum and enhancing the charge transport properties of organic materials. *FF* depends on the competition between charge recombination and transport. Furthermore, the series resistances significantly influence the *FF*, and should be minimized.[28] Above all, designing high-PCE OPV devices is a multivariable problem, depending on the material's absorptivity, the HOMO and LUMO energy levels, molecular packing, charge transport, material processing and so on.[36] Importantly, optimizing one variable to attempt enhancing any of V_{OC}, J_{SC}, and *FF* may compromise the other two, or even itself, e.g. donor-acceptor conjugated polymers have a relatively low optical band gap that can help absorb more photons thus get a higher J_{SC}, but too strong an acceptor in the polymer's framework can lead to a decreased J_{SC} by deteriorating its hole mobility,[37] or generating an extremely low LUMO that results in poor charge dissociation[38]. Hence, different factors must be carefully manipulated and balanced to reach an optimum state for OPV devices.

Despite the complexity of optimization, there are two major directions in the OPV field: (1) the optical band gaps of organic materials are normally higher than 2 eV, only covering the visible range of the solar spectrum.[39] Smaller band-gap organic materials are in demand to extend absorption to the long wavelength region (600~800 nm); (2) The main drawback of organic materials is the poor charge transport property due to the localized electronic states caused by weak intermolecular interaction. In this respect, novel molecular designs are required to develop organic materials with high carrier mobility.

One of the effective approaches of optical band gap reduction is minimization of bond-length alternation. The underlying mechanism can be explained with the simplest form of conjugated polymer, *trans*-polyacetylene (Figure 1.4).[40] Theoretically, polyacetylene is a metallic conductor if double bonds are delocalized over the conjugation backbone and thus rendering all carbon-carbon bond lengths identical. Based on this principle, two well-known methods have been proposed: (1) transition from aromatic to quinoidal structures, e.g. upon going from the aromatic to the quinoidal state, the band gap of polyisothianaphthene (PITN) is 1 eV lower than that of polythiophene.[41] (2) enlargement of the π systems, e.g. ladder polymer.[42] However, despite the fact that they are very

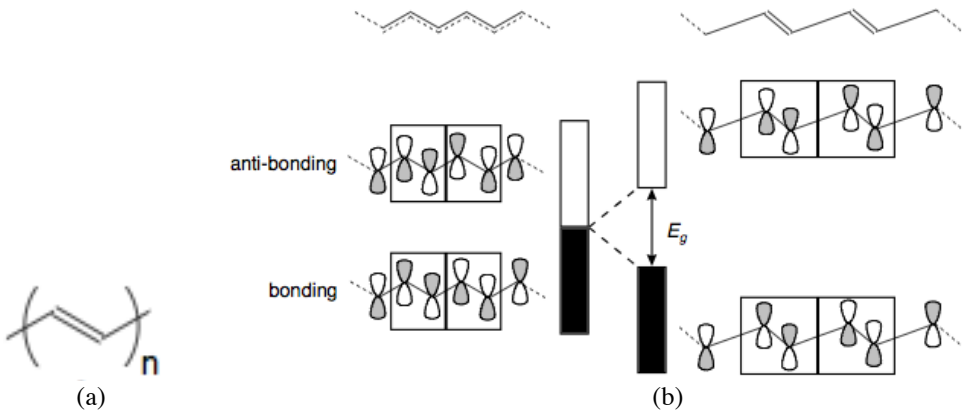

Figure 1.4. (a) Chemical structure of *trans*-polyacetylene (b) Band gap formation by localization of double bonds in *trans*-polyacetylene; (left) the double bonds are delocalized along the polymer chain; finding a band gap as the energy difference between a "bonding" ground state and an "anti-bonding" excited state is impossible due to equivalence (or degeneracy) of both structures for an infinite chain. (right) band gap E_g exists for the two states. From Mullekom *et al*. (2000)

efficient in engineering band gap, both methods have the detrimental drawback of poor synthetic accessibility and pulling up HOMO energy levels (decrease in V_{OC}).

The more successful approach in decreasing optical band gap is incorporating a donor-acceptor strategy. Theoretically, this is due to the reduction of bond-length alternation by

increasing the double-bond character between the repeating units of a CP.[43] The interaction between a strong electron donor (D) and a strong electron acceptor (A) may also give rise to an increased double bond character between these units, since they can accommodate the charges that are associated with such a mesomerism ($D+A \rightarrow D^{+}+A^{-}$).[44] Consequently, a decreased band gap could be obtained in a conjugated polymer with an alternating sequence of the appropriate donor and acceptor units. Figure 1.5 shows the band gap reduction as a result of orbital hybridization from the view of molecular orbital theory.

Although a smaller band gap leads to a red-shifted absorption, which improves light harvesting, it is tricky to determine an ideal band gap. As we mentioned earlier, OPV efficiency is influenced by various factors and simply making the band gap as small as possible will not necessarily guarantee a better OPV device. Moreover, in the field of OLEDs, the goal of obtaining different emission colors will sometimes require a larger band gap.[45] Therefore, instead of band gap minimization, band gap tuning is more practical to obtain desired properties.

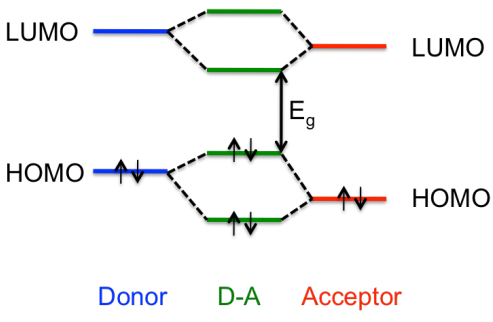

Figure 1.5. Principals of band gap reduction in D-A conjugated polymers explained by molecular orbital theory.

In inorganic materials, charge transport occurs via wave-like propagation of carriers in conduction or valence bands.[1] Mobilities in these materials can exceed 100 cm^2/Vs. Recently, Cheng *et al*. investigated the transport properties of oligoacene crystals in the tight binding approximation.[46] Their studies showed that the mean free path of the charge carriers is smaller than the intermolecular spacing. In light of this

realization, charge transport in organic materials is depicted as a localized phenomenon. The reason for this behavior is that the constituent molecules are weakly bound by van der Waals forces and thus a continuous band structure does not exist. Instead, the hopping model, in which carriers hop between discontinuous localized electronic states, describes the charge transport more accurately.[47] As a result, most organic materials have charge carrier mobilities orders of magnitude lower than inorganic semiconductors. At present, the advancement of acceptor (electron or *n*-type transporting) materials is rather limited (e.g. fullerene derivatives have been the dominant acceptors since 1995[31]), compared to the fast development of a wide range of donor (hole or *p*-type transporting) materials.[28] Therefore the majority of experimental mobilities are measured for hole transporting materials.

One of the major factors influencing charge transport is molecular packing or crystallinity. Generally, highly ordered crystalline systems tend to have outstanding charge transport properties. Apart from the van der Waals forces, the quadrupolar interactions, emerging from the coupling between the permanent quadrupoles of these molecules,[48] also play an important role in configuring the molecular packing. While the van der Waals forces favor the "face-to-face" orientation of the molecules that results in the maximized π–π stacking interaction, the quadrupolar interactions prefer the "edge-to-face" stacking where hydrogen atoms on one molecule encounter the π network of the adjacent molecule.[49] These two competing forces generate a variety of stable packing configurations, leading to polymorphism. The most common crystal form based on the above mechanism is herringbone stacking, such as is observed for crystalline pentacene.[50] Although rarely encountered, co-facial π–π stacking crystal is preferable because the

large orbital overlap facilitates the carrier hopping from one localized state to another and hence promotes the carrier mobility. Studies have shown that various stacking motifs can be realized by tuning the nature, size and position of the substituent on the molecule's conjugation backbone.[51] The actual stacking also depends on the processing environment, e.g. pressure, temperature and film thickness. Due to the flexibility of polymorphism, the difficulties of determining how a molecule will crystallize in the solid state cannot be underestimated. Although scientists have been developing the ability to reliably predict the crystal structure with only the chemical diagram over the last decades, predicted crystal structures for only a limited number of molecules show consistency with the experimental findings, most of them being small molecules with less than 20 atoms.[52] Nevertheless, polymorphism provides enormous opportunities to understand the fundamental mechanism of charge transport in organic materials, and consequently direct the molecular engineering for advanced charge transport materials.

From a computational point of view, single crystals are more attractive than polycrystalline or amorphous materials, because in case of the latter, the intrinsic properties of organic materials are masked by various defects that trap the charge carriers. An accurate insight into the transport process can only be achieved with a good understanding of the correlations between structure and intrinsic properties. The single crystal serves as a model system, where those correlations can be explored.

1.2.3. Organic light emitting diodes

Essentially the reverse to photovoltaics, electroluminescence is a process in which recombination of holes and electrons produces light. Early research of organic

electroluminescence was focused on molecular crystals, since ordered structures present better charge transport properties. One of the first OLED devices was reported by Pope *et al*. who managed to obtain electroluminescence by applying 400 V of operation voltage on anthracene crystal.[53] Due to the impracticality of such a high voltage, organic thin film

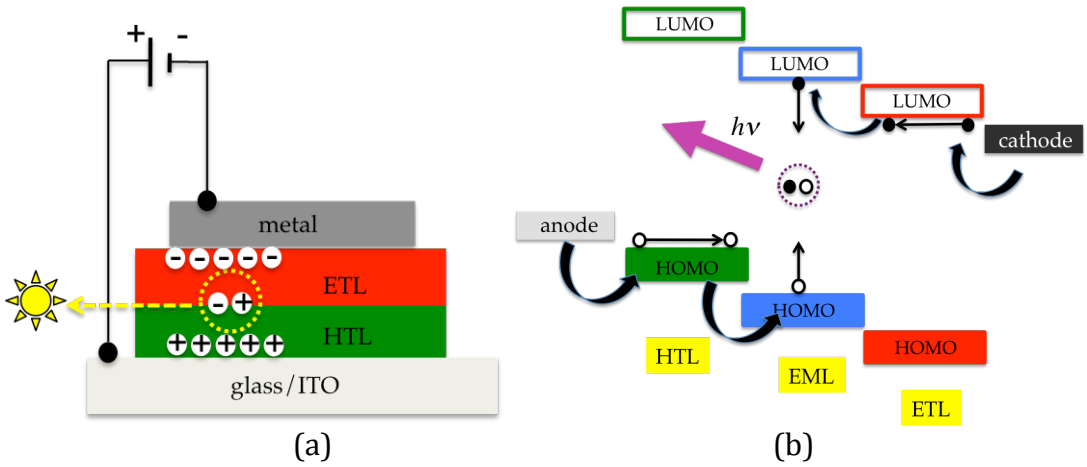

Figure 1.6. ETL: electron transporting layer; HTL: hole transporting layer; EML: emitting layer (a) Configuration of bilayer heterojunction OLED devices. (b) The mechanism of bilayer OLED in a schematic energy level diagram (an EML layer is included). The processes involved in the operation of OLED are charge injection, transport, and recombination to form excitons, and radiative decay of excitons to generate photons. Only escaping photons can be of practical use, while the others are absorbed by the device itself.

of evaporated anthracene was developed to yield fluorescence at 30 V.[54] However, the quantum efficiency of this single-layer device was no more than 0.05%. Tang *et al*. made a substantial improvement with the invention of first multilayer device.[55] Figure 1.6 shows the basic configuration of bilayer heterojunction OLED devices and its operational mechanism. This structure improves the balance of electrons and holes in the emitting zone by transporting electrons in the acceptor materials and holes in the donor materials, and thus enhances the recombination efficiency. In contrast, the previous single-layer device has the detrimental flaw that either electron or hole is the majority charge carrier

while the other is the minority one. Most of the majority charge carriers fail to recombine and migrate to the opposite electrode, resulting in low recombination efficiency.

External quantum efficiency (EQE) is the most important parameter to an OLED device. It is defined as the ratio of the number of photons that manage to escape the device to the number of charge carriers injected into the device. EQE can be expressed as

$$\eta_{EQE} = \gamma\chi\eta_{pl}\eta_{oc} \tag{1.3}$$

where γ is the fraction of electrons and holes that recombine into excitons. This value is always less than 1 because of incomplete recombination caused by the imbalance of electrons and holes. χ represents the fraction of excitons that have the potential to radiatively decay due to selection criteria for electronic transitions in organic semiconductors. η_{pl} is the photoluminescence efficiency, and η_{oc} is the so-called out-coupling efficiency, i.e. the fraction of the number of photons that manage to escape the device to the total number of photons generated.

To enhance the EQE of OLED devices, involves optimizing all the variables mentioned above. First, optimizing the device configuration and the carrier injection/transporting layer can improve γ. For example, by adding hole and electron blocking layers, the injected charge can be prevented from escaping to the adjacent layer, resulting in increased recombination efficiency. Second, η_{oc} is strongly dependent on the optical properties of the organic layers, as well as the electrodes and glass substrate. It can be estimated as $\eta_{oc} = 1 - \sqrt{1 - 1/n^2}$,[56] where n is the refractive index of the emitting layer (n is typically ~1.7-1.8 for organic semiconductors[57]). Hence, using organic materials with

high refractive index can enhance the EQE. Third, in order to improve η_{pl}, bimolecular quenching needs to be reduced.[58] Emitting Molecules carrying large steric groups (e.g. alkane chain) can prevent the aggregation of each other and thus reduce the bimolecular quenching.[59] Lastly, χ depends on the nature of emitting layer, consisting of either phosphorescent or fluorescent materials. Due to spin statistics, electron hole recombination leads to 25% singlet and 75% triplet state population.[60] Normally, in metal-free organic molecules, only fluorescence is achieved, while triplet excitation energy is transferred into heat. This is because a radiative decay for triplet to the ground state is forbidden by spin selection rule. On the other hand, while organometallic compounds with transition metal centers exhibit no fluorescence, through spin orbit coupling (SOC) they exhibit a fast intersystem crossing (ISC) to the lowest triplet state and eventually overcome the aforementioned spin-forbidding decay.[6] Thus, the triplet harvests both singlet and triplet excitation energy and can efficiently emit. In principle, phosphorescence shows a four-time higher χ (100%) than fluorescence (25%). In 1998, Baldo *et al*. reported the first phosphorescent device that in principle could have an internal quantum efficiency (i.e. the fraction of the total number of photons generated to the number of charge carriers injected into the device) of 100%.[61] They utilized the heavy atom Pt to facilitate ISC and supply intense phosphorescence. Other heavy metal atoms, e.g. Ru, Os, Re, Ir and so on, are also commonly used in phosphorescent materials.[6] This phenomenon is called heavy atom effect, by which SOC between the excited electrons and the massive nucleus of the heavy atom is enhanced.[62] The mixing of the singlet and triplet states around the heavy atom promotes ISC.

Recently, Bolton *et al*. reported a purely (metal-free) organic phosphor.[8] They claim that incorporating halogen bonding into the crystals can turn on phosphorescence. The designed compound contains triplet-producing aromatic aldehydes and triplet-promoting bromine, and crystal-state halogen bonding is formed to direct the heavy atom effect to produce efficient solid-state phosphorescence. This finding opens up a new class of purely organic compounds for phosphor design, and ignites further research, both experimentally[9,10] and theoretically[63].

1.3. Computational background and methods

1.3.1. Density functional theory

Solving Schrödinger equation is the most fundamental problem in quantum mechanics, the essence of which lies in how to tackle the many-body/electron problem. Early methods, such as Hartree-Fock (HF), Møller-Plesset perturbation theory and coupled cluster, consider the many-body wavefunction as a core quantity, by which all properties of the system can be determined. However, the complexity of the wavefunction is proportional to the number of electrons N in the system, more specifically, depends on $3N$ spatial variables and N spin variables. This prohibits their applications for large system. In contrast, DFT overcomes this scaling limitation by only considering the total electron density instead of many-body wavefunction, because the electron density is always 3 dimensional. This favorable property makes DFT one of the most popular methods in studying the electronic structure of a range of materials. A short review is given below on the most important theorems of DFT and the Kohn-Sham DFT, the most widely used DFT in organic semiconductor community and this thesis.

The concept of DFT originates from the early work of Thomas and Fermi, who used the electron density in place of the wavefunction. The electron density is defined as

$$\rho(r) = N \int ... \int \left|\Psi(x_1, x_2, ..., x_N)\right|^2 ds_1 dx_2 .. dx_N \tag{1.4}$$

where each electron is defined by its position and spin, i.e. $x = (r,s)$; $\rho(r)$ determines the probability of finding any of the *N* electrons within the volume *r* but with arbitrary spin, while the other *N*–1 electrons have arbitrary positions and spins.

Modern DFT was born in 1964 due to the work by Hohenberg and Kohn. [64] They were able to give two very simple existence theorems, which underpin the whole of current DFT. The first theorem demonstrates that: since the electron density $\rho(r)$ uniquely determines the external potential $v(r)$ and the external potential $v(r)$ determines the Hamiltonian, which in turn determines the ground state wavefunction, the ground state wavefunction must be determined uniquely by the ground state electron density $\rho(r)$. In the original paper, this was proven in a simple but elegant manner by using the principle of *reductio ad absurdum, i.e.* a given assumption generates a contradiction and hence establishing the opposite of the assumption. As a result, we can write the total energy of the system as

$$E(\rho) = T(\rho) + V_{ee}(\rho) + T_{ne}(\rho) = F_{HK}(\rho) + \int \rho(r) v(r) dr \tag{1.5}$$

where $F_{HK}(\rho) = T(\rho) + V_{ee}(\rho)$ is a universal function of ρ describing the kinetic energy $T(\rho)$ and electron-electron interaction $V_{ee}(\rho)$. The second theorem demonstrates that the total energy of the system can be varied according to above equation, with the density

that minimizes the total energy being the exact ground state density. In other words, we can obtain the ground state energy by minimizing the functional in equation 1.5.

The next question was how to obtain $F_{HK}(\rho)$. 1n 1965, Kohn and Sham[65] applied the idea of one electron orbitals and approximated the kinetic energy of the system by the kinetic energy of non-interacting electrons. The celebrated Kohn-Sham equations, in a form of one-electron Schrödinger equation, are as follows

$$\left[-\frac{1}{2}\nabla^2 + v(r) + \int \frac{\rho(r')}{|r-r'|}dr' + v_{xc}(r)\right]\phi_i = \varepsilon\phi_i \tag{1.6}$$

where

$$\rho(r) = \sum_i^N |\phi_i| \tag{1.7}$$

$$v_{xc}(r) = \frac{\delta E_{xc}(\rho)}{\delta\rho(r)} \tag{1.8}$$

The left side of equation 1.6 consists of the kinetic energy of the non-interacting electrons, the external potential, the Hartree potential and exchange-correlation potential, respectively. The relation between the electron density and Kohn-Sham orbitals is shown in equation 1.7. The exchange-correlation potential $v_{xc}(r)$ is defined in equation 1.8, where $E_{xc}(\rho)$ is the exchange-correlation functional. Clearly, the Kohn-Sham equations need be solved by means of an iterative method because of their interdependent nature. This method is commonly known as the self-consistent field (SCF) method.

Before entering SCF iterations to finally solve the Kohn-Sham equations, we must know the exchange-correlation functional. Since the exact form of this functional is not known, various approximations have been developed. One usually splits the exchange-correlation functional into two parts: exchange part and correlation part and approximates them separately

$$E_{xc} = E_x + E_c \tag{1.9}$$

The simplest approximation is called the local density approximation (LDA) where the electron density is assumed to be a homogeneous electron gas. The exchange energy is known analytically and the correlation energy is obtained by fitting to the many-body free electron gas data. In spite of its simple assumption, LDA works surprisingly well with the metal and oxide surfaces. Generalized gradient approximation (GGA) is developed to take into account the inhomogeneities of the electron density. Comparing to LDA, GGA produces better results for many properties, such as gas phase properties of molecules. Another group of exchange-correlation functional is hybrid functionals, which use a fraction of the exact exchange energy from HF theory. Perhaps, the most successful hybrid functional is B3LYP[66] that employs three parameters A, B, C to tune the mixing of HF exchange and DFT exchange and correlation (equation 1.10),

$$E_{xc} = E_{x-LDA} + A(E_{x-HF} - E_{x-LDA}) + B\Delta E_{x-GGA} + C\Delta E_{c-GGA} \tag{1.10}$$

where the three parameters can be determined by means of fitting experimental data. In general, hybrid functionals show improved performance over LDA and GGA functionals, particularly for gas phase properties of molecules and band gaps in solids. In this thesis,

Gaussian09, Dalton2011 and VASP5.0 are the DFT-based simulation packages to calculate the ground state properties of materials.

1.3.2. Time-dependent density functional theory

DFT can only address the ground state or static properties of materials because only time-independent electron densities are considered. In other situations, the electron densities may become time-dependent due to the influence of external source. For example, the optical properties of OLED involve absorption and emission of photons, in which materials are subject to a time-dependent electric field and can undergo electronic excitations and transitions. To obtain the information of time-dependent properties in the frame of DFT, we can utilize time-dependent density function theory (TDDFT) based on response theory, which was established by the Runge-Gross theorem.[67]

In the response theory, the Hamiltonian is expressed as

$$\hat{H}(t) = \hat{H}_0 + \hat{V}(t) \tag{1.11}$$

where $\hat{H}_0$ is the unperturbed part, and $\hat{V}(t)$ is a time-dependent perturbation that can be written as

$$\hat{V}(t) = \int_{-\infty}^{\infty} d\omega \hat{V}^{\omega} \exp(-i\omega + \varepsilon)t \tag{1.12}$$

This perturbation causes the wavefunction to become time-dependent, and it can be expanded in a power series of the perturbation at a finite time t .

$$\begin{aligned}\left|\tilde{0}\right\rangle &= \left|0\right\rangle + \int_{-\infty}^{\infty} d\omega_1 \left|0^{(\omega_1)}\right\rangle \exp\left[(-i\omega_1 + \varepsilon)t\right] \\ &+ \int_{-\infty}^{\infty}\int_{-\infty}^{\infty} d\omega_1 d\omega_2 \left|0^{(\omega_1,\omega_2)}\right\rangle \exp\left[(-i(\omega_1+\omega_2) + 2\varepsilon)t\right] + \ldots\end{aligned} \tag{1.13}$$

The right hand side of the above equation consists of the wavefunction of unperturbed system, the wavefunction linear in the perturbation, the wavefunction quadratic in the perturbation and so on. Also, the expectation value of an arbitrary Hermitian operator $\hat{F}$ performing on a time dependent wavefunction $\left|\tilde{0}\right\rangle$ can be expressed in powers of applied field.

$$\left\langle\tilde{0}\middle|\hat{F}\middle|\tilde{0}\right\rangle = \left\langle 0\middle|\hat{F}\middle|0\right\rangle^{(0)} + \left\langle\tilde{0}\middle|\hat{F}\middle|\tilde{0}\right\rangle^{(1)} + \left\langle\tilde{0}\middle|\hat{F}\middle|\tilde{0}\right\rangle^{(2)} + \ldots \tag{1.14}$$

Substituting equation 1.13 into equation 1.14, the expectation value of the time-dependent operator $\hat{F}$ is obtained as follows

$$\begin{aligned}\left\langle\tilde{0}\middle|\hat{F}\middle|\tilde{0}\right\rangle &= \left\langle 0\middle|\hat{F}\middle|0\right\rangle \\ &+ \int_{-\infty}^{\infty} d\omega_1 \left\langle\left\langle \hat{F};\hat{V}^{\omega_1}\right\rangle\right\rangle_{\omega_1} \exp(-i\omega_1 t) \\ &+ \frac{1}{2}\int_{-\infty}^{\infty} d\omega_1 \int_{-\infty}^{\infty} d\omega_2 \left\langle\left\langle \hat{F};\hat{V}^{\omega_1},\hat{V}^{\omega_2}\right\rangle\right\rangle_{\omega_1\omega_2} \exp\left[-i(\omega_1+\omega_2)t\right] + O(V^3)\end{aligned} \tag{1.15}$$

where the Fourier coefficient $\left\langle\left\langle \hat{F};\hat{V}^{\omega_1}\right\rangle\right\rangle_{\omega_1}$ represents the linear response function with respect to the perturbation $\hat{V}^{\omega_1}$ of frequency ω_1 and $\left\langle\left\langle \hat{F};\hat{V}^{\omega_1},\hat{V}^{\omega_2}\right\rangle\right\rangle_{\omega_1\omega_2}$ represents the quadratic response function with respect to the perturbation $\hat{V}^{\omega_1}$ and $\hat{V}^{\omega_1}$ of frequencies ω_1 and ω_2. The linear response functions can be expressed with eigenfunctions of $\hat{H}_0$ as follows

$$\left\langle\left\langle \hat{F};\hat{V}^{\omega_1} \right\rangle\right\rangle_{\omega_1} = \sum_{k>0}\left(\frac{\langle 0|\hat{F}|k\rangle\langle k|\hat{V}^{\omega_1}|0\rangle}{\omega_1-\omega_k} - \frac{\langle 0|\hat{V}^{\omega_1}|k\rangle\langle k|\hat{F}|0\rangle}{\omega_1+\omega_k}\right), \tag{1.16}$$

where $\omega_1 = \pm\omega_k$ correspond to the excitation energy between states $|0\rangle$ and $|k\rangle$. The residue of equation 1.16 calculates the associated transition moments between the ground state and excited states, as shown in equation 1.17.

$$\lim_{\omega_1 \to \omega_k}(\omega_1-\omega_k)\left\langle\left\langle \hat{F};\hat{V}^{\omega_1} \right\rangle\right\rangle_{\omega_1} = \langle 0|\hat{F}|k\rangle\langle k|\hat{V}^{\omega_1}|0\rangle \tag{1.17}$$

Similarly, the quadratic response function can also be written as

$$\left\langle\left\langle \hat{F};\hat{V}^{\omega_1},\hat{V}^{\omega_2} \right\rangle\right\rangle_{\omega_1\omega_2} = \sum_{k,l>0}\left[\begin{array}{l} \dfrac{\langle 0|F|k\rangle\langle k|V^{\omega_1}-V_0^{\omega_1}|l\rangle\langle l|V^{\omega_2}|0\rangle}{(\omega_1+\omega_2-\omega_k)(\omega_2-\omega_l)} \\ -\dfrac{\langle 0|V^{\omega_k}|k\rangle\langle k|F-F_0|l\rangle\langle l|V^{\omega_2}|0\rangle}{(\omega_1+\omega_k)(\omega_2-\omega_l)} \\ +\dfrac{\langle 0|V^{\omega_1}|k\rangle\langle k|V^{\omega_2}-V_0^{\omega_2}|l\rangle\langle l|V^{\omega_2}|0\rangle}{(\omega_1+\omega_k)(\omega_2+\omega_k+\omega_l)} \end{array}\right] \tag{1.18}$$

Its single residue gives the transition moment induced by spin-orbit coupling when setting $\hat{F} = \hat{\mu}$ and $\hat{V}^{\omega_1} = \hat{H}_{SO}(\omega_1 = 0)$, while its double residue gives the transition moment between excited states. In this thesis, the two DFT packages, Gaussian09 and Dalton2011, are preinstalled with the TDDFT function and used to evaluate the excited state properties of materials.

1.3.3. Molecular dynamics

The MD method is simple in concept, in that it iteratively solves the coupled classical equations of motions (described by Newton's law) of a many-particle system. It starts with a large configuration of atoms and computes the force on each atom. This force is

converted into an acceleration that, by using an explicit finite difference algorithm, can be combined with the current and previous atomic positions and velocities to predict the position of each atom a small time interval (time step) later. Unlike quantum mechanics, the algorithm used in MD can scale linearly with the number of atoms, which makes it feasible to run simulations with millions of atoms by using large multi-processor computers. Using MD simulations, one can compute many quantities that can also be measured experimentally: (1) evolution of the system with temperature and pressure in equilibrium (2) distribution functions (e.g. molecule orientations and atom positions) (3) analysis of dynamics through time-correlation functions. In this thesis, the MD package LAMMPS, is used mainly for sampling atomic trajectories in order to generate distribution function of charge transfer integrals.

1.3.4. Molecular orbital theory

The electronic structure of a molecule can be described by a set of molecular orbitals. According to the approximation of the linear combination of atomic orbitals (LCAO), it is assumed that a certain molecular orbital Ψ_j is a weighted sum of the n constituent atomic orbitals ϕ_i, as shown below

$$\Psi_j = \sum_{i=1}^{n} c_{ij}\phi_i \tag{1.19}$$

where the weights can be determined by substituting this equation into the Schrödinger equation. In a diatomic system, such as two hydrogen atoms, the molecular orbitals are easily written as,

$$\Psi_{\pm} = \phi_{1s}(A) \pm \phi_{1s}(B) \tag{1.20}$$

where A and B designate the two hydrogen atoms. By linearly combining their atomic orbitals, two molecular orbitals are obtained: the bonding orbital (Ψ_+) and the anti-bonding orbital (Ψ_-). Figure 1.7 shows the schematic of molecular orbitals' energy levels. In this case, both electrons occupy the bonding orbital with opposite spins, which has a lowest energy. In principle, bonding between atoms occurs if the combined molecular orbital becomes lower in energy than the simple sum of atomic orbitals. For larger molecules, this process becomes increasingly complicated and is generally performed by computers. Among all the molecular orbitals, of specific interest are the highest occupied molecular orbital (HOMO) and the lowest unoccupied molecular orbital (LUMO). The difference between HOMO and LUMO corresponds to the optical energy gap of this molecule. In the presence of many molecules in a solid state, the superposition and interaction of all the molecular orbitals results in a further splitting in energy levels, appearing as band structure.

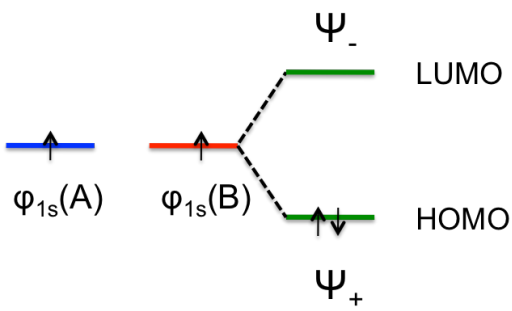

Figure 1.7. Schematic illustration of orbitals' energy levels of a diatomic hydrogen system.

1.3.5. Franck-Condon effect

The classical interpretation of Franck-Condon effect is that the electronic transitions are almost instantaneous, <1 femtosecond, between potential energy curves relative to

nuclear motions, <100 femtoseconds, therefore the electronic transition undergoes a vertical transition in terms of potential energy surface with a fixed nuclear position.

A more accurate description of the Franck-Condon effect requires the aid of quantum mechanics. Consider a molecular system undergoing a transition from an initial state $|i\rangle$ to a final state $|f\rangle$ with a dipole moment operator $\vec{\mu}$. The transition probability under the dipole approximation[68] is expressed as:

$$P_{i->f} = \langle \Psi_f | \vec{\mu} | \Psi_i \rangle \tag{1.21}$$

According to Born-Oppenheimer approximation, the total wavefunction for an N-electron system could be written as a single product of a nuclear wavefunction Ψ_{nuc} that depends only on the nuclear coordinates R_{nuc}, and an electronic wavefunction Ψ_{elec} that depends on the electronic coordinates X_{elec} and parametrically on the nuclear coordinates

$$\Psi_{total} = \Psi_{elec}(X_{elec};R_{nuc}) \times \Psi_{nuc}(R_{nuc}) \tag{1.22}$$

Thus, equation 1.21 becomes

$$P_{i->f} = \langle \Psi^f_{elec} \Psi^f_{nuc} | \vec{\mu} | \Psi^i_{elec} \Psi^i_{nuc} \rangle \tag{1.23}$$

The dipole moment operator can be separated into nuclear component $\vec{\mu}_{nuc}$ and electronic component $\vec{\mu}_{elec}$, turning equation 1.23 into

$$P_{i->f} = \langle \Psi^f_{elec} \Psi^f_{nuc} | \vec{\mu}_{nuc} | \Psi^i_{elec} \Psi^i_{nuc} \rangle + \langle \Psi^f_{elec} \Psi^f_{nuc} | \vec{\mu}_{elec} | \Psi^i_{elec} \Psi^i_{nuc} \rangle \tag{1.24}$$

The first term in the above equation can be rewritten as

$$\left\langle \Psi_{elec}^{f}\Psi_{nuc}^{f}\left|\vec{\mu}_{nuc}\right|\Psi_{elec}^{i}\Psi_{nuc}^{i}\right\rangle = \left\langle \Psi_{nuc}^{f}\left|\vec{\mu}_{nuc}\right|\Psi_{nuc}^{i}\left\langle \Psi_{elec}^{f}\left|\Psi_{elec}^{i}\right\rangle\right\rangle \quad (1.25)$$

The electronic wavefunction integral $\left\langle \Psi_{elec}^{f}\left|\Psi_{elec}^{i}\right\rangle\right.$ cannot be separated from the nuclear wavefunction integral, as it depends parametrically on the nuclear coordinates. However, the electronic wavefunction integral is rigorously 0 because of the electronic wavefunctions are different solutions of the same Schrödinger equation and are orthogonal to each other. The second term in equation 1.24 can be rewritten as

$$P_{i->f} = \left\langle \Psi_{nuc}^{f}\left|\left\langle \Psi_{elec}^{f}\left|\vec{\mu}_{elec}\right|\Psi_{elec}^{i}\right\rangle\right|\Psi_{nuc}^{i}\right\rangle = \left\langle \Psi_{nuc}^{f}\left|D_{ele}\right|\Psi_{nuc}^{i}\right\rangle = \left\langle \Psi_{nuc}^{f}\left|\Psi_{nuc}^{i}\right\rangle\right. \times D_{ele} \quad (1.26)$$

where D_{ele} is the electronic dipole moment and can be treated as constant if it only slowly varies as a function of R_{nuc}. The square of electronic dipole moment, namely $\left|D_{ele}\right|^2$ determines the strength of the transitions. The square of nuclear wavefunction integral, namely $\left|\left\langle \Psi_{nuc}^{f}\left|\Psi_{nuc}^{i}\right\rangle\right.\right|^2$, is the so-called Franck-Condon factor that modulates the relative intensity of the electronic transition with vibrational contributions. A large Franck-Condon factor leads to a larger transition probability, assuming the nuclear positions of initial and final states are similar.

1.4. Thesis layout

This thesis is organized in the following way to investigate organic semiconductors for optoelectronic applications by means of computational methods. In chapter 2, we use various computational methods to design and predict new molecular crystals for desired structures and properties. The most important aspect in this context is the ability to tailor the energy levels of the highest occupied and lowest unoccupied molecular orbitals and to achieve high long-range charge carrier mobility. To this end we pursue functionalization, elemental substitution, and the creation of hybrid molecular building blocks. Following that in chapter 3, a multi-scale model based on density functional theory, molecular dynamics and kinetic Monte Carlo is established and used to investigate the charge transport in our newly designed molecular crystals. In chapter 4, we will address the mechanism for tuning the band gap of OPV materials for better absorption properties. Electronic properties including frontier orbital energy levels, electron energy gap, orbital localization and intramolecular charge transfer are investigated to illustrate the design principle of our molecular systems. In chapter 5, we look into the phenomenon of strong phosphorescence from metal-free organic compounds, which are synthesized and measured by our collaborating lab. We identify a strong correlation between their electronic properties (spin orbital coupling and excited state localization) and emission intensity. Lastly, we will present a summary of this thesis and the outlook in the field of computational organic semiconductors.

1.5. References

1. Gutmann, F. & Lyons, L. E. *Organic semiconductors* (Wiley New York, 1967).
2. Santato, C. & Rosei, F. ORGANIC/METAL INTERFACES Seeing both sides. *Nat. Chem.* **2**, 344-345 (2010).
3. Brabec, C. J. et al. Polymer-Fullerene Bulk-Heterojunction Solar Cells. *Adv. Mater.* **22**, 3839-3856 (2010).
4. Virkar, A. A., Mannsfeld, S., Bao, Z. & Stingelin, N. Organic Semiconductor Growth and Morphology Considerations for Organic Thin-Film Transistors. *Adv. Mater.* **22**, 3857-3875 (2010).
5. Kim, Y. et al. A strong regioregularity effect in self-organizing conjugated polymer films and high-efficiency polythiophene: fullerene solar cells. *Nat. Mater.* **5**, 197-203 (2006).
6. Yersin, H. Triplet emitters for OLED applications. Mechanisms of exciton trapping and control of emission properties. **241**, 1-26 (2004).
7. Risko, C., McGehee, M. D. & Bredas, J.-L. A quantum-chemical perspective into low optical-gap polymers for highly-efficient organic solar cells. *Chem. Sci.* **2**, 1200-1218 (2011).
8. Bolton, O., Lee, K., Kim, H.-J., Lin, K. Y. & Kim, J. Activating efficient phosphorescence from purely organic materials by crystal design. *Nat. Chem.* **3**, 205-210 (2011).
9. Lee, D. et al. Room Temperature Phosphorescence of Metal-Free Organic Materials in Amorphous Polymer Matrices. *J. Am. Chem. Soc.* **135**, 6325-6329 (2013).
10. Kwon, M. S., Lee, D., Seo, S., Jung, J. & Kim, J. Tailoring Intermolecular Interactions for Efficient Room-Temperature Phosphorescence from Purely Organic Materials in Amorphous Polymer Matrices. *Angew. Chem.-Int. Edit.* **53**, 11177-11181 (2014).
11. Scharber, M. C. & Sariciftci, N. S. Efficiency of bulk-heterojunction organic solar cells. *Prog. Polym. Sci.* **38**, 1929-1940 (2013).
12. Dimroth, F. et al. Wafer bonded four-junction GaInP/GaAs//GaInAsP/GaInAs concentrator solar cells with 44.7% efficiency. *Prog. Photovoltaics* **22**, 277-282 (2014).
13. Kim, B.-G. et al. Energy Level Modulation of HOMO, LUMO, and Band-Gap in Conjugated Polymers for Organic Photovoltaic Applications. *Adv. Funct. Mater.* **23**, 439-445 (2013).
14. Coropceanu, V. et al. Charge transport in organic semiconductors. *Chem. Rev.* **107**, 926-952 (2007).
15. Jadhav, P. J., Mohanty, A., Sussman, J., Lee, J. & Baldo, M. A. Singlet Exciton Fission in Nanostructured Organic Solar Cells. *Nano Lett.* **11**, 1495-1498 (2011).
16. Congreve, D. N. et al. External Quantum Efficiency Above 100% in a Singlet-Exciton-Fission-Based Organic Photovoltaic Cell. *Science* **340**, 334-337 (2013).
17. Walker, B. J., Musser, A. J., Beljonne, D. & Friend, R. H. Singlet exciton fission in solution. *Nat. Chem.* **5**, 1019-1024 (2013).
18. Turnbull, G., Samuel, I. & Wang, Y. Theory of Organic Semiconductor Lasers. 9-

32 (2014).
19. Dimitrakopoulos, C. D. & Mascaro, D. J. Organic thin-film transistors: A review of recent advances. *IBM J. Res. Dev.* **45**, 11-27 (2001).
20. Lan, Y.-K. & Huang, C.-I. Charge Mobility and Transport Behavior in the Ordered and Disordered States of the Regioregular Poly(3-hexylthiophene). *J. Phys. Chem. B* **113**, 14555-14564 (2009).
21. Duan, Z.-F. et al. A Novel Thiophene-Fused Polycyclic Aromatic with a Tetracene Core: Synthesis, Characterization, Optical and Electrochemical Properties. *Molecules* **16**, 4467-4481 (2011).
22. Chang, Y.-C. et al. Crystal engineering for pi-pi stacking via interaction between electron-rich and electron-deficient heteroaromatics. *J. Org. Chem.* **73**, 4608-4614 (2008).
23. Sirringhaus, H. et al. Two-dimensional charge transport in self-organized, high-mobility conjugated polymers. *Nature* **401**, 685-688 (1999).
24. Skotheim, T. A. & Reynolds, J. R. Handbook of conducting polymers-conjugated polymers: synthesis, properties and characterization. (2007).
25. Swenberg, C. E. & Pope, M. Electronic processes in organic crystals and polymers. *Oxford University Press, Oxford* (1999).
26. TANG, C. W. & ALBRECHT, A. C. PHOTOVOLTAIC EFFECTS OF METAL-CHLOROPHYLL-A-METAL SANDWICH CELLS. *J. Chem. Phys.* **62**, 2139-2149 (1975).
27. TANG, C. W. 2-LAYER ORGANIC PHOTOVOLTAIC CELL. *Appl. Phys. Lett.* **48**, 183-185 (1986).
28. Mishra, A. & Baeuerle, P. Small Molecule Organic Semiconductors on the Move: Promises for Future Solar Energy Technology. *Angew. Chem.-Int. Edit.* **51**, 2020-2067 (2012).
29. Peumans, P., Bulovic, V. & Forrest, S. R. Efficient photon harvesting at high optical intensities in ultrathin organic double-heterostructure photovoltaic diodes. *Appl. Phys. Lett.* **76**, 2650-2652 (2000).
30. Yakimov, A. & Forrest, S. R. High photovoltage multiple-heterojunction organic solar cells incorporating interfacial metallic nanoclusters. *Appl. Phys. Lett.* **80**, 1667-1669 (2002).
31. YU, G., GAO, J., HUMMELEN, J. C., WUDL, F. & HEEGER, A. J. POLYMER PHOTOVOLTAIC CELLS - ENHANCED EFFICIENCIES VIA A NETWORK OF INTERNAL DONOR-ACCEPTOR HETEROJUNCTIONS. *Science* **270**, 1789-1791 (1995).
32. Oosterhout, S. D. et al. The effect of three-dimensional morphology on the efficiency of hybrid polymer solar cells. *Nat. Mater.* **8**, 818-824 (2009).
33. MOREL, D. L. et al. HIGH-EFFICIENCY ORGANIC SOLAR-CELLS. *Appl. Phys. Lett.* **32**, 495-497 (1978).
34. Potscavage, W. J., Yoo, S. & Kippelen, B. Origin of the open-circuit voltage in multilayer heterojunction organic solar cells. *Appl. Phys. Lett.* **93**, (2008).
35. KIESS, H. & REHWALD, W. ON THE ULTIMATE EFFICIENCY OF SOLAR-CELLS. *Sol. Energy Mater. Sol. Cells* **38**, 45-55 (1995).
36. Potscavage, W. J., Jr, Sharma, A. & Kippelen, B. Critical Interfaces in Organic Solar Cells and Their Influence on the Open-Circuit Voltage. *Accounts Chem.*

Res. **42**, 1758-1767 (2009).
37. Chua, L. L. et al. General observation of n-type field-effect behaviour in organic semiconductors. *Nature* **434**, 194-199 (2005).
38. Chen, C.-H., Hsieh, C.-H., Dubosc, M., Cheng, Y.-J. & Su, C.-S. Synthesis and Characterization of Bridged Bithiophene-Based Conjugated Polymers for Photovoltaic Applications: Acceptor Strength and Ternary Blends. *Macromolecules* **43**, 697-708 (2010).
39. Guenes, S., Neugebauer, H. & Sariciftci, N. S. Conjugated polymer-based organic solar cells. *Chem. Rev.* **107**, 1324-1338 (2007).
40. van Mullekom, H. A. M. *The Chemistry of High and Low Band Gap-conjugated Polymers* (Technische Universiteit Eindhoven, 2000).
41. Bredas, J. L., Heeger, A. J. & Wudl, F. Towards organic polymers with very small intrinsic band gaps. I. Electronic structure of polyisothianaphthene and derivatives. *The Journal of chemical physics* **85**, 4673-4678 (1986).
42. Roncali, J. Synthetic principles for bandgap control in linear π-conjugated systems. *Chemical reviews* **97**, 173-206 (1997).
43. Ajayaghosh, A. Donor-acceptor type low band gap polymers: polysquaraines and related systems. *Chem Soc Rev* **32**, 181-191 (2003).
44. Colladet, K. et al. Low band gap donor-acceptor conjugated polymers toward organic solar cells applications. *Macromolecules* **40**, 65-72 (2007).
45. Segura, J. L. The chemistry of electroluminescent organic materials. *Acta Polym.* **49**, 319-344 (1998).
46. Cheng, Y. C. et al. Three-dimensional band structure and bandlike mobility in oligoacene single crystals: A theoretical investigation. *J. Chem. Phys.* **118**, 3764-3774 (2003).
47. Wang, L. et al. Computational methods for design of organic materials with high charge mobility. *Chem. Soc. Rev.* **39**, 423-434 (2010).
48. Newman, C. R. et al. Introduction to organic thin film transistors and design of n-channel organic semiconductors. *Chemistry of materials* **16**, 4436-4451 (2004).
49. Jurchescu, O. D. *Molecular organic semiconductors for electronic devices* (University Library Groningen][Host], 2006).
50. Mattheus, C. C. et al. Polymorphism in pentacene. *Acta Crystallogr. Sect. C-Cryst. Struct. Commun.* **57**, 939-941 (2001).
51. Anthony, J. E., Eaton, D. L. & Parkin, S. R. A road map to stable, soluble, easily crystallized pentacene derivatives. *Organic letters* **4**, 15-18 (2002).
52. Bardwell, D. A. et al. Towards crystal structure prediction of complex organic compounds - a report on the fifth blind test. *Acta Crystallogr. Sect. B-Struct. Sci.* **67**, 535-551 (2011).
53. Pope, M., Kallmann, H. P. & Magnante, P. Electroluminescence in organic crystals. *The Journal of Chemical Physics* **38**, 2042-2043 (1963).
54. Vincett, P. S., Barlow, W. A., Hann, R. A. & Roberts, G. G. Electrical conduction and low voltage blue electroluminescence in vacuum-deposited organic films. *Thin solid films* **94**, 171-183 (1982).
55. TANG, C. W. & VANSLYKE, S. A. ORGANIC ELECTROLUMINESCENT DIODES. *Appl. Phys. Lett.* **51**, 913-915 (1987).

56. Saleh, B. E. A. & Teich, M. C. Guided-wave optics. *Fundamentals of Photonics (Wiley, 2001)* 238-271 (1991).
57. Forget, S. & Chénais, S. *Organic solid-state lasers* (Springer, 2013).
58. Wu, W. C., Yeh, H. C., Chan, L. H. & Chen, C. T. Red organic light-emitting diodes with a non-doping amorphous red emitter. *Adv. Mater.* **14**, 1072-107+ (2002).
59. Huang, C., Zhen, C. G., Su, S. P., Loh, K. P. & Chen, Z. K. Solution-processable polyphenylphenyl dendron bearing molecules for highly efficient blue light-emitting diodes. *Org. Lett.* **7**, 391-394 (2005).
60. Friend, R. H. et al. Electroluminescence in conjugated polymers. *Nature* **397**, 121-128 (1999).
61. Baldo, M. A. et al. Highly efficient phosphorescent emission from organic electroluminescent devices. *Nature* **395**, 151-154 (1998).
62. Turro, N. J. *Modern molecular photochemistry* (University Science Books, 1991).
63. Climent, C., Alemany, P., Lee, D., Kim, J. & Casanova, D. Optical Properties of 4-Bromobenzaldehyde Derivatives in Chloroform Solution. *J. Phys. Chem. A* **118**, 6914-6921 (2014).
64. HOHENBERG, P. & KOHN, W. INHOMOGENEOUS ELECTRON GAS. *Phys. Rev. B* **136**, B864-B86+ (1964).
65. KOHN, W. & SHAM, L. J. SELF-CONSISTENT EQUATIONS INCLUDING EXCHANGE AND CORRELATION EFFECTS. **140**, 1133-113& (1965).
66. BECKE, A. D. DENSITY-FUNCTIONAL THERMOCHEMISTRY.3. THE ROLE OF EXACT EXCHANGE. *J. Chem. Phys.* **98**, 5648-5652 (1993).
67. RUNGE, E. & GROSS, E. K. U. DENSITY-FUNCTIONAL THEORY FOR TIME-DEPENDENT SYSTEMS. *Phys. Rev. Lett.* **52**, 997-1000 (1984).
68. Herzberg, G. *Molecular Spectra and Molecular Structure. 1966, Volume 3. Electronic Spectra and Electronic Structure of Polyatomic Molecules* (van Nostrand, 1966).

Chapter 2. Electronic properties and crystal structure prediction of octasilsesquioxanes-pentacene hybrid molecular building blocks

2.1. Introduction

The field of organic semiconductor materials has rapidly grown, driven by the huge need of optoelectronic devices that are mechanically flexible and yet inexpensive to fabricate. The performance of such devices crucially depends on the charge carrier (electrons or holes) mobility.[1] Conventionally, organic materials possessed mobilities of the order of 10^{-5} $cm^2V^{-1}s^{-1}$, which is too small for practical applications.[2] Recently, mobilities as high as 10 $cm^2V^{-1}s^{-1}$ at room temperature have been observed in the π-conjugated molecular crystals.[3-5] To further improve the charge carrier transport in organic semiconductors, it is essential to better understand the relationship between molecular structure and carrier mobility. This understanding will help in developing the molecular design criteria for new organic materials with desired properties.

Ultrapure pentacene crystals are well known to have high hole mobilities. However, pentacene molecules adopt a herringbone arrangement in single crystals, in which the neighboring molecules form a V-shaped pattern rather than a parallel configuration. This hinders adequate wavefunction overlap between molecules, and ultimately affects the charge hopping between the molecules. From a molecular engineering point of view, if we can control the orientation of adjacent pentacenes to be parallel to each other, so as to

achieve larger wavefunction overlap, it may be possible to improve charge mobility. In our previous theoretical study on SQ_8 and its functionalized derivatives, we noticed that for individual molecules, functional organic groups attached on SQ_8 cage could only adopt certain orientations due to the cage's rigidity and three-dimensional structure.[6] These investigations also reveal that for crystals of functionalized SQ_8 derivatives, the organic functional groups tend to aggregate to form organic phases while the SQ_8 cages form inorganic phases, as demonstrated using molecular dynamics simulations.[7] These observations led to the hypothesis that by attaching pentacene to the rigid SQ_8 cage to form organic-inorganic hybrid molecules we may potentially be able to control the orientation of pentacene segments. On this premise, former group member Feng Qi explored the structure and properties of a number of concept hybrid molecules, in which he attached between one and eight acene functional groups to the corners of SQ_8 cubes, and among the acenes he included benzene, naphthalene, anthracene, tetracene, and pentacene. He predicted crystal structures for many of these compounds, especially those whose molecular structure possess inversion symmetry, and these findings are documented in his thesis. In the present study, we focus on of these hybrid molecular building blocks, which likely exhibits a significant degree of π-orbital overlap between adjacent acene segments due to their parallel packing, i.e., dipentacene-SQ_8. Moreover, because experimental collaborators advised us of the difficulty in possibly synthesizing this molecule, due to the need for attaching pentacene on the space diagonally opposite corners of the SQ_8 cube, we also explore the structure and properties of a cube with only one pentacene group attached, i.e., monopentacene-SQ_8, and which is entirely the work o the present author. The two concept building blocks are shown in Figure 2.1.

In our approach, we begin from the ground state configurations of either single molecule as the input for Polymorph module embedded in Accelrys' Materials Studio suite of programs, which yields a series of energy-minimized crystal structures for different space groups. The crystal structure with the lowest total energy is considered as the most stable polymorph for the corresponding molecule. We then apply Molecular dynamics (MD) and density functional theory (DFT) to further relax these crystal structures towards their ground state configurations and verify their stability.

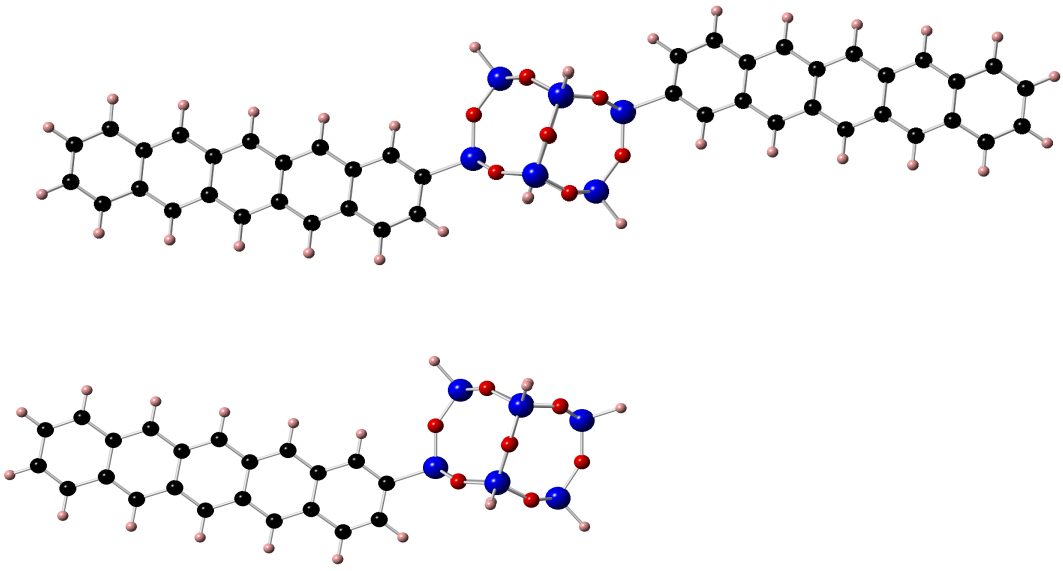

Figure 2.1. Optimized molecular structures of dipentacene-SQ_8 (upper) and monopentacene-SQ_8 (lower) at the approximation level of B3LYP/6-31G*. The rigidity and three-dimensional structure of SQ8 cage force pentacene segments to only adopt certain directions. C (black), H (pink), O (red), Si (blue).

2.2. Methodology and Computational Details

2.2.1. Ground state analysis

First principles calculations on the electronic properties of single molecule are performed using Gaussian09.[8] We choose B3LYP as the exchange-correlation functional, which is a Hartree-Fock-DFT hybrid where the exchange energy is explicitly calculated using a Hartree-Fock approach.[9] The molecular geometries are optimized in Cartesian coordinates without symmetry constraints using 6-31G* contracted Gaussian basis set with polarization functions.

2.2.2. Polymorph prediction method

The identification of the most probable crystal structures for the various candidate building blocks is accomplished using molecular modeling software from Accelrys' Materials Studio suite of programs. It has been identified as one of the most effective packages in the crystal structure prediction blind test.[10] The structure optimization simulations are based on the COMPASS force field,[11] which provides the expediency required for sampling large numbers of trial structures. The Polymorph prediction program uses MD and Monte Carlo simulated annealing methods to predict multiple space groups for a given single molecule conformation. It first generates a large number of low-density crystal packing structures during the packing stage. During the clustering step, it filters out duplicate packing structures to reduce the total number of structures based on Monte Carlo and MD relaxation energy. Then a geometry optimization of the remaining structures is performed using the smart energy minimization method. In a second clustering step duplicate structures, if there are any, are removed and potential

crystal packing structures are sorted according to total system energy. In the end, the crystal structure with the lowest energy is considered the most stable crystal structure for this molecule. A Parrinello-Rahman algorithm[12,13] is used to control the size and shape of the simulation box at finite temperatures. To reduce the computational cost, we only study the structures in the 9 most common space groups found in the Cambridge Structural Database (CSD),[14] including $P\bar{1}$, P21/c, C2, C2/c, P21, PBCA, CC, PNA21 and PBCN.

Once possible stable crystalline structures are identified, first principles calculations are carried out to further relax these structures using VASP.[15] The exchange-correlation energy is evaluated according to the generalized gradient approximation PBE(GGA-PBE).[16] The interaction between atomic cores and valence electrons is described by the projector augmented wave (PAW) method.[17] To account for the dispersion interactions, which constitute the prevalent cohesive forces in organic crystals, we also include the non-local correlation functional vdW-DF that is pre-installed in VASP.[18] Structures are optimized until the force on each atom was as small as 0.001 eV/Å.

In order to further confirm the validity of our predicted crystal structures, we perform MD simulations using LAMMPS[19] and examine their stability at room temperature. For this purpose we use again the well-established COMPASS force field.[4,11] We prepare a simulation box by replicating a unit cell in three crystallographic directions, generating an ordered packing structure consisting of 16 unit cells (i.e., 32 molecules). The system is first relaxed for 2 ns in the NPT ensemble with a time step of 2 fs and the target temperature set to 300K. For each system we make sure that the variation in system temperature remained smaller than 1%. The lattice parameters and bond lengths are

recorded every 2000 steps, for a total of 500 snapshots. On this basis, we ensure the validity of COMPASS force field for our systems, as well as verify the stability of the relaxed structures at room temperature.

2.3. Results and Discussion

2.3.1. Structure and electronic properties of single molecules

In optimized dipentacene-SQ_8, the two pentacene segments attached to the SQ_8 cage along the diagonal lie in the same plane and their longitudinal axes are parallel to each other, and they are at a maximum separation from each other (Figure 2.1). The monopentacene-SQ_8 has a very similar structure, except for holding only one planar pentacene segment. The SQ_8 cage is very rigid even after functionalization with the organic groups. Bond distances and angles deviate from those of hydrogen terminated SQ_8 cages by typically less than 2%.[6] The deformation of the cage upon functionalization with acenes can be measured by the change of the distance between two silicon atoms along the body diagonal before and after attaching the pentacene segments. In SQ_8, this distance is 5.473 Å. In dipentacene-SQ_8 and monopentacene-SQ_8, the distance is 5.517 Å and 5.496 Å, i.e., only 0.8% and 0.4% larger than the distance in SQ_8, respectively.

Comparing the electron density isosurfaces of dipentacene-SQ_8 and pentacene (Figure 2.2), we can see that the frontier orbitals of the hybrid molecule are mainly localized on pentacene. On close inspection, however, we notice that the frontier orbitals extend inside the SQ_8 cage, occupying the space around the anchoring silicon atoms in case of the highest occupied molecular orbitals (HOMO) and engulfing the majority of the SQ_8 cage bonding structure in case of the lowest unoccupied molecular orbitals (LUMO). Hence,

we can expect the electronic properties of the hybrid molecules to be dominated by the pentacene segments but influenced by the SQ_8 core. Indeed, the HOMO and LUMO energy levels for the hybrid molecules are close to those of pure pentacene, i.e., the HOMO levels are –4.72 eV for dipentacene-SQ_8, –4.75 eV for monopentacene-SQ_8 and –4.60 eV for pure pentacene, whereas the LUMO levels are –2.52 eV for dipentacene-SQ_8, –2.55 eV for monopentacene-SQ_8 and –2.38 eV for pure pentacene. The HOMO-LUMO gap (2.20 eV) of the hybrid molecule is much smaller than that for hydrogen terminated SQ_8 (8.85 eV) and very close to that of pure pentacene (2.22 eV).

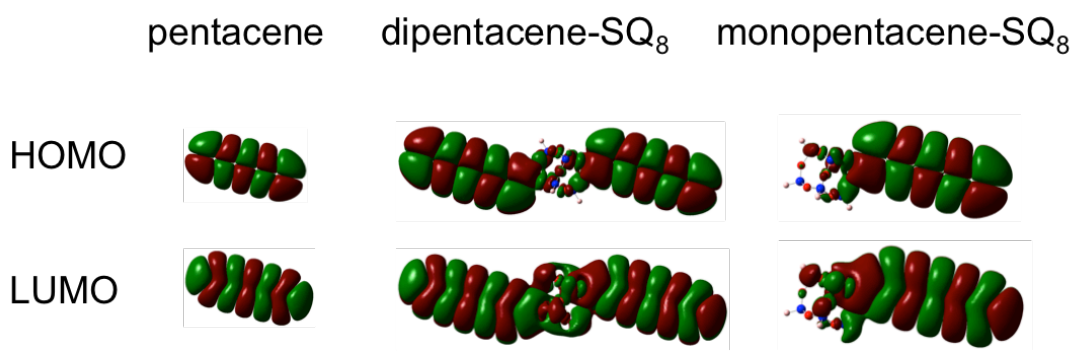

Figure 2.2. Electron density (0.0005 au) of pentacene, dipentacene-SQ_8 and monopentacene-SQ_8 . The frontier orbitals mainly localize on pentacene segments and partially on SQ_8 cage.

2.3.2. Crystal structure prediction of hybrid molecules

Figure 2.3 and Figure 2.4 show the most probable crystal structures of dipentacene-SQ_8 and monopentacene-SQ_8. The lowest ground state energy is found for a crystal structure with $P\bar{1}$ symmetry (Figure 2.3), while P21/c was a close second in terms of these attributes. Both have two molecules per unit cell, as does pure crystalline pentacene.[20] The structures belonging to other symmetry groups have higher energy, indicating that

they may not be as stable as those with $P\bar{1}$ or P21/c symmetry. The crystal structure information of the predicted polymorphs is listed in Table 2.1.

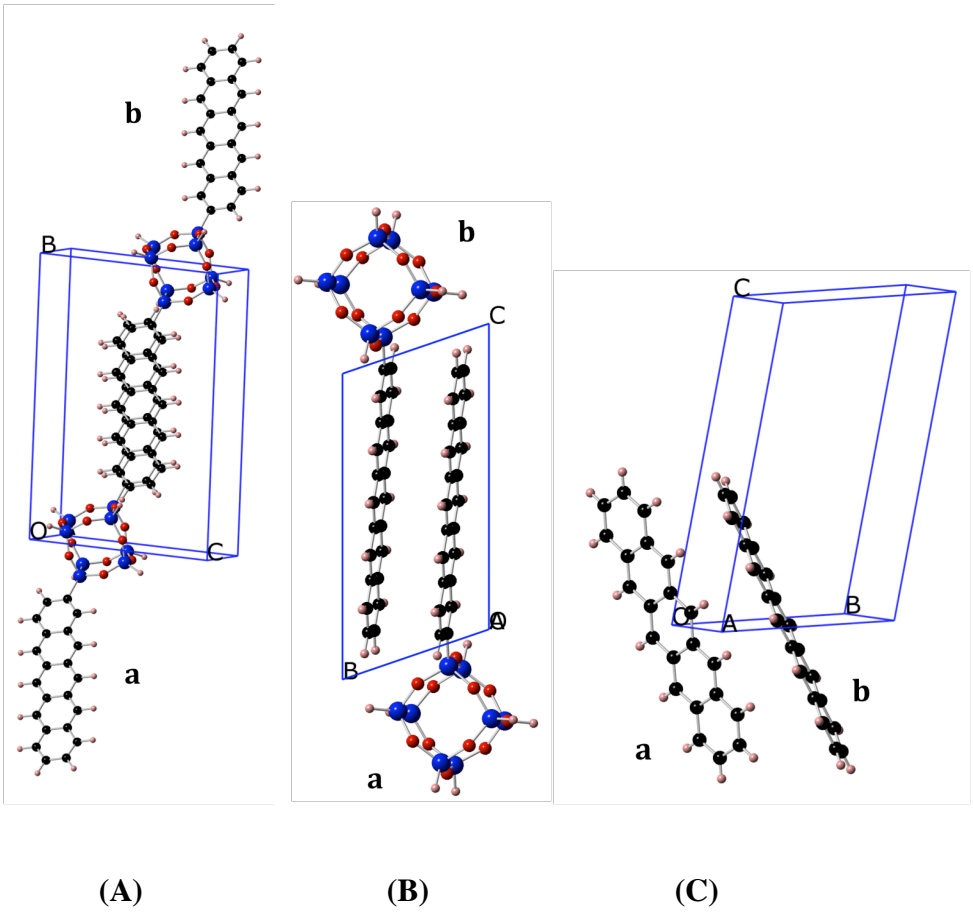

Figure 2.3. (A&B) The most probable crystal structures of dipentacene-SQ_8 and monopentacene-SQ_8. (C) Crystal structure of pentacene. There are two molecules in one unit cell of each crystal. Unlike the two molecules formed a V-shape in pentacene, the pentacene segments in the two molecules in dipentacene-SQ_8 and monopentacene-SQ_8 crystal structure form parallel configuration, which may have larger wavefunction overlap.

Due to procedural inaccuracies in the calculations, discrepancies between predicted and experimental structures may be expected. However, the structures predicted to have the lowest energies are mostly characterized by paralleled packing of the pentacene

segments, in contrast to the herringbone stacking in pentacene crystal. This provides for an enhanced π - π orbital overlap, which is highly desired for good intermolecular charge transfer. As a consequence, in the two new hybrid materials, one may expect comparable or even higher charge mobility than in pentacene.

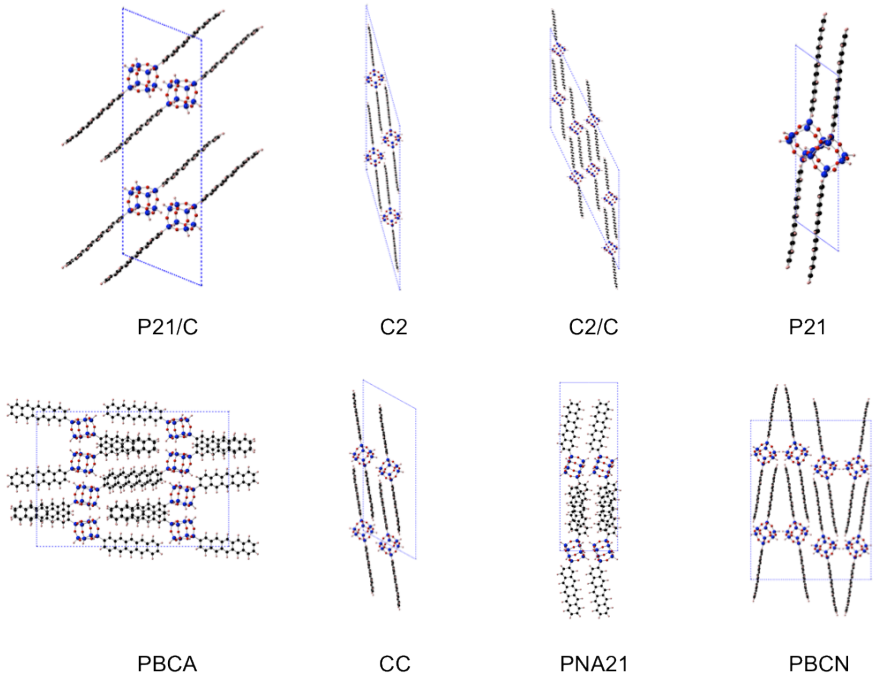

(A)

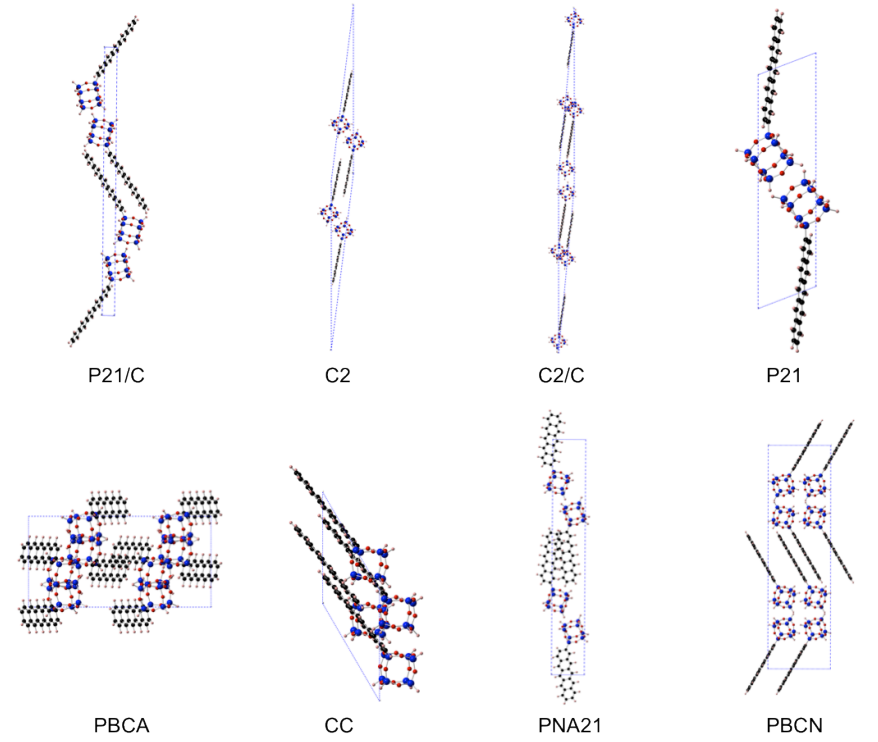

(B)

Figure 2.4. Other possible crystal structures of (A) dipentacene-SQ_8 and (B) monopentacene-SQ_8. Note that in most of the structures, the pentacene segments adopt parallel configuration.

To further validate our crystal structures, we carried out the MD simulations and DFT calculations. In MD simulations, the correctness of COMPASS force field is also tested simultaneously. Table 2.2 shows the averaged lattice parameters generated in MD simulations at 300K compared with that optimized by DFT calculations. For all three crystals, MD simulations yield results similar to those of DFT calculations, indicating a good stability of crystals at ambient conditions and thus predicting a high likelihood for successful synthesis of these hybrid compounds in the laboratory. For pentacene, both DFT calculations MD simulations agree with the experimental findings.[20] Furthermore, we recorded the bond lengths of a single molecule in the crystal at different time intervals

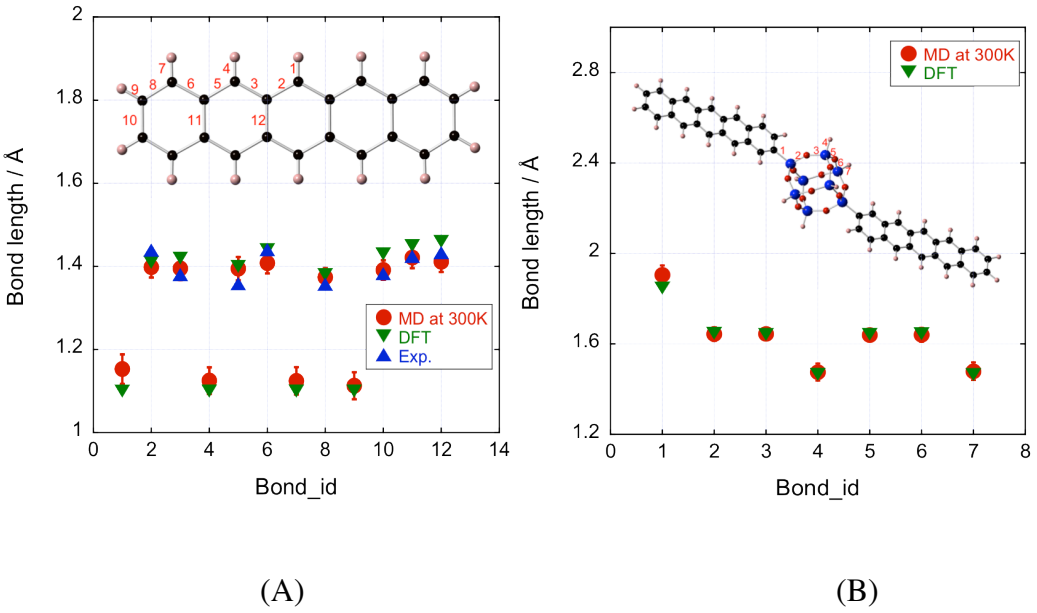

Figure 2.5. Atomic bond lengths of (A) pentacene (A) and (B) dipentacene-SQ_8 molecule (black: carbon; pink: hydrogen; blue: silicon; red: oxygen). The bond lengths in MD simulation are averaged over 500 steps. The DFT simulated values are also shown in the graph. The missing bond lengths follow symmetry.

of the MD simulations. Without losing generality, the average bond lengths and their standard deviations (in form of the error bar) for only C-C, C-H in pentacene and Si-C,

Si-O, Si-H in dipentacene-SQ_8 are shown in Figure 2.5 and compared with results from DFT calculations and experimental values. We observe high consistency between the bond lengths in DFT calculations and MD simulations. The fluctuations of bond lengths in MD simulations are in a reasonable range, with a maximum standard deviation of 0.03Å. Particularly, the bond lengths for pentacene are in good agreement with the experimental measurements reported in the literature.[21] As a result, our predicted crystal structures as well as the pentacene crystal structure are confirmed to be stable by both computational methods.

2.4. Conclusions

We designed hybrid molecules by functionalizing the SQ_8 cage with one and two pentacene molecules. The possible crystal structures of the hybrid materials are investigated by a combination of Monte Carlo method, molecular dynamics and density functional theory. The design principle is to use the rigidity and three-dimensional structure of SQ_8 cage to control the orientation of pentacene segments such that parallel configurations for better orbital overlap are adopted. The most probable structures for the two hybrid molecules both show a parallel configuration of pentacene segments in the crystals. This parallel configuration enhances the electron orbital overlap between pentacene segments, which makes the two hybrid-molecular crystals potentially better transport materials than pentacene crystal.

Table 2.1. Properties of predicted most possible crystal structures of dipentacene-SQ_8 and monopentacene-SQ_8 by Polymorph.

	dipentacene-SQ_8			monopentacene-SQ_8		
Space group	$P\bar{1}$	P21/C	PBCA	$P\bar{1}$	P21/C	PBCA
a (Å)	7.0671	20.1273	7.1066	14.5799	16.0154	27.9551
b (Å)	20.2152	29.4681	78.9321	17.9693	51.5121	13.9315
c (Å)	16.2284	7.1877	14.8107	14.628	23.0578	14.5148
α (deg)	107.744	90	90	84.559	90	90
β (deg)	119.169	69.7388	90	76.07	171.4768	90
γ (deg)	66.351	90	90	23.669	90	90

Table 2.2. Lattice parameters for pentacene, dipentacene-SQ_8 and monopentacene-SQ_8 crystals relaxed by different simulation methods (MD and DFT).

	pentacene			dipentacene-SQ_8		monopentacene-SQ_8	
	Exp.	DFT	MD	DFT	MD	DFT	MD
a (Å)	6.266	6.392	6.478(±0.02)	7.210	7.348(±0.03)	13.671	13.704((±0.01)
b (Å)	7.775	7.872	7.848(±0.03)	20.372	20.755(±0.01)	16.879	16.635(±0.02)
c (Å)	14.530	14.660	14.995(±0.05)	16.665	16.971(±0.02)	14.524	14.534(±0.02)
α (deg)	76.475	76.263	76.903(±0.05)	107.550	107.398(±0.02)	88.607	88.498(±0.01)
β (deg)	87.682	87.336	87.754(±0.01)	118.397	118.366(±0.02)	79.966	80.012(±0.03)
γ (deg)	84.684	84.801	84.734(±0.02)	67.171	67.205(±0.01)	24.233	24.313(±0.02)

2.5. References

1. Coropceanu, V. et al. Charge transport in organic semiconductors. *Chem. Rev.* **107**, 926-952 (2007).
2. Wang, L. et al. Computational methods for design of organic materials with high charge mobility. *Chem. Soc. Rev.* **39**, 423-434 (2010).
3. Sundar, V. C. et al. Elastomeric transistor stamps: Reversible probing of charge transport in organic crystals. *Science* **303**, 1644-1646 (2004).
4. Ionescu, T. C. et al. Evaluation of force fields for molecular simulation of polyhedral oligomeric silsesquioxanes. *J. Phys. Chem. B* **110**, 2502-2510 (2006).
5. Shirota, Y. & Kageyama, H. Charge carrier transporting molecular materials and their applications in devices. *Chem. Rev.* **107**, 953-1010 (2007).
6. Zhen, C.-G., Becker, U. & Kieffer, J. Tuning Electronic Properties of Functionalized Polyhedral Oligomeric Silsesquioxanes: A DFT and TDDFT Study. *J. Phys. Chem. A* **113**, 9707-9714 (2009).
7. Zhou, J. & Kieffer, J. Molecular dynamics simulations of monofunctionalized polyhedral oligomeric silsesquioxane C6H13(H7Si8O12). *J. Phys. Chem. C* **112**, 3473-3481 (2008).
8. Frisch, M. J. et al. Gaussian 09. (2009).
9. BECKE, A. D. DENSITY-FUNCTIONAL THERMOCHEMISTRY.3. THE ROLE OF EXACT EXCHANGE. *J. Chem. Phys.* **98**, 5648-5652 (1993).
10. Bardwell, D. A. et al. Towards crystal structure prediction of complex organic compounds - a report on the fifth blind test. *Acta Crystallogr. Sect. B-Struct. Sci.* **67**, 535-551 (2011).
11. Sun, H. COMPASS: An ab initio force-field optimized for condensed-phase applications - Overview with details on alkane and benzene compounds. *J. Phys. Chem. B* **102**, 7338-7364 (1998).
12. PARRINELLO, M. & RAHMAN, A. CRYSTAL-STRUCTURE AND PAIR POTENTIALS - A MOLECULAR-DYNAMICS STUDY. *Phys. Rev. Lett.* **45**, 1196-1199 (1980).
13. PARRINELLO, M. & RAHMAN, A. POLYMORPHIC TRANSITIONS IN SINGLE-CRYSTALS - A NEW MOLECULAR-DYNAMICS METHOD. *J. Appl. Phys.* **52**, 7182-7190 (1981).
14. Cabeza, A. J. C., Pidcock, E., Day, G. M., Motherwell, W. D. S. & Jones, W. Space group selection for crystal structure prediction of solvates. *Crystengcomm* **9**, 556-560 (2007).
15. Kresse, G. & Furthmuller, J. Efficient iterative schemes for ab initio total-energy calculations using a plane-wave basis set. *Phys. Rev. B* **54**, 11169-11186 (1996).
16. Perdew, J. P., Burke, K. & Ernzerhof, M. Generalized gradient approximation made simple. *Phys. Rev. Lett.* **77**, 3865-3868 (1996).
17. BLOCHL, P. E. PROJECTOR AUGMENTED-WAVE METHOD. *Phys. Rev. B* **50**, 17953-17979 (1994).
18. Dion, M., Rydberg, H., Schroder, E., Langreth, D. C. & Lundqvist, B. I. Van der waals density functional for general geometries (vol 92, art no 246401, 2004). *Phys. Rev. Lett.* **95**, (2005).

19. PLIMPTON, S. FAST PARALLEL ALGORITHMS FOR SHORT-RANGE MOLECULAR-DYNAMICS. *J. Comput. Phys.* **117**, 1-19 (1995).
20. Mattheus, C. C. et al. Polymorphism in pentacene. *Acta Crystallogr. Sect. C-Cryst. Struct. Commun.* **57**, 939-941 (2001).
21. Endres, R. G., Fong, C. Y., Yang, L. H., Witte, G. & Woll, C. Structural and electronic properties of pentacene molecule and molecular pentacene solid. *Comput. Mater. Sci.* **29**, 362-370 (2004).

Chapter 3. Computational modeling of octasilsesquioxanes-pentacene nanocomposites with very high charge mobility

3.1. Introduction

Even though the intrinsic mechanisms of charge transport in organic materials has been studied for decades, the theoretical understanding is difficult to extract from experimental data alone, due to the complexity of organic systems.[1] The main focus of recent theoretical studies has been to develop better models for explaining the band-like behavior found in experiments, i.e. the fact that the carrier mobility decreases with temperature.[2-4] This behavior is widely described as the consequence of increased phonon scattering with temperature by delocalized charge carriers. However, a recent study on the transport properties of polyacenes based on a tight-binding band model with electron-phonon scattering under a constant time approximation demonstrated that the mean free path of charge carriers at high temperatures is comparable or even shorter than the lattice constant, indicating strong charge localization within organic semiconductors.[5] The band model fails due to the weak interaction between organic molecules, which are held together by van der Waals forces. Instead, the charge transport mechanism is more accurately described by a hopping process, in which holes and electrons hop between discontinuous localized electronic states. Indeed, the semi-classical Marcus hopping model[6] has been used by many groups and successfully explains some experimental data at room temperature.[7-9] However, Marcus' theory is based on the principle of thermal

activation, according to which high temperature provides more energy to overcome the transport barrier, which is contrary to band-like behavior. One of the refined Marcus-based models successfully reproduces the band-like behavior in various organic single crystals.[9-11] Unlike other proposed models, such as the polaron model,[5] this model retains the basic idea of a charge carrier hopping process in organic materials, but also takes into account the nuclear tunneling effect in which intramolecular modes contribute to the charge transfer process through local electron-phonon coupling.[12] Since this effect gets stronger at low temperatures,[13] the carrier mobility behaves in a band-like manner as based on its temperature dependence.

Another important aspect, which as of yet is poorly accounted for in theoretical models, is the effect of thermal disorder on charge transport. Thermal disorder is essential to assumptions made for hopping models, as it destroys the translational symmetry of the electronic Hamiltonian and leads to a localized charge description.[14] The way thermal disorder affects the charge transfer integral has been studied for materials with apparent wavefunction continuity into one and two dimensions. Troisi proposed that thermal disorder is the main cause of the band-like behavior of charge transport in the 1-D stack of organic molecules they studied.[15] However, Wang concluded that 2-D charge transport is unaffected by dynamic disorder, and the nuclear tunneling effect of intramolecular vibrations is the only source that gives rise to the band-like behavior.[11] How the real 3-D materials respond to the dynamic disorder effect has yet to be established.

In this work, we develop a quantum charge transfer hopping model to assess the charge carrier mobility in the three organic single crystals (Figure 2.3), which provide 1-D, 2-D and 3-D charge conduits, respectively. First, we perform density functional theory (DFT)

calculations to obtain two key related parameters, i.e. Huang-Rhys factors and charge transfer integrals. The charge transfer integral characterizes the extent of wavefunction overlap and the strength of electronic coupling between the two molecules in a hopping pair (dimer). Since charge transfer integral is strongly influenced by the relative position of the two molecules, we apply molecular dynamics (MD) simulations to obtain hundreds of snapshots of dimer geometries and use those as the input for DFT calculations to generate a distribution of charge transfer integral values. The intramolecular normal modes are crucial to predict the charge transfer rate because they allow one to account for the way electron-phonon coupling affects the charge transfer, which is commonly known as nuclear tunneling effect. Huang-Rhys factors are the physical parameters to measure the extent of electron-phonon coupling for each intramolecular normal mode. Accordingly, we can calculate the charge transfer rate for a single hopping step. Finally, implement the kinetic Monte-Carlo method to simulate long-range charge transport that is composed of millions of hopping step. The detail of the entire calculation is shown in the next section.

3.2. Methodology and Computational Details

The basic premise for the hopping model is that electrons hop from anions to neutral molecules through the LUMO while holes hop from cations to neutral molecules through the HOMO, a process that is expressed by the following reaction equation

$$M_1^{\pm} + M_2 \rightarrow M_1 + M_2^{\pm} \tag{3.1}$$

With this hopping "reaction" we can associate a rate coefficient $k_{i->f}$ that depends on a number of quantities, including the charge transfer integral, the extent of electron-phonon

coupling, the difference between the free energies of the initial and final state, etc., as detailed in the following.

3.2.1. Charge transfer rate based on perturbation theory

The quantum charge transfer rate was derived by Jortner[16] and Lin *et al*.[17] Nan *et al*. successfully used this rate theory to investigate the charge transport properties of several organic crystals and observed consistent results with experiments.[10] The derivation starts from the Fermi golden rule,

$$k_{i->f} = \frac{2\pi}{\hbar} V^2 \sum_{\upsilon} \sum_{\upsilon'} P_{i\upsilon} \left| \left\langle \Psi_{f\upsilon'} \middle| \Psi_{i\upsilon} \right\rangle \right|^2 \delta(E_{f\upsilon'} - E_{i\upsilon}) \tag{3.2}$$

where V is the charge transfer integral between initial and final state, $\left| \left\langle \Psi_{f\upsilon'} \middle| \Psi_{i\upsilon} \right\rangle \right|^2$ is the Franck-Condon factor. To simplify, the motion of the atoms in the initial and final states can be described as harmonic oscillators, reflecting the curvature of the potential energy surfaces of two states,

$$\Psi_{i\upsilon} = \prod_j \chi_{i\upsilon_j}(Q_j) \tag{3.3}$$

$$\Psi_{f\upsilon'} = \prod_j \chi_{f\upsilon'_j}(Q'_j) \tag{3.4}$$

where Q_j denotes nuclear configuration, and the wavefunction of a harmonic oscillator is expressed as

$$\chi_{i\upsilon_j}(Q_j) = \sqrt{\frac{\beta_j}{\sqrt{\pi} 2^{\upsilon_j} \upsilon_j!}} H_{\upsilon_j}(\beta_j Q_j) \exp(-\frac{\beta_j^2 Q_j^2}{2}) \tag{3.5}$$

Note that $\beta_j = \sqrt{\frac{\omega_j}{\hbar}}$ and H_{v_j} are the Hermite polynomials. P_{iv} is the distribution function for the initial state and is expressed as

$$P_{iv} = \left[\sum_v \exp(\frac{-E_{iv}}{k_B T})\right]^{-1} \exp(\frac{-E_{iv}}{k_B T}) = \prod_j 2\sinh\frac{\hbar\omega_j}{2k_B T}\exp(\frac{-\hbar\omega_j(v_j+\frac{1}{2})}{k_B T}) \tag{3.6}$$

By redefining $P_{iv} = \prod_j P_{iv_j}$ and using the relation $\delta(E_{fv'} - E_{iv}) = \frac{1}{2\pi\hbar}\int_{-\infty}^{\infty} dt e^{it\omega_{fv',iv}}$ for the delta function, equation 3.2 can be rewritten as

$$k_{i->f} = \frac{V^2}{\hbar^2}\int_{-\infty}^{\infty} dt e^{it\omega_{fi}}\prod_j G_j(t) \tag{3.7}$$

where

$$G_j(t) = \sum_{\upsilon_j}\sum_{\upsilon'_j} P_{i\upsilon_j}\left|\left\langle \chi_{f\upsilon'_j}\middle|\chi_{i\upsilon_j}\right\rangle\right|^2 \exp\left\{it\left[\left(\upsilon'_j+\frac{1}{2}\right)\omega'_j - \left(\upsilon_j+\frac{1}{2}\right)\omega_j\right]\right\} \tag{3.8}$$

In order to simplify G_j, Mehler's formula is utilized,

$$\begin{aligned}&\sum_{n=0}^{\infty}\frac{\exp(-(n+\frac{1}{2})t)}{\sqrt{\pi}2^n n!}H_n(x)H_n(x')\exp\left[-\frac{1}{2}(x^2+x'^2)\right]\\ &= (2\pi\sinh t)^{-\frac{1}{2}}\exp\left[-\frac{1}{4}(x+x')^2\tanh\frac{1}{2}t - \frac{1}{4}(x-x')^2\coth\frac{1}{2}t\right]\end{aligned} \tag{3.9}$$

where $H_n(x)$ are the Hermite polynomials. Substituting the wavefunction of harmonic oscillator (equation 3.5) into equation 3.8, we obtain

$$G_j(t) = \frac{2\beta_j \beta'_j \sinh(\frac{\hbar\omega_j}{2kT})}{2\pi\sqrt{\sinh\kappa_j \sinh\mu'_j}}$$
$$\times \int dQ'_j\, dQ'_j\, dQ_j dQ_j \exp\left\{-\frac{1}{4}\beta'^2_j \left[(Q'_j + Q'_j)^2 \tanh\frac{1}{2}\mu'_j + (Q'_j - Q'_j)^2 \coth\frac{1}{2}\mu'_j\right]\right\}$$
$$\times \exp\left\{-\frac{1}{4}\beta_j^2 \left[(Q_j + Q_j)^2 \tanh\frac{1}{2}\kappa_j + (Q_j - Q_j)^2 \coth\frac{1}{2}\kappa_j\right]\right\} \tag{3.10}$$

where $u'_j = -i\omega'_j t$ and $\kappa_j = i\omega_j t + \hbar\omega_j / k_B T$. We consider the displaced harmonic oscillator approximation, that is, $\omega_j = \omega'_j$ and $\Delta Q_j = Q'_j - Q_j$. Equation 3.10 now becomes

$$G_j(t) = \exp\left\{-S_j\left[\coth\frac{\hbar\omega_j}{2k_B T} - \operatorname{csc} h\frac{\hbar\omega_j}{2k_B T}\cosh(it\omega_j + \frac{\hbar\omega_j}{2k_B T})\right]\right\} \tag{3.11}$$

or

$$G_j(t) = \exp\left\{-S_j\left[(2n_j + 1) - n_j e^{-it\omega_j} - (n_j + 1)e^{it\omega_j}\right]\right\} \tag{3.12}$$

Substituting equation 3.12 into equation 3.7 yields

$$k_{i->f} = \frac{V^2}{\hbar^2}\int_{-\infty}^{\infty} dt \exp\left\{i\omega_{fi}t - \sum_j S_j[(2n_j + 1) - n_j e^{-i\omega_j t} - (n_j + 1)e^{i\omega_j t}]\right\} \tag{3.13}$$

Equation 3.13 is the main equation for calculating charge transfer rate in this study. Here, V is the charge transfer integral. ω_j is the j^{th} normal mode frequency, S_j is the Huang-Rhys factor related to j^{th} normal mode , and $n_j = [\exp(\hbar\omega_j / k_B T) - 1]^{-1}$ is defined as the occupation number. The local electron-phonon coupling is often characterized by S_j,

which can be obtained through normal mode analysis. In this study, the normal modes of vibration are first calculated on the optimized structures of neutral and charged molecules. Then the changes of geometry between optimized neutral and charged molecules are projected onto all the normal mode directions. Finally, the Huang-Rhys factors related to the j^{th} mode ω_j is calculated as $S_j = (2\hbar)^{-1}\omega_j(\Delta Q_j)^2$, where ΔQ_j represents the rigid displacement projected onto the j^{th} normal mode (Figure 3.1(a)). In this study, we use the DUSHIN code developed by Reimers[18] to obtain the Huang-Rhys factors. $\omega_{fi} = \Delta G/\hbar$ and ΔG is the free energy change when an electron (hole) hops from molecule *i* to *j* and is defined as

$$\Delta G = E_j(M_j^{\mp 1}, M_{l\neq j}^0) - E_i(M_i^{\mp 1}, M_{l\neq i}^0) \pm e\vec{r}_{ij}\cdot\vec{F} \qquad (3.14)$$

where the energy $E_j(M_j^{\mp 1}, M_{l\neq j}^0)$ is the electrostatic energy of the system in which molecule *j* is anion (cation) and the others are neutral, *e* is unit charge, $\vec{r}_{ij}$ is the vector between the centers of the hopping sites, and $\vec{F}$ is an externally applied electric field. In this study, the non-electric-field term vanishes if the two molecules in the hopping pair are of the same type.

Depending on the conditions, equation 3.13 assumes different forms. In presence of strong coupling, i.e. $\sum_j S_j >> 1$, we can use the short time approximation by expanding $\exp(it\omega_j) = 1 + it\omega_j + (it\omega_j)^2/2 + ...$ Keeping only the first three terms, we can further simplify equation 3.13 into

$$k_{i->f} = \frac{V^2}{\hbar^2}\sqrt{\frac{2\pi}{\sum_j S_j \omega_j{}^2(2n_j+1)}}\exp(-\frac{(\omega_{fi}+\sum_j S_j\omega_j)^2}{2\sum_j S_j\omega_j{}^2(2n_j+1)}) \tag{3.15}$$

In the classic high-temperature limit, we have $\hbar\omega_j / k_B T << 1$, thus $n_j >> 1$. We can further reduce equation 3.15 to

$$k_{i->f} = \frac{V^2}{\hbar^2}\sqrt{\frac{\pi\hbar}{k_B T\sum_j S_j\omega_j}}\exp(-\frac{\hbar(\omega_{fi}+\sum_j S_j\omega_j)^2}{4k_B T\sum_j S_j\omega_j}) \tag{3.16}$$

or

$$k_{i->f} = \frac{V^2}{\hbar}\sqrt{\frac{\pi}{\lambda k_B T}}\exp(-\frac{(\Delta G+\lambda)^2}{4\lambda k_B T}) \tag{3.17}$$

This is the classical Marcus equation,[6] and it has been widely used to study the transport properties in organic semiconductors at high temperature.[19] $\lambda = \sum_j S_j\hbar\omega_j$ is the inner (intramolecular) reorganization energy, which represents the activation barrier originating from the configuration adjustment of molecules during the charge transfer. Figure 3.1 (b) shows the method of estimating λ from potential energy surfaces.

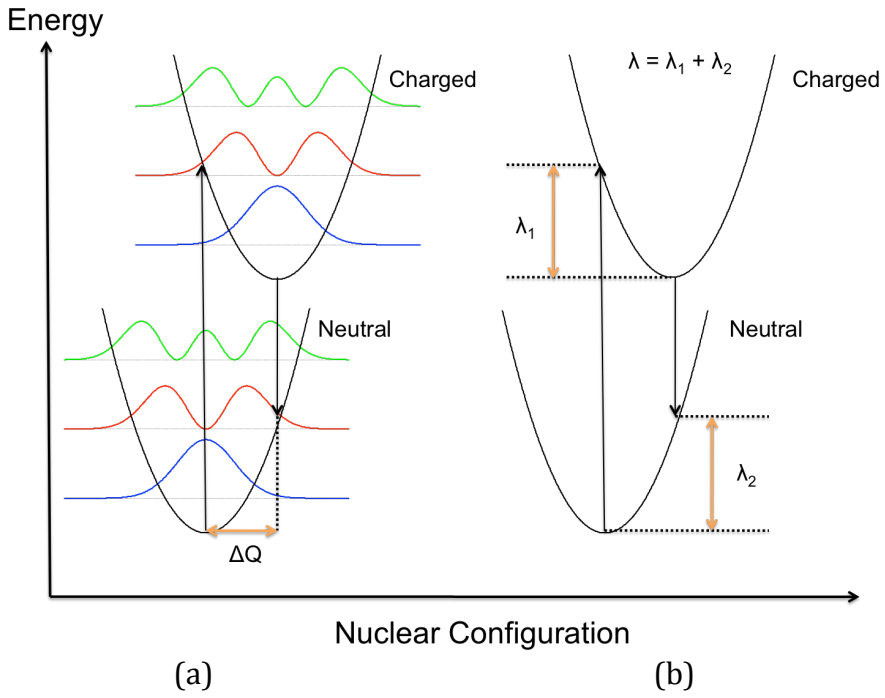

Figure 3.1. Schematic illustration of the potential energy surface of the neutral and charged molecules. (a) According to Franck-Condon effect, vibrational levels in a harmonic oscillator approximation are favored when they correspond to a minimal change in the nuclear coordinates. ΔQ is the normal mode displacement (b) reorganization energy λ is obtained by comparing the energies in the uncharged and charged optimized configurations, for both neutral and ionized states.

3.2.2. Charge transfer integral

For charge transfer integral for a molecular pair is written as

$$V = \left\langle M_1^{\pm} M_2 \middle| H \middle| M_1 M_2^{\pm} \right\rangle \tag{3.18}$$

where H is the interaction Hamiltonian. In the literature, there are several computational methods that allow one to obtain the transfer integral for a fixed geometry. For example, the energy level splitting method based on Koopmans' theorem postulates that the transfer integral is equal to the energy difference between the HOMO and HOMO–1 (i.e.,

one level lower than HOMO).[20] A more accurate way is to directly evaluate the electronic coupling element for frontier orbitals, as discussed by Nan *et al*.[10] The transfer integral can be rewritten as

$$V = \left\langle \Psi_{HOMO}^{0,M_1} \middle| F \middle| \Psi_{HOMO}^{0,M_2} \right\rangle \tag{3.19}$$

where $\left|\Psi_{HOMO}^{0,M_1}\right\rangle$ and $\left|\Psi_{HOMO}^{0,M_2}\right\rangle$ represents the HOMOs of the two isolated molecules M_1 and M_2, when no intermolecular interactions exist. F is the Fock operator that can be expressed as

$$F = SC\varepsilon C^{-1} \tag{3.20}$$

where S is the intermolecular overlap matrix, and C and ε are the Kohn-Sham orbital's coefficients and energies for the pair. A standard self-consistent (SCF) field procedure is used to calculate the non-interacting molecular orbitals of the two individual molecules. These orbitals are further used to construct the Kohn-Fock matrix, where one can eventually obtain the interaction information with respect to the individual molecules based on the first order perturbation.

In a real molecular system (e.g. molecular single crystal), however, it would be too much of a simplification to keep molecular geometries fixed because of intermolecular vibrations. Due to the variation of molecular geometries with time, the charge transfer integral essentially varies as the system progresses through a series of configurational snapshots. This represents the essence of thermal disorder, which evidently casts some uncertainty as to the magnitude of the charge transfer integral at the precise instant of a charge carrier transfer.[21] Wang *et al*. obtained the time evolution of transfer integral by

calculating the transfer integrals of unique molecular pairs at the fixed geometry of each snapshot that was generated by molecular dynamics (MD).[1] They then performed a discrete Fourier transform of the time-dependent transfer integral fluctuations, $\Delta V = V(t) - \langle V \rangle$, to obtain a Fourier series representation of the transfer integral,

$$V(t) = V_0 + \sum_{k=0}^{N/2} \mathrm{Re}V_k \cos(\omega_k t + \varphi_0) + \sum_{k=0}^{N/2} \mathrm{Im}V_k \sin(\omega_k t + \varphi_0), \tag{3.21}$$

where V_0 is the transfer integral of the snapshot at time 0, N is the total number of snapshots, ReV and ImV are the amplitudes of cosine and sine basis functions, based on which contributions corresponding to different phonon frequencies ω_k can be obtained. The phase factor φ_0 can be chosen randomly because fluctuation correlation was hardly found between transfer integrals of different pairs.

Another method to incorporate thermal disorder in charge transfer integral is based on stochastic sampling, a method we devised during this project. Similar to the time evolution method, first we sample a large number of hopping pair configurations at various temperatures. To this end we carry out MD simulations based on the COMPASS force field that we used to validate the predicted crystal structures in previous chapter. We then calculate the transfer integrals of pairs for the geometries of a series of MD snapshots. From this data we compile a probability distribution and a corresponding cumulative distribution of the transfer integral that would be representative of any randomly chosen hopping pair configuration. The MD simulation is performed with a sufficiently long time (in total 500 steps) in order to cover all the possible values in the distribution. Figure 3.2. shows an example of a probability distribution function for

charge transfer integrals collected for such an MD trajectory. This distribution function is used to generate a statistical sampling of charge transfer integrals for the kinetic Monte Carlo procedure described next.

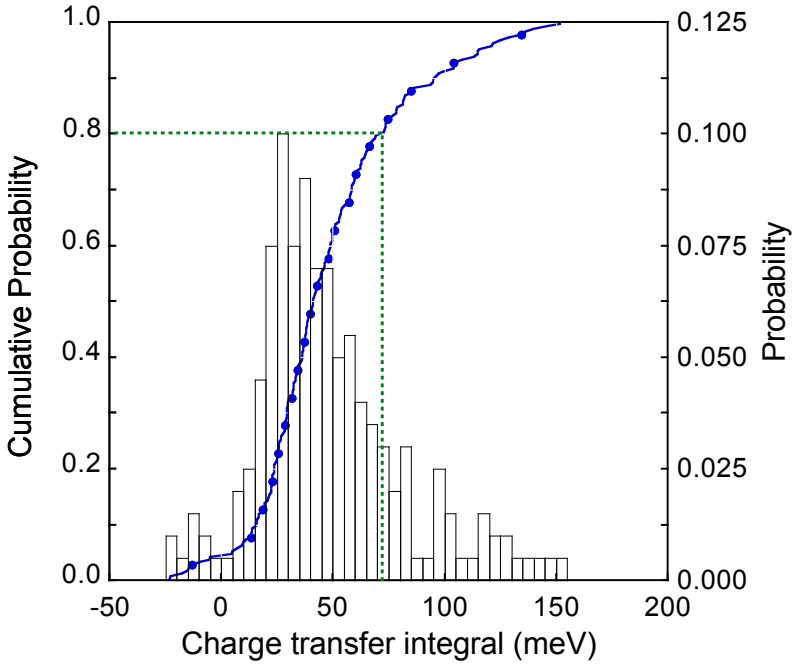

Figure 3.2. Description of the method for incorporating thermal disorder in charge transfer integral. (histogram) a typical probability distribution of charge transfer integral; (blue curve) the corresponding cumulative distribution (blue line); (green dashed lines) a random number 0.8 gives a charge transfer integral of 72 meV.

3.2.3. Simulated mobility based on kinetic Monte Carlo

Only one hopping step is insufficient to describe the charge transport property in a bulk parameter. A random walk based on a kinetic Monte Carlo algorithm is used to simulate the charge transport in a long range by creating a system with periodic boundary condition. Initially, the charge is assigned to a randomly chosen molecule *i*. The hopping rates for the charge from molecule *i* to all its neighbours (considering a total of *N*

neighbours) are calculated using equation 3.13. To this end we consider the local configuration of hopping sites surrounding the charge carrier, specifically the distance between hopping pairs and the relative orientation of the molecules to be stochastic quantities. Note that because the characteristic time for charge transfer is much less than that for thermal fluctuations, this configuration can be considered as invariant during the charge transfer.[11] For each pair we generate a random number r uniformly distributed between [0,1]. Based on this number we select a charge transfer integral magnitude as illustrated in Figure 3.2, by determining the abscissa associated with the random number projected onto the cumulative distribution. This value for V is then used when computing the hopping rate according to equation 3.13 for this specific pair at this time. The procedure is carried out for all neighbor pairs.

The final probability for the charge to hop from molecule i to one of the neighbouring molecules j is calculated as the rate of charge hopping from molecule i to molecule j, divided by the sum of the rates of charge hopping from molecule i to any of its neighbours, as given by equation 3.22,

$$P_j = k_{i\to j} \Big/ \sum_{n=1}^{N} k_{i\to n} \tag{3.22}$$

Next, another random number r, uniformly distributed between [0,1], is generated. The charge hops to the neighbouring molecule j if and only if satisfying equation 3.23 (Note that when j=1, the left side degrades to 0; when j=N, the right side becomes unity).

$$\sum_{n=1}^{j-1} P_n < r < \sum_{n=1}^{j} P_n \tag{3.23}$$

After determining the next position for the charge, the Monte-Carlo simulation time is increased by $1/k_{i\to j'}$ and the hopping distance along the electric field is recorded. The simulation continues until the total hopping distance along the electric field is equal or larger than a pre-set value (e.g., corresponding to the distance between two electrodes in experiments of measuring charge mobility, e.g. time-of-flight experiments[22]). Then the mobility is evaluated as

$$\mu = \frac{r_{tot}/t_{tot}}{F} \tag{3.24}$$

r_{tot} is the total hopping distance along the electric field and t_{tot} is the total travel time.

3.3. Results and Discussion

3.3.1. Huang-Rhys factors

Table 3.1–3.3 show the Huang-Rhys factors for pentacene and the two hybrid molecules. The calculation for pentacene is in good agreement with other theoretical results in the literature.[23] The Huang-Rhys factors S_j are strongly related to a key parameter used in semi-classical Marcus theory, namely the inner reorganization energy λ_{reo}, which represents the activation barrier due to the configurational adjustment of molecules during charge transfer. The characterization of the contributions of each vibrational frequency ω_j to inner reorganization energy, calculated as $\lambda_{reo} = S_j \hbar\omega_j$, is essential to rationalize the temperature dependence of the electron-transfer rates.[24] Alternatively, the inner reorganization energy can also be computed from the adiabatic potential energy surfaces (Figure 3.1(b)). Accordingly, $\lambda_{reo} = E_A^B - E_B + E_B^A - E_A$,

where E_A^B is the energy of the charge atom in the optimized uncharged geometry, E_B is the energy of the charge atom in the optimized charged geometry, E_B^A is the energy of the neutral molecule in the optimized charged geometry, and E_A is the energy of the neutral molecule in the optimized uncharged geometry. Table 3.4 shows that the two methods for calculating the reorganization energy give results those are in excellent agreement with each other. The calculated reorganization energy for hole transport in pentacene is close to the experimental value of 0.099 eV. The reorganization energy of dipentacene-SQ_8 is smaller than those of pentacene or monopentacene-SQ_8, indicating a smaller activation barrier due to deformation of the molecular structure during hole transitions. We also notice that the main contribution to the reorganization energy comes from high frequency modes, ranging from 1200 to 1600 cm^{-1}.

3.3.2. Charge transfer integral

Table 3.5 lists the charge transfer integrals for the hole hopping pairs that are identified as nearest neighbor pentacene molecules or hybrid molecule segments in the experimentally determined pentacene crystal structures[25] and in the two predicted hybrid crystals. The charge transfer integrals are calculated using a direct method described by Shuai *et al*.[21], when molecules are in their optimized configuration. As we can see, the calculated charge transfer integrals for hopping pairs in pentacene are comparable to those reported by Troisi and Orlandi.[26] By comparing the largest charge transfer integrals for pentacene and the hybrid molecular crystals, we find that for both hybrid molecular crystals they have larger magnitudes than that for pure pentacene, namely 205.46 meV for dipentacene-SQ_8 and 435.56 meV for monopentacene-SQ_8 , while the charge transfer

integral for pure pentacene is 135.70 meV. In general, we can expect enhanced transport property with larger charge transfer integral values. Accordingly, both hybrid molecular crystals should have a higher hole mobility than pentacene. In the next section we analyze in detail the decidedly distinct transport behaviors for these two hybrid molecular crystals.

To better account for the effect of the molecular thermal motion on the electronic charge transport in these organic and hybrid molecular crystals, we must assess the variations in the charge transfer integral that arise from the fact that at finite temperatures molecules are momentarily displaced from their ground state optimized configurations. In essence, due to the thermal motion the molecules that constitute a hopping pair are some of the time closer together and at other times farther apart; their relative orientation also varies. These fluctuations affect the orbital overlaps and, consequently, the charge hopping rates. They also affect exactly what neighboring atom the electron hole is most likely to transfer to, and thus, the overall charge migration trajectory. The computational methods have been detailed previously in section 1.2.2. Figure 3.3 shows the resulting distribution of charge transfer integrals for each crystal at 300K. As we can see, the distribution of charge transfer integral follows a Gaussian-like behavior, with the peak center, corresponding to the average value of the charge transfer integral located close to that of optimized ground state molecular structures. The fluctuations in charge transfer integrals are of the same order of magnitude as the average. These findings are all consistent with other theoretical work.[11,15] Taking pentacene as an example, we show the effect of temperature on the distribution of charge transfer integrals in Figure 3.4; as we increase the temperature, we obtain a flatter distribution. For the second step of our

procedure, we use these charge transfer integral distributions as input for a kinetic Monte Carlo simulation of long range hopping paths mapped onto the known or predicted crystal structures of our molecules under consideration.

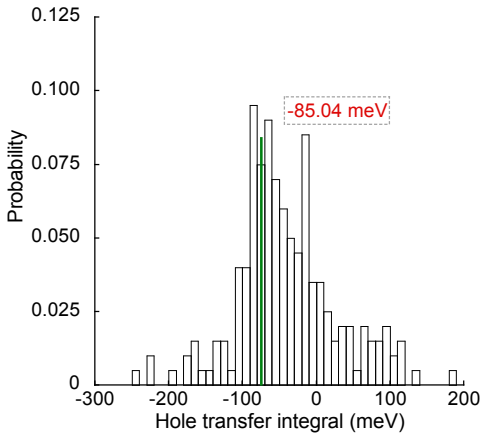

(a)

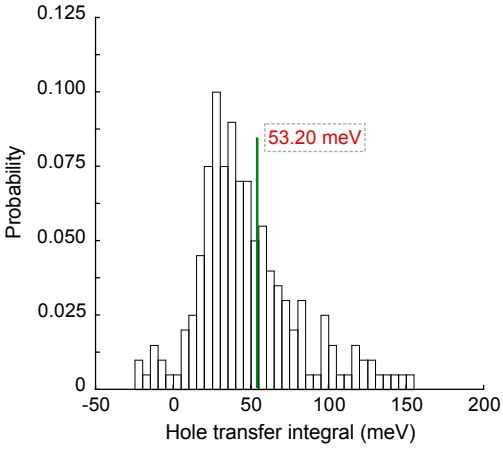

(b)

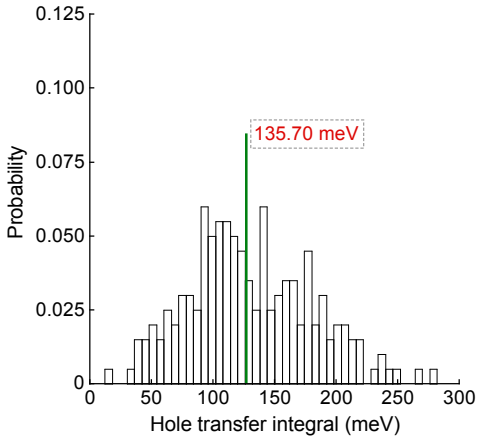

(c)

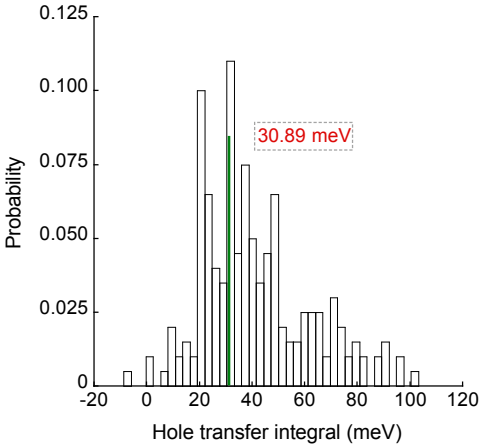

(d)

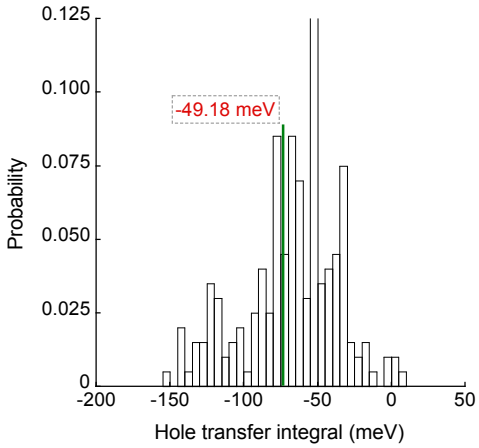
0.125
0.100
0.075
0.050
0.025
0
Probability
-49.18 meV
-200
-150
-100
-50
0
50
Hole transfer integral (meV)

(e)

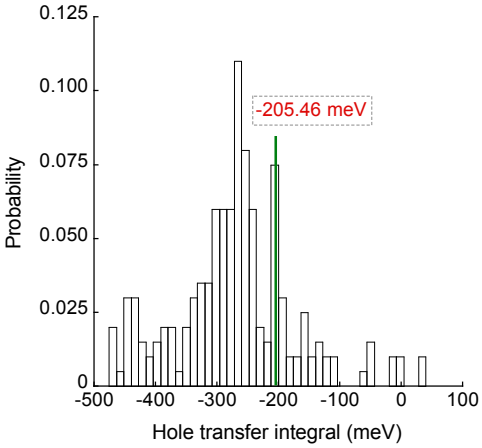
0.125
0.100
0.075
0.050
0.025
0
Probability
-205.46 meV
-500
-400
-300
-200
-100
0
100
Hole transfer integral (meV)

(f)

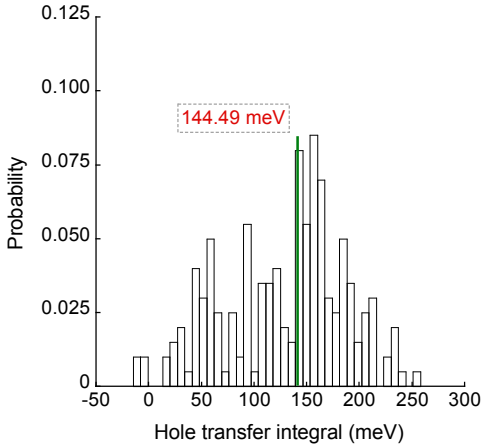
0.125
0.100
0.075
0.050
0.025
0
Probability
144.49 meV
-50
0
50
100
150
200
250
300
Hole transfer integral (meV)

(g)

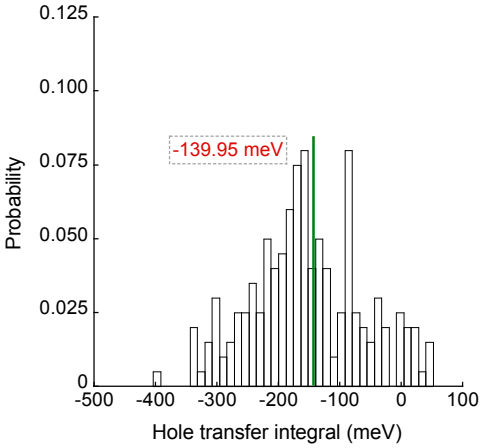
0.125
0.100
0.075
0.050
0.025
0
Probability
-139.95 meV
-500
-400
-300
-200
-100
0
100
Hole transfer integral (meV)

(h)

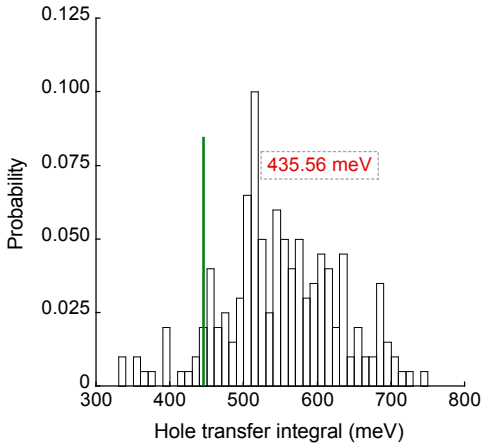

(i)

Figure 3.3. The distribution of hole transfer integrals in pentacene crystal, dipentacene-SQ_8 crystal, and monopentacene-SQ_8 crystal at 300K. (a)-(c): pentacene, (d)-(g): dipentacene-SQ_8, (h)-(i): monopentacene-SQ_8; the green line shows the hole transfer integral of the pair in the optimized configuration; only unique transfer integrals are presented.

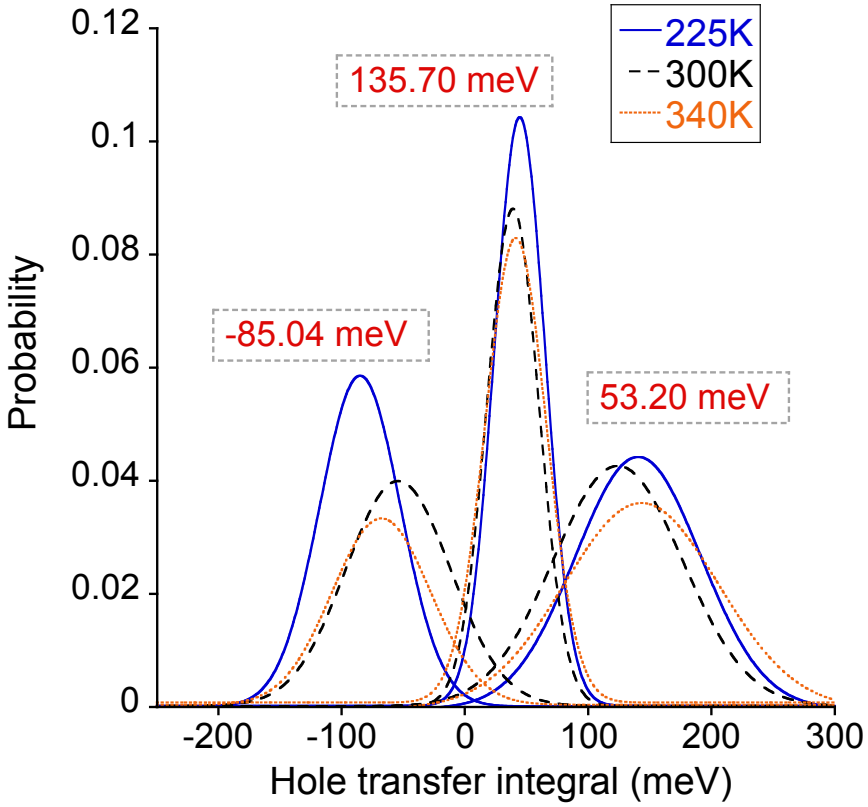

Figure 3.4. Fitted curves for hole transfer integrals in pentacene crystal at 225K, 300K and 340K.

3.3.3. Structure and hopping path dimensionality

The pentacene crystal is characterized by a layered structure. The charge mobility within the layers is larger than that between layers due to larger orbital overlap between molecules within layers. In the two hybrid crystals, the pentacene segments also form layers (Figure 3.5). In fact, the orbital overlap between pentacene segments in these crystals constitutes the majority of the interactions. Based on its structure, the dipentacene-SQ_8 crystal provides more pathways for carriers to hop into different directions. The charge transfer integrals associated with the various hopping pairs, listed in Table 3.5, also support this notion, so that we can expect a 3D transport behavior.

However, in crystalline monopentacene-SQ_8 carriers can only migrate in a specific direction, as shown in Figure 3.5(f). The predominant migration pathway has the linear pentacene segments stacked against only two other such units belonging to a different molecule, and they are positioned on opposite sides of the plane containing the central pentacene segment. This makes for two unique charge transfer pairs and a single migration direction.

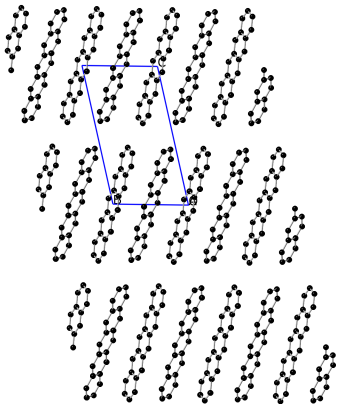

(a)

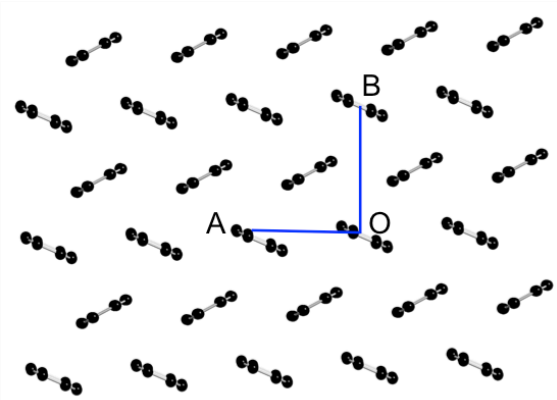

(d)

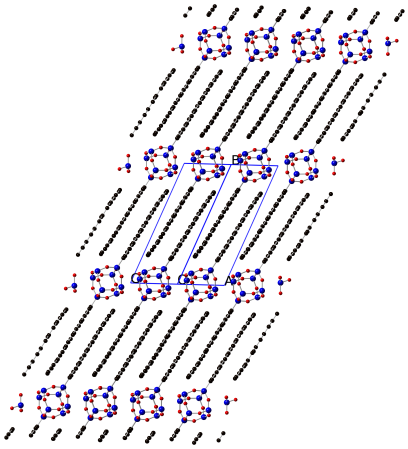

(b)

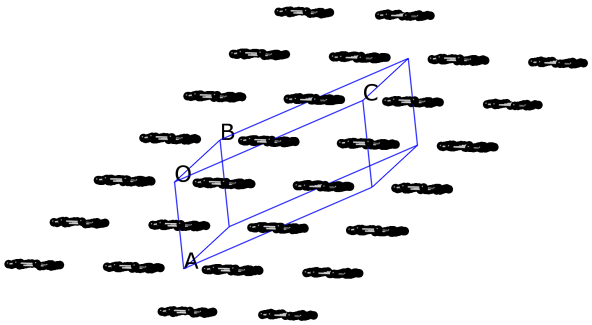

(e)

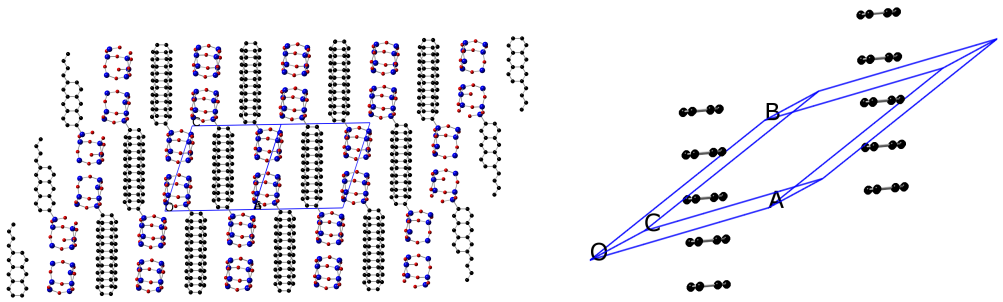

(c) (f)

Figure 3.5. Layered structures in (a) pentacene crystal, (b) dipentacene-SQ_8 crystal, (c) monopentacene-SQ_8 crystal, hydrogen atoms are omitted; arrangement of pentacene or pentacene segments in layers of (d) pentacene crystal, (e) dipentacene-SQ_8 crystal, (f) monopentacene-SQ_8 crystal, only carbon atoms are displayed.

3.3.4. Transport properties

First, we compare hole transport under the influence of an externally applied electric field along the OA and OB directions of pure crystalline pentacene. The electric field biases the hopping probability by means of shifting the free energy difference associated with a charge carrier jump, as expressed in equation 3.14, which affects the hopping rate coefficient through the first term of the exponential in equation 3.13. Finally, the formal definition of electron and hole mobility involves normalization with respect to the field strength, as shown in equation 3.24. We first validate our calculation approach by comparing the simulated results with experimental data for crystalline pentacene. After that, we extend our studies to the hole transport under an electric field in OA, OB, and OC directions in the two hybrid crystals.

The experimental hole mobility of pentacene crystal is determined from space-charge-limited current (SCLC) measurements,[2] with an applied electric field of around $2 \cdot 10^5$ V/m. Therefore, in our simulations we applied the same electric field strength to be consistent with the experimental conditions. The temperature dependence of the simulated conductivities arises from terms in the pertinent expression that possess inherent temperature dependences, as well as from the structural disorder due to thermal motion, accounted for as described in section 1.3.2. The simulation results are compared with experimental data in Figure 3.6, and the findings can be interpreted as following. First, the simulations yield higher hole mobilities than the experiments. However, note that our calculations are based on single crystals without any impurities or defects, and hence the mobilities obtained from simulations can be considered as an upper boundary. Second, the thermal disorder has great impact on the mobility behavior: (1) the simulation results with thermal disorder exhibit band-like behavior when the temperature is below 300K; and (2) the simulation results show a minimum in hole mobility around 300K. At higher temperatures, the hole mobility increases slightly or remains largely temperature independent. Both findings agree well with experimental data. This is in contrast to the findings from other theoretical investigations, which state that the band-like mobility behavior in 2-D is purely a nuclear tunneling effect.[10,11] According to our findings, the thermal disorder plays the principal role in yielding the band-like mobility behavior in 2-D. Overall, this comparison indicates that our refined hopping model is reliable for simulating charge transport in organic crystal materials.

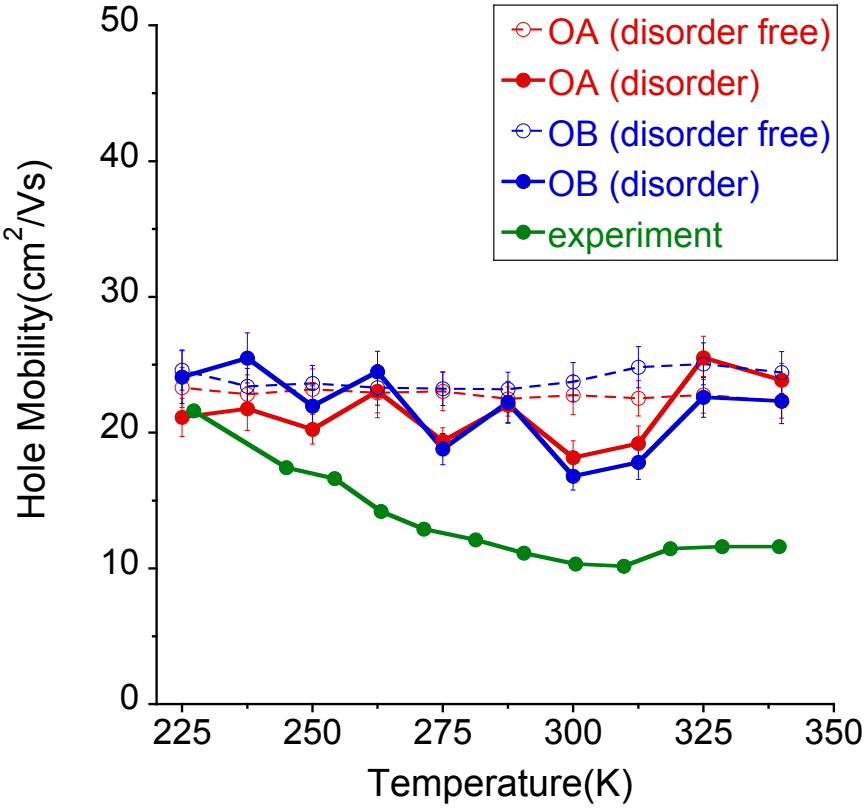

Figure 3.6. Comparison of simulation results (disorder and disorder free) and experimental data of hole mobility in pentacene crystal. The hole mobility is calculated along the same direction of the applied electric field, i.e. the crystallographic direction OA and OB of pentacene crystal.

Using the same electric field as for crystalline pentacene, the simulation of charge carrier mobilities in crystalline dipentacene-SQ_8 yields remarkable results. Accordingly, the predicted hole mobility in the dipentacene-SQ_8 crystal is two orders of magnitude larger than that in pure pentacene crystal (17 cm^2/Vs at 300 K), reaching values as high as 11775 cm^2/Vs at 300 K along OB direction (Figure 3.7). Comparing the hole mobility absent of thermal disorder in the three crystallographic directions, the predominant hole mobility is obtained along the OB direction. This is because the preferred hopping direction in the dipentacene-SQ_8, i.e., the one that exhibits the largest hole transfer

integral (205 meV), is close to OB direction. The SQ_8 cages in the hybrid molecules do not make direct significant contributions to the high hole mobility. However, its rigidity and three-dimensional structure restrict the orientation of the functional groups. In the case of dipentacene-SQ_8 , the pentacene segments adopt a parallel configuration such that the hole transfer integral is larger than that in the herringbone structure seen for pristine crystalline pentacene. Comparing the simulated results with and without thermal disorder, we find that the hole mobility along OB, the most favored direction for hole hopping, is decreased upon imposing thermal disorder. This is because thermal disorder has detrimental influence on the superiority of that direction by randomizing the structural anisotropy of the system, and thus balancing the probability of hole hopping between different directions, leading to a reduced hole mobility along the same direction. The hole mobilities along less favored directions should also be affected by thermal disorder, but it is difficult to predict their trends before carrying out kinetic Monte Carlo simulations. In the case of dipentacene-SQ_8, the hole mobility along OA is slightly increased after adding thermal disorder while that of OC is decreased. Moreover, we observe band-like behavior of the hole mobilities for all three directions, regardless of whether we take thermal disorder into account. Compared to that in pentacene crystal, the band-like behavior of the hole mobility in dipentacene-SQ_8 crystal is much less affected by the thermal disorder, but it can be seen as a consequence of the nuclear tunneling effect.

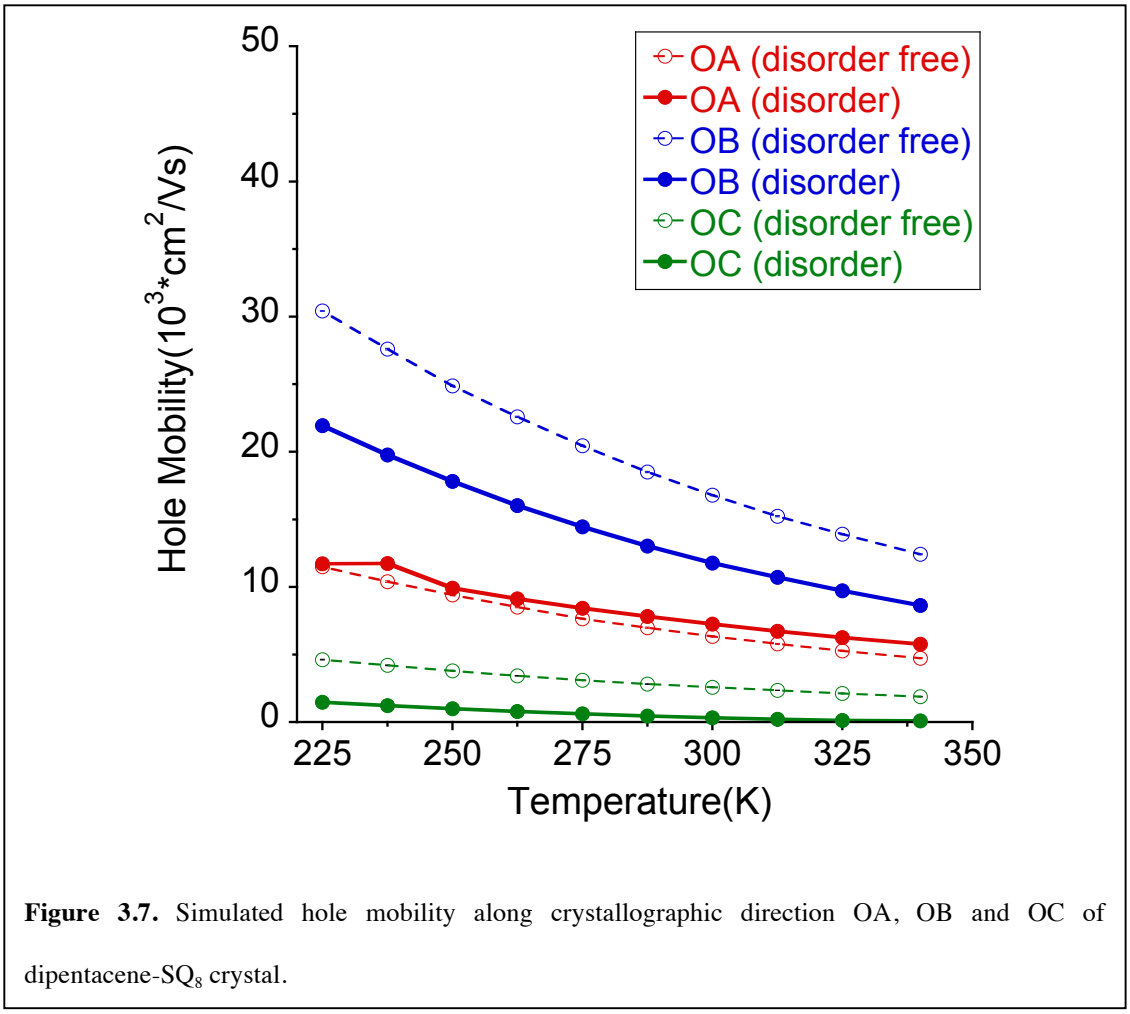

Figure 3.7. Simulated hole mobility along crystallographic direction OA, OB and OC of dipentacene-SQ_8 crystal.

The simulated hole mobility of monopentacene-SQ_8 crystal is shown in Figure 3.8. Surprisingly, larger transfer integrals in monopentacene-SQ_8 compared to those in pentacene or dipentacene-SQ_8 crystal fail to result in larger hole mobilities. In fact, only the largest hole mobility along OB direction is comparable to that in the pure pentacene crystal. This behavior can be explained by the "bottleneck effect" illustrated in other theoretical work such as by Wang et al.[11] They studied the system of a 1-D packing of pentacene molecules, where only two unique hopping pairs exist and are positioned in an alternating form along the 1-D transport conduits. They found that charges oscillate between the sites of a pentacene hopping pair with the larger charge transfer rate. In our

case of monopentacene-SQ_8, we also have a similar 1-D "alternating" configuration roughly aligned with OB direction, where the two charge transfer integrals are 435.56 meV and –139.55 meV. Indeed, the hole transfer rate for the pair with a transfer integral of 435.56 meV is nearly 9 times larger than that of the other pair with a transfer integral of –139.55 meV. The strong oscillation in the pair with the larger transfer integral substantially compromises the speed of charge migration in the monopentacene-SQ_8 crystal, and consequently leads to an inefficient charge transport. Taking thermal disorder into account alleviates this bottleneck effect by reducing the difference of the two charge transfer rates on a time average, which leads to an enhanced hole mobility along OB direction, as is shown in Figure 3.8. Also, the magnitude of hole mobilities along less favored directions, OA and OC, is slightly altered by thermal disorder.

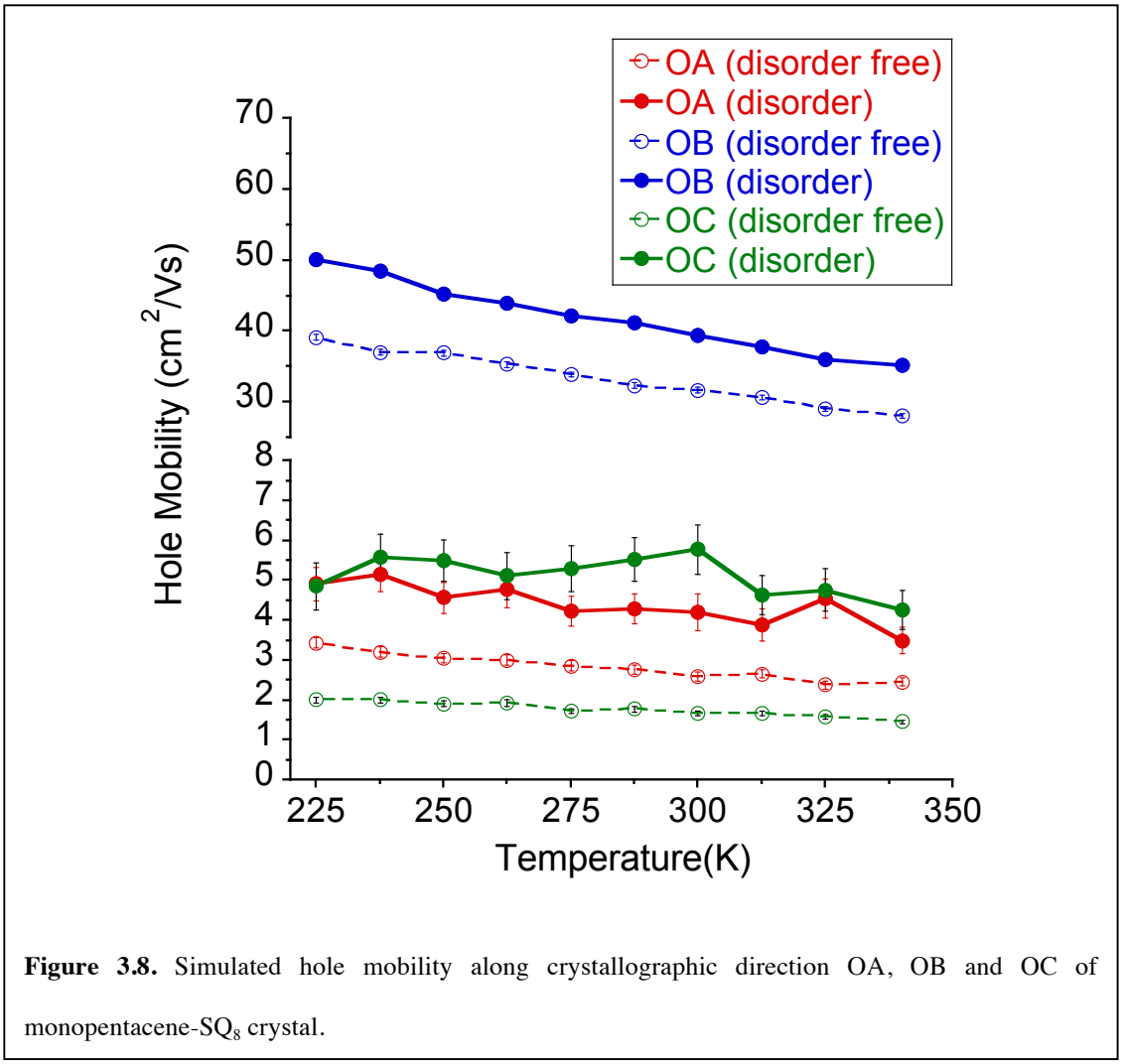

Figure 3.8. Simulated hole mobility along crystallographic direction OA, OB and OC of monopentacene-SQ_8 crystal.

3.4. Conclusions

We developed a multi-scale hopping model based on Fermi's golden rule to simulate the charge transport in organic crystals. The simulated hole mobility of crystalline pentacene successfully reproduces the previous experimental result by using our model. The simulated hole mobility in dipentacene-SQ_8 crystal can be up to two orders of magnitude larger than that in pentacene, reaching 11775 cm^2/Vs at 300K. The simulated hole mobility of monopentacene-SQ_8 does not show good enhancement of hole mobility compared to that in pentacene, which is mainly due to the bottleneck effect for 1-D

system. Thermal disorder plays a great role in each of the studied crystals. For pentacene, it facilitates the formation of band-like behavior of hole mobility; for dipentacene-SQ_8, it decreases the hole mobility in the most favored direction for hole hopping by balancing the probability of hole hopping in different directions; for monopentacene-SQ_8, it increases the hole mobility in the most favored direction for hole hopping by breaking the bottleneck effect. Overall, these simulation results shine light on the practical use of computational materials design at molecular level.

Table 3.1. B3LYP/6-31G* calculations of vibrational frequencies ω (cm^{-1}), Huang-Rhys factors S, and partial/total reorganization energy λ_{reo} (meV), for pentacene in neutral and cation state.

Neutral			Cation		
ω (cm^{-1})	S	λ_{reo} (meV)	ω (cm^{-1})	S	λ_{reo} (meV)
264	0.028	0.92	263	0.027	0.88
617	0.000	0.00	613	0.000	0.00
765	0.001	0.09	765	0.000	0.00
800	0.002	0.20	807	0.001	0.10
1030	0.003	0.38	1048	0.002	0.26
1194	0.011	1.63	1205	0.017	2.54
1223	0.045	6.82	1233	0.044	6.73
1348	0.000	0.00	1341	0.004	0.67
1426	0.065	11.49	1427	0.002	0.35
1450	0.010	1.80	1442	0.084	15.02
1512	0.002	0.37	1521	0.000	0.00
1571	0.089	17.33	1564	0.056	10.86
1594	0.010	1.98	1592	0.030	5.92
3181	0.000	0.00	3200	0.000	0.00
3185	0.000	0.00	3206	0.000	0.00
3211	0.000	0.00	3229	0.000	0.00
Total		43.02			43.32

Table 3.2. B3LYP/6-31G* calculations of vibrational frequencies ω (cm^{-1}), Huang-Rhys factors S, and partial/total reorganization energy λ_{reo} (meV), for dipentacene-SQ_8 in neutral and cation state.

Neutral			Cation		
ω (cm^{-1})	S	λ_{reo} (meV)	ω (cm^{-1})	S	λ_{reo} (meV)
19	0.016	0.04	20	0.015	0.04
70	0.061	0.53	70	0.071	0.62
76	0.039	0.37	76	0.028	0.26
160	0.001	0.02	160	0.001	0.02
184	0.003	0.07	185	0.003	0.07
212	0.003	0.08	212	0.003	0.08
273	0.002	0.07	273	0.002	0.07
338	0.001	0.04	338	0.001	0.04
380	0.001	0.05	380	0.002	0.09
413	0.059	3.02	414	0.05	2.57
417	0.018	0.93	418	0.027	1.40
449	0.011	0.61	448	0.008	0.44
463	0.003	0.17	461	0.003	0.17
504	0.001	0.06	502	0.001	0.06
525	0.001	0.07	522	0.001	0.06
583	0.001	0.07	583	0.001	0.07
589	0.003	0.22	590	0.002	0.15
640	0.001	0.08	637	0.001	0.08
679	0.008	0.67	677	0.008	0.67
762	0.001	0.09	752	0.001	0.09
767	0.001	0.10	763	0.001	0.09
809	0.004	0.40	767	0.001	0.10
907	0.002	0.22	812	0.004	0.40
1028	0.001	0.13	904	0.002	0.22
1136	0.029	4.08	1039	0.001	0.13

1141	0.004	0.57	1117	0.002	0.28
1156	0.001	0.14	1133	0.03	4.21
1196	0.002	0.30	1145	0.001	0.14
1223	0.02	3.03	1202	0.004	0.60
1227	0.004	0.61	1227	0.013	1.98
1323	0.001	0.16	1230	0.012	1.83
1345	0.002	0.33	1342	0.003	0.50
1357	0.001	0.17	1398	0.001	0.17
1407	0.004	0.70	1411	0.002	0.35
1427	0.032	5.66	1433	0.03	5.33
1446	0.001	0.18	1440	0.009	1.61
1452	0.002	0.36	1441	0.002	0.36
1471	0.001	0.18	1565	0.016	3.10
1573	0.045	8.78	1572	0.019	3.70
1579	0.001	0.20	1587	0.01	1.97
1595	0.003	0.59	1593	0.001	0.20
1678	0.001	0.21	1665	0.001	0.21
Total		34.36			34.54

Table 3.3. B3LYP/6-31G* calculations of vibrational frequencies ω (cm^{-1}), Huang-Rhys factors S, and partial/total reorganization energy λ_{reo} (meV), for monopentacene-SQ_8 in neutral and cation state.

Neutral			Cation		
ω (cm^{-1})	S	λ_{reo} (meV)	ω (cm^{-1})	S	λ_{reo} (meV)
15	0.007	0.01	16	0.013	0.03
71	0.003	0.03	72	0.003	0.03
91	0.059	0.67	89	0.048	0.53
97	0.139	1.67	96	0.13	1.55
147	0.014	0.26	147	0.012	0.22
164	0.001	0.02	164	0.001	0.02
207	0.016	0.41	206	0.016	0.41
276	0.018	0.62	276	0.017	0.58
284	0.001	0.04	285	0.001	0.04
288	0.007	0.25	287	0.004	0.14
332	0.002	0.08	331	0.002	0.08
378	0.003	0.14	379	0.003	0.14
394	0.014	0.68	395	0.023	1.13
395	0.01	0.49	396	0.01	0.49
404	0.005	0.25	403	0.006	0.30
412	0.217	11.08	411	0.195	9.94
415	0.025	1.29	415	0.004	0.21
452	0.121	6.78	443	0.012	0.66
457	0.002	0.11	454	0.054	3.04
463	0.01	0.57	455	0.043	2.43
503	0.002	0.12	460	0.032	1.83
564	0.002	0.14	499	0.002	0.12
566	0.032	2.25	564	0.022	1.54
583	0.001	0.07	566	0.018	1.26
592	0.003	0.22	583	0.002	0.14

616	0.005	0.38	593	0.001	0.07
640	0.004	0.32	611	0.004	0.30
677	0.038	3.19	634	0.004	0.31
748	0.002	0.19	669	0.001	0.08
761	0.005	0.47	671	0.032	2.66
767	0.002	0.19	754	0.003	0.28
809	0.011	1.10	764	0.003	0.28
849	0.001	0.11	766	0.001	0.09
895	0.003	0.33	814	0.007	0.71
898	0.029	3.23	847	0.001	0.11
906	0.003	0.34	893	0.037	4.10
1028	0.002	0.25	902	0.002	0.22
1108	0.002	0.27	1047	0.001	0.13
1122	0.025	3.48	1099	0.064	8.72
1135	0.099	13.93	1129	0.071	9.94
1142	0.003	0.42	1145	0.002	0.28
1150	0.027	3.85	1155	0.011	1.58
1156	0.001	0.14	1158	0.002	0.29
1197	0.004	0.59	1195	0.002	0.30
1214	0.001	0.15	1208	0.009	1.35
1223	0.042	6.37	1228	0.008	1.22
1227	0.007	1.06	1233	0.043	6.57
1323	0.001	0.16	1311	0.001	0.16
1345	0.004	0.67	1322	0.001	0.16
1357	0.001	0.17	1338	0.007	1.16
1379	0.001	0.17	1361	0.001	0.17
1407	0.008	1.40	1401	0.001	0.17
1428	0.065	11.51	1417	0.003	0.53
1446	0.001	0.18	1427	0.004	0.71
1453	0.007	1.26	1433	0.003	0.53

1472	0.002	0.37	1441	0.085	15.19
1508	0.001	0.19	1474	0.001	0.18
1553	0.001	0.19	1557	0.02	3.86
1573	0.086	16.77	1568	0.033	6.42
1579	0.004	0.78	1571	0.007	1.36
1595	0.004	0.79	1582	0.001	0.20
1606	0.001	0.20	1590	0.025	4.93
1678	0.002	0.42	1646	0.002	0.41
Total		103.85			102.57

Table 3.4. Hole reorganization energies λ of pentacene, dipentacene-SQ_8 and monopentacene-SQ_8 calculated at the B3LYP/ 6-31G* Level. AP: calculated from the adiabatic potential (AP) surfaces for the neutral and charged species. NM: calculated from normal mode (NM) analysis. EXP: measured in the experiment.[27]

	λ_{reo} (eV)		
	AP	NM	EXP
pentacene	0.089	0.086	0.099
dipentacene-SQ_8	0.071	0.069	--
monopentacene-SQ_8	0.215	0.206	--

Table 3.5. Calculation results of charge transfer integrals for hole hopping in pentacene, dipentacene-SQ_8 and monopentacene-SQ_8 at B3LYP/6-31G* level. Data in parenthesis are from literature.[26] The negative sign for some values is only a numerical factor.

Pentacene					
Hopping couples		Hopping direction			*V* (meV)
M_1	M_2	OA	OB	OC	
a	a	1	0	0	53.20 (49.7)
b	b	1	0	0	57.97 (51.0)
a	b	0	0	0	–85.04 (74.4)
a	b	1	0	0	135.68
a	b	0	1	0	135.70 (130.1)
a	b	1	1	0	–85.02
dipentacene-SQ_8					
Hopping couples		Hopping direction			*V* (meV)
M_1	M_2	OA	OB	OC	
a	a	0	1	0	30.89
a	a	1	1	0	–31.88
a	b	0	1	1	–205.46
a	b	1	1	1	–49.18
b	b	0	1	0	144.49
b	b	1	1	0	–146.49
monopentacene-SQ_8					
Hopping couples		Hopping direction			*V* (meV)

M_1	M_2	OA	OB	OC	
a	b	0	1	0	435.56
a	a	1	1	0	–139.55

3.5. References

1. Wang, L. et al. Computational methods for design of organic materials with high charge mobility. *Chem. Soc. Rev.* **39**, 423-434 (2010).
2. Jurchescu, O. D., Baas, J. & Palstra, T. T. M. Effect of impurities on the mobility of single crystal pentacene. *Appl. Phys. Lett.* **84**, 3061-3063 (2004).
3. Podzorov, V. et al. Intrinsic charge transport on the surface of organic semiconductors. *Phys. Rev. Lett.* **93**, (2004).
4. Podzorov, V., Menard, E., Rogers, J. A. & Gershenson, M. E. Hall effect in the accumulation layers on the surface of organic semiconductors. *Phys. Rev. Lett.* **95**, (2005).
5. Cheng, Y. C. et al. Three-dimensional band structure and bandlike mobility in oligoacene single crystals: A theoretical investigation. *J. Chem. Phys.* **118**, 3764-3774 (2003).
6. MARCUS, R. A. ELECTRON-TRANSFER REACTIONS IN CHEMISTRY - THEORY AND EXPERIMENT. *Rev. Mod. Phys.* **65**, 599-610 (1993).
7. Bredas, J. L., Calbert, J. P., da, S., DA & Cornil, J. Organic semiconductors: A theoretical characterization of the basic parameters governing charge transport. *Proc. Natl. Acad. Sci. U. S. A.* **99**, 5804-5809 (2002).
8. Deng, W. Q. & Goddard, W. A. Predictions of hole mobilities in oligoacene organic semiconductors from quantum mechanical calculations. *J. Phys. Chem. B* **108**, 8614-8621 (2004).
9. Yang, X., Li, Q. & Shuai, Z. Theoretical modelling of carrier transports in molecular semiconductors: molecular design of triphenylamine dimer systems. *Nanotechnology* **18**, (2007).
10. Nan, G., Yang, X., Wang, L., Shuai, Z. & Zhao, Y. Nuclear tunneling effects of charge transport in rubrene, tetracene, and pentacene. *Phys. Rev. B* **79**, (2009).
11. Wang, L., Li, Q., Shuai, Z., Chen, L. & Shi, Q. Multiscale study of charge mobility of organic semiconductor with dynamic disorders. *Phys. Chem. Chem. Phys.* **12**, 3309-3314 (2010).
12. Wang, L. J., Peng, Q., Li, Q. K. & Shuai, Z. Roles of inter- and intramolecular vibrations and band-hopping crossover in the charge transport in naphthalene crystal. *J. Chem. Phys.* **127**, (2007).
13. Coropceanu, V., Sanchez-Carrera, R. S., Paramonov, P., Day, G. M. & Bredas, J.-L. Interaction of Charge Carriers with Lattice Vibrations in Organic Molecular Semiconductors: Naphthalene as a Case Study. *J. Phys. Chem. C* **113**, 4679-4686 (2009).
14. Troisi, A. & Orlandi, G. Charge-transport regime of crystalline organic semiconductors: Diffusion limited by thermal off-diagonal electronic disorder. *Phys. Rev. Lett.* **96**, (2006).
15. Troisi, A. & Orlandi, G. Dynamics of the intermolecular transfer integral in crystalline organic semiconductors. *J. Phys. Chem. A* **110**, 4065-4070 (2006).
16. JORTNER, J. TEMPERATURE-DEPENDENT ACTIVATION-ENERGY FOR ELECTRON-TRANSFER BETWEEN BIOLOGICAL MOLECULES. *J. Chem. Phys.* **64**, 4860-4867 (1976).
17. Lin, S. H. et al. Ultrafast dynamics and spectroscopy of bacterial photosynthetic

reaction centers. **121**, 1-88 (2002).
18. Reimers, J. R. A practical method for the use of curvilinear coordinates in calculations of normal-mode-projected displacements and Duschinsky rotation matrices for large molecules. *J. Chem. Phys.* **115**, 9103-9109 (2001).
19. Coropceanu, V. et al. Charge transport in organic semiconductors. *Chem. Rev.* **107**, 926-952 (2007).
20. Lin, B. C., Cheng, C. P., You, Z. Q. & Hsu, C. P. Charge transport properties of tris(8-hydroxyquinolinato)aluminum(III): Why it is an electron transporter. *J. Am. Chem. Soc.* **127**, 66-67 (2005).
21. Shuai, Z., Geng, H., Xu, W., Liao, Y. & Andre, J.-M. From charge transport parameters to charge mobility in organic semiconductors through multiscale simulation. *Chem. Soc. Rev.* **43**, 2662-2679 (2014).
22. KEPLER, R. G. CHARGE CARRIER PRODUCTION AND MOBILITY IN ANTHRACENE CRYSTALS. **119**, 1226-1229 (1960).
23. Malagoli, M., Coropceanu, V., da, S., DA & Bredas, J. L. A multimode analysis of the gas-phase photoelectron spectra in oligoacenes. *J. Chem. Phys.* **120**, 7490-7496 (2004).
24. Coropceanu, V., Andre, J. M., Malagoli, M. & Bredas, J. L. The role of vibronic interactions on intramolecular and intermolecular electron transfer in pi-conjugated oligomers. *Theor. Chem. Acc.* **110**, 59-69 (2003).
25. Mattheus, C. C. et al. Polymorphism in pentacene. *Acta Crystallogr. Sect. C-Cryst. Struct. Commun.* **57**, 939-941 (2001).
26. Troisi, A. & Orlandi, G. Band structure of the four pentacene polymorphs and effect on the hole mobility at low temperature. *J. Phys. Chem. B* **109**, 1849-1856 (2005).
27. Coropceanu, V. et al. Hole- and electron-vibrational couplings in oligoacene crystals: Intramolecular contributions. *Phys. Rev. Lett.* **89**, (2002).

Chapter 4. Design principles for energy level tuning in donor/acceptor conjugated polymers

4.1. Introduction

Conjugated polymers (CPs) are widely used in organic photovoltaic (OPV) devices. The power conversion efficiency of these systems has been enhanced above 6 %.[1] However, the optical energy gaps of conventional organic materials are normally larger than 2 eV, covering only the visible range of the solar spectrum (300-650 nm).[2,3] Smaller energy gap organic materials are in demand to extend absorption to the long wavelength region (600~800 nm). Accordingly, the broadened absorption spectrum of CPs can take advantage of the red light or high photon flux region of the solar spectrum, thus contributing to more efficient solar energy harvesting. Therefore it has been one of the major efforts to design and synthesize novel conjugated polymers with narrow energy gaps in recent years. There are three major ways to modify the energy gap: (i) enlargement of the π orbital systems;[4] (ii) transition from aromatic to quinoidal structures;[5] and (iii) incorporation of alternating donor/acceptor functional units.[5] While they are very efficient in engineering energy gaps, both (i) and (ii) have the detrimental effect of increasing HOMO energy levels, resulting in a decrease in the open circuit voltage (Voc). Method (iii) overcomes this problem by integrating donor (electron-rich) and acceptor (electron-deficient or electron-poor) units into one system. This combined donor-acceptor (D-A) strategy is now widely used to design efficient polymer

photovoltaic materials. In such copolymer systems, alternating units strong enough to make the respective HOMO and LUMO levels close would yield a low energy gap polymer.[6] Theoretically, this is due to the reduction of bond-length alternation by increasing the double-bond character between the repeat units of a CP.[7] The interaction between a strong electron donor (D) and a strong electron acceptor (A) may also give rise to an increased double bond character between these units, since they can accommodate the charges that are associated with such a mesomerism ($D+A \rightarrow D^{+}+A^{-}$).[8] Consequently, a decreased energy gap could be obtained in a conjugated polymer with an alternating sequence of the appropriate donor and acceptor units.

Recently, Kim *et al*. have systematically explored a series of CPs by varying the acceptor units while keeping the donor unit unchanged.[9] The measured energy levels indicate that a stronger electron-withdrawing acceptor unit lowers both the highest occupied molecular orbital (HOMO) and the lowest unoccupied molecular orbital (LUMO) levels of the CP. However, the drop in the LUMO level is significantly more pronounced than that in the HOMO level, resulting in the CP's energy gap narrowing. Compared to the change in the LUMO level, the HOMO level appears to be nearly stagnant and mainly determined by the nature of the donor unit. The phenomenon of energy gap narrowing due to the variation of acceptor units could also be verified by the blue shift on absorption spectrum shown in the same study.

In the present investigation, first-principles calculations are used to systematically investigate the aforementioned phenomena and to elucidate the design principles for conjugated polymer systems. By summarizing key factors influencing the frontier orbital

energy levels and the energy gap , important principles to design D–A copolymers are highlighted. This chapter is organized as follows: in Section 4.2, a brief description of the theory and computational details is given. Subsequently, the four D-A polymers with the same donor unit and varied acceptor units (Figure 4.1), previously synthesized by Kim et al.,[9] are studied. In Section 4.3, structures, HOMO-LUMO levels and energy gaps of the isolated donors, the isolated acceptors, the D-A oligomer and the synthesized D-A

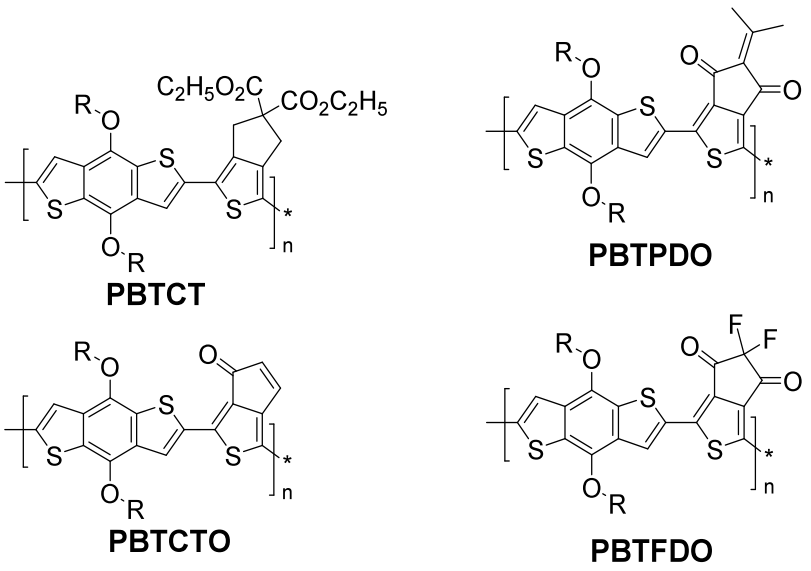

Figure 4.1. The synthesized polymers.

polymers, as well as the role of charge localization and intramolecular charge transfer are discussed in detail. After ascertaining consistency between our simulation results and the experimental findings for the known systems, we expand our study to include a set of newly conceived CPs that allow us to vary the donor units while maintaining the same acceptor unit. This allows us to further validate the mechanisms responsible the observed behaviors, and identify robust molecular design criteria for energy level tuning in CPs. Finally, a summary is given in Section 4.4.

4.2. Computational details

The electronic structure and properties of the conjugated polymers were investigated using density functional theory (DFT) calculations in Gaussian09[10], with the hybrid functional B3LYP and fully periodic boundary conditions (PBC) to obtain accurate electronic energy gaps for these conjugated polymers. For the optimized geometries, a electronic structure calculations were performed with a larger 6-311G(d,p) basis set using 5 k-points along the one dimensional Brillouin zone. The energy gap of a polymer is calculated as the minimum difference between the HOMO and the LUMO energy levels at a given k-point, while the energy levels of the HOMO and LUMO are determined from the maximum point of the HOMO and the minimum point of the LUMO, respectively. The Mulliken[11] charge distribution on each atom is also obtained after optimizing the structure in gas phases within DFT calculations.

4.3. Results and discussion

4.3.1. Varying the acceptor in conjugated oligomers or polymer for a given donor

The degree of planarity within the conjugated backbone not only influences the electronic and optical properties considerably, but from a practical computational viewpoint, it can also affect the cost associated with the calculations and analysis of longer oligomers.[12] Therefore, CP backbones are constructed from thiophene derivatives to ensure a rigid-planar conformation. Figure 4.2 shows all the polymers that have been synthesized by Kim et al.,[9] i.e. PBTCT, PBTCTO, PBTPDO, and PBTFDO, have exactly the same zig-zag shaped backbone geometry. Among them, PBTCT and PBTCTO exhibit twist angles between the D-A repeating units of 7.5° and 7.9°, respectively, which

are slightly larger than for the other polymers (≈1°–3°). An additional geometric

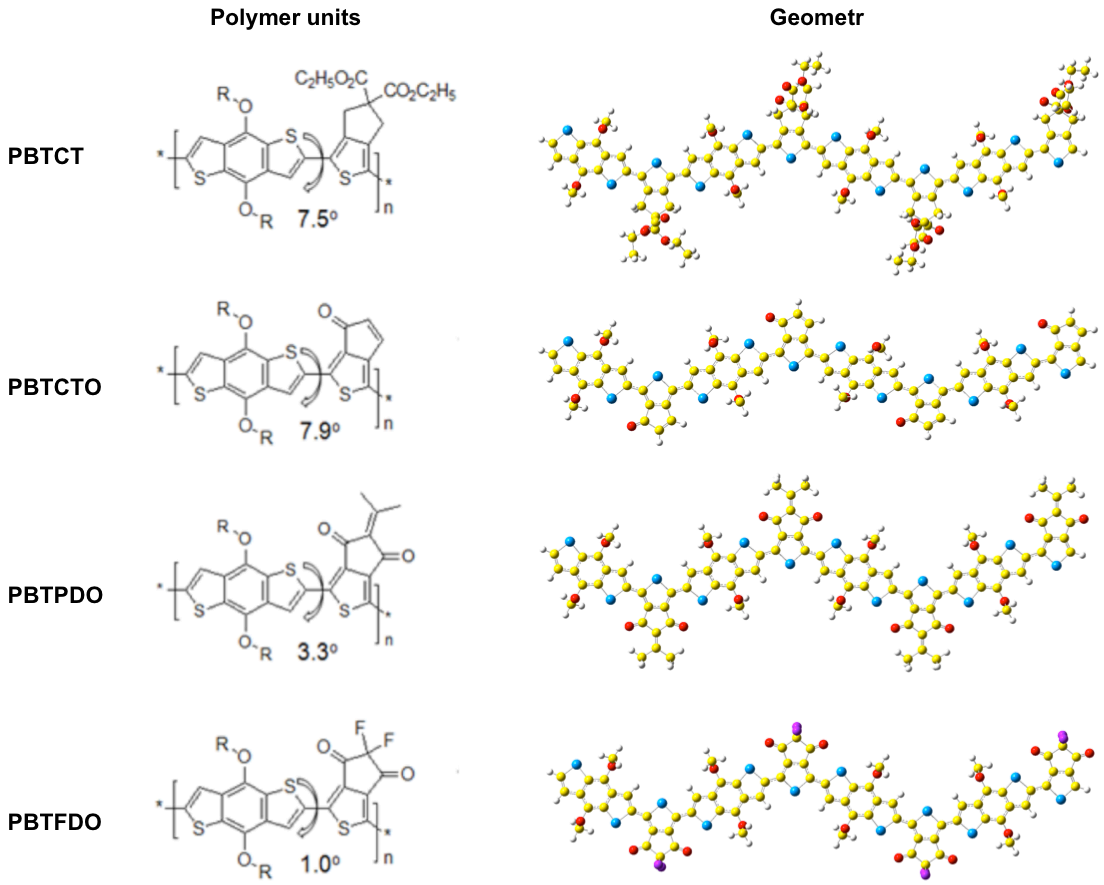

Figure 4.2. Chain conformations of the CPs, obtained from the tetramer conformation calculation under minimized energy state.

consideration concerns the orientation of the individual components along the conjugated backbone. As donor–acceptor components often contain heteroatoms, the possibility exists that intramolecular van der Waals and electrostatic interactions stabilize particular configurations.[13,14] For testing purpose, we studied the

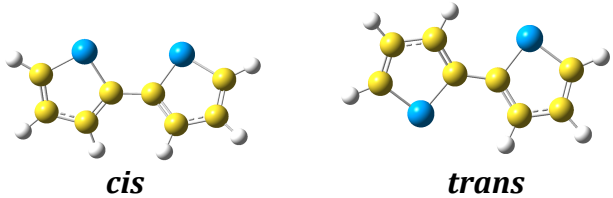

Figure 4.3. The *cis* and *trans* conformations of the bithenyl oligomer.

bithenyl oligomer that consists of two adjacent thiophene units. Depending on the way of positioning these two thiophene units, we can have two types of conformation, i.e., *cis* and *trans*, as shown in Figure 4.3. According to our calculation, the *trans* is energetically more stable by 10 meV than the *cis* in the gas phase. This is mainly because the *cis* conformation causes the lone pairs of the two sulfur atoms to repel each other, and therefore is less favorable. Therefore we built the backbone of the polymers with a *trans* conformation initially and later optimize it with DFT calculation.

The hybridization of molecular orbitals as a result of combining different monomeric groups may lead to unexpected new energy levels. This is because the HOMO/LUMO levels strongly depend on the degree of electron delocalization within the CP's effective conjugation length,[15] which is inevitably affected by the conformation of the backbone.[16,17] Therefore, the energy gap of a CP may not be predicted simply by the frontier orbital energy levels (i.e. HOMO, LUMO) of the donor unit or acceptor unit. To identify the governing principles more clearly, we begin by comparing the frontier orbital energy levels of the simplest oligomer, a single D-A repeating unit or monomer, with those of the constituting donor unit and acceptor unit. Figure 4.4 shows the structures of the donor unit and four different acceptor units. We also include a donor-donor (D-D) oligomer and acceptor-acceptor (A-A) oligomer in our comparison. As shown in Figure 4.5, our calculations reveal that upon combining a donor and an acceptor unit into a single D-A repeat unit, the resulting HOMO level very closely corresponds to that of the isolated donor unit and the LUMO level to that of the isolated acceptor unit, in almost all cases. The only exception we observed is the PBTCT monomer, which can be explained by the comparable electron donating strength of the donor and acceptor in this molecule.

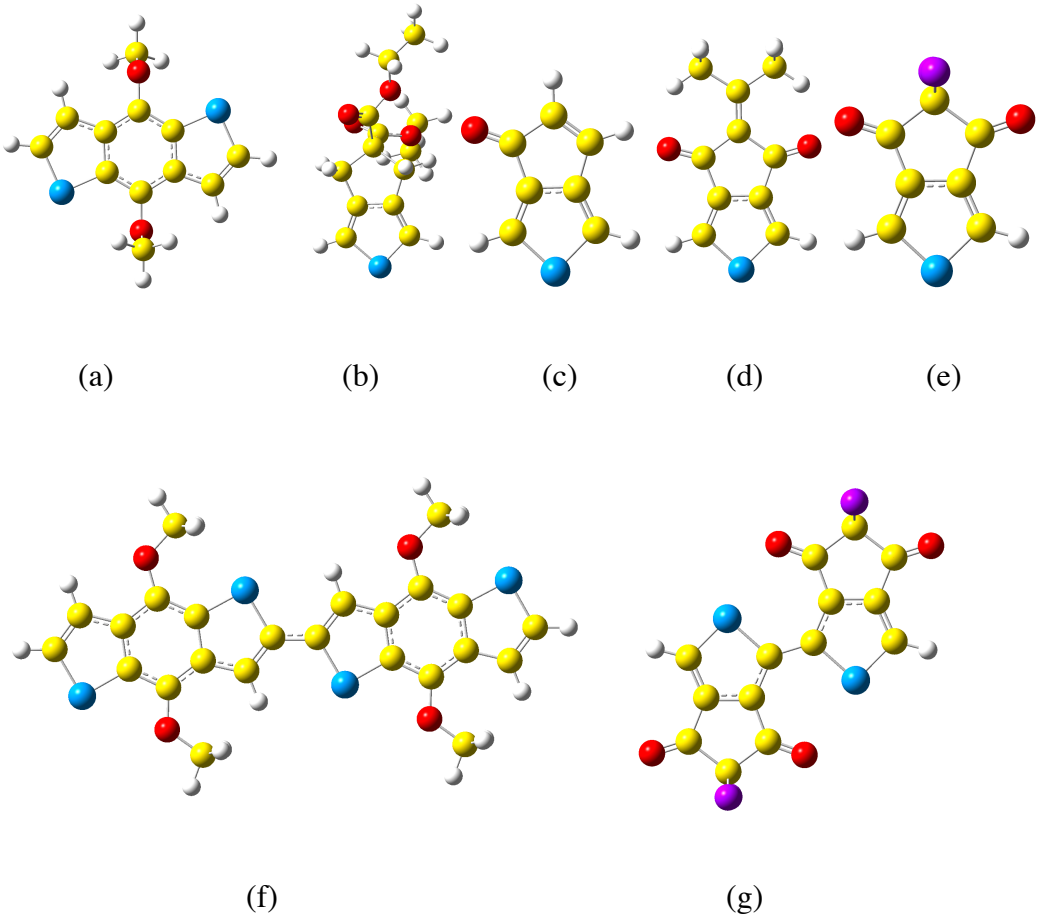

Figure 4.4. (a) hydrogenized donor unit; (b-e) hydrogenized acceptor units for PBTCT, PBTCTO, PBTPDO, and PBTFDO from left to right; (f) donor-donor oligomer (g) acceptor-acceptor oligomer based on (e). (yellow) C, (white) H, (blue) S, (red) O, (purple) F.

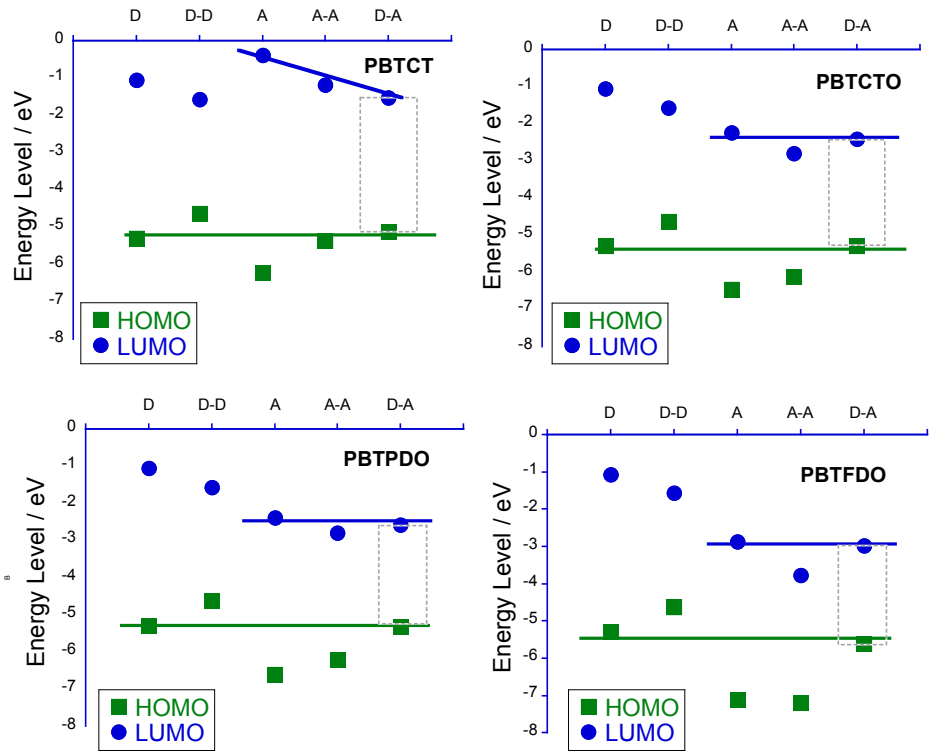

Figure 4.5. The frontier orbital energy levels of donor unit (D), donor-donor unit (D-D), acceptor unit (A), acceptor-acceptor unit (A-A) and CP monomer (D-A). It is found that the HOMO level is determined by that of the donor unit and the LUMO level by that of the acceptor unit in a single D-A repeat unit. The rule applies for all but PBTCT.

Bonding donor and acceptor groups to each other causes some amount of charge to transfer between the two, as illustrated in Figure 4.6. The strength of electron donating or withdrawing behavior can be measured by the excess of charge compared to the isolated units.[18] For PBTCT the electron donating strength of the donor unit is only slightly larger than that of the acceptor unit. In such CP, neither the donor nor the acceptor put a definite mark onto the CP's electron donating or withdrawing characteristics. Compared to the other three D-A monomers, the energy levels of PBTCT from those of its donor or acceptor constituents, is fraught with an uncertainty of the order of 20-30% of the

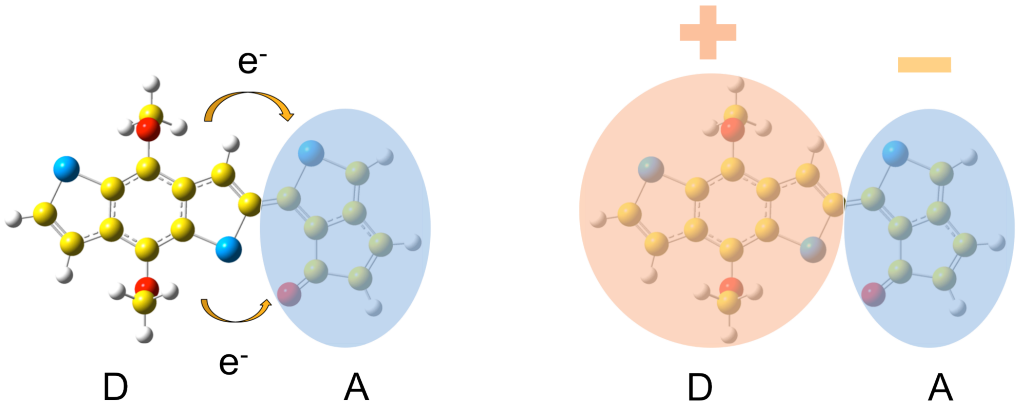

Figure 4.6. An illustration of intramolecular charge transfer for PBTCTO monomer. The charge distribution of donor (acceptor) units in CPs is different from that of corresponding isolated donor (acceptor) unit in Figure 4.4. The charge redistribution, as a result, can be expressed as the amount of charge transfer from donor unit to neighboring acceptor unit, or vice versa.

HOMO-LUMO gap. In fact, the use of weak donor and acceptor units was not satisfactory in yielding a low band gap material.[19] Moreover, the D-D oligomer and A-A oligomer both show a decreased energy gap compared to the single donor unit and acceptor unit, respectively, but neither of them can be predicted by the single unit. This result indicates that the energy levels of D-A monomer can be well predicted from that of the donor unit and acceptor unit, on the condition that the two units have a sufficiently large difference in the electron donating/withdrawing strength.

Despite the success of predicting the HOMO and LUMO levels of isolated D-A groups from the characteristics of the constituting units, this does not yet provide satisfactory agreement with experimental observations. Especially, the observation that the LUMO decreases more dramatically than the HOMO eludes explanation. Evidently, the difference is that in experimental systems CPs consists of a large number of repeat units, and the extended conjugation of orbitals is a hallmark of these polymers. To elucidate

the effect of conjugation length on electronic properties, we gradually increase the number of repeat units for our calculations, from 1 to 2, 3, and 4. With this, in fact, we reach the limit of reasonable computational expense. However, by constructing a simulation cell that is periodic in the direction of the polymer backbone we can mimic the case of a CP with continuous conjugation, or a quasi-infinite number of repeat units. While periodic boundary conditions do not allow for exploring the extent of conjugation lengths applicable to real CPs, it eliminates symmetry breaking end groups and thus provide for a better representation of a central segment of the polymer. The periodic unit cell in this case also contains two repeat units. Figure 4.7 shows the HOMO and LUMO levels calculated for these CP oligomer configurations. We also include the energy levels of experimentally synthesized CPs as measured by means of cyclic voltammetry (CV).[9] The calculation demonstrates that the HOMO levels of all CPs decrease minimally upon combining different numbers of repeating units, while the LUMO levels decrease more substantially. Moreover, the more pronounced electron withdrawing behavior of the acceptor unit, the more pronounced the decrease in the LUMO level. This ultimately leads to a narrowing of the energy gap in the sequence from PBTCT to PBTFDO, as we can see from the graphs in Figure 4.7(b) as well as Table 4.1, a trend that also agrees well with the experimental findings. We furthermore find that the LUMO of periodic unit cells in our calculation are always higher than the measured LUMO of polymers in experiments. Note that the polymer in experiments is restricted by effective conjugation length while the periodic unit cell in our calculations is an effectively infinite chain. This is contrary to our expectations, as a larger conjugation length should yield a more decreased LUMO. In fact, Zhang and Musgrave[20] found that although the hybrid DFT

functionals predict the HOMO–LUMO gap relatively accurately, the predicted the HOMO and LUMO energies are inaccurate. We observe a similar behavior in our calculations.

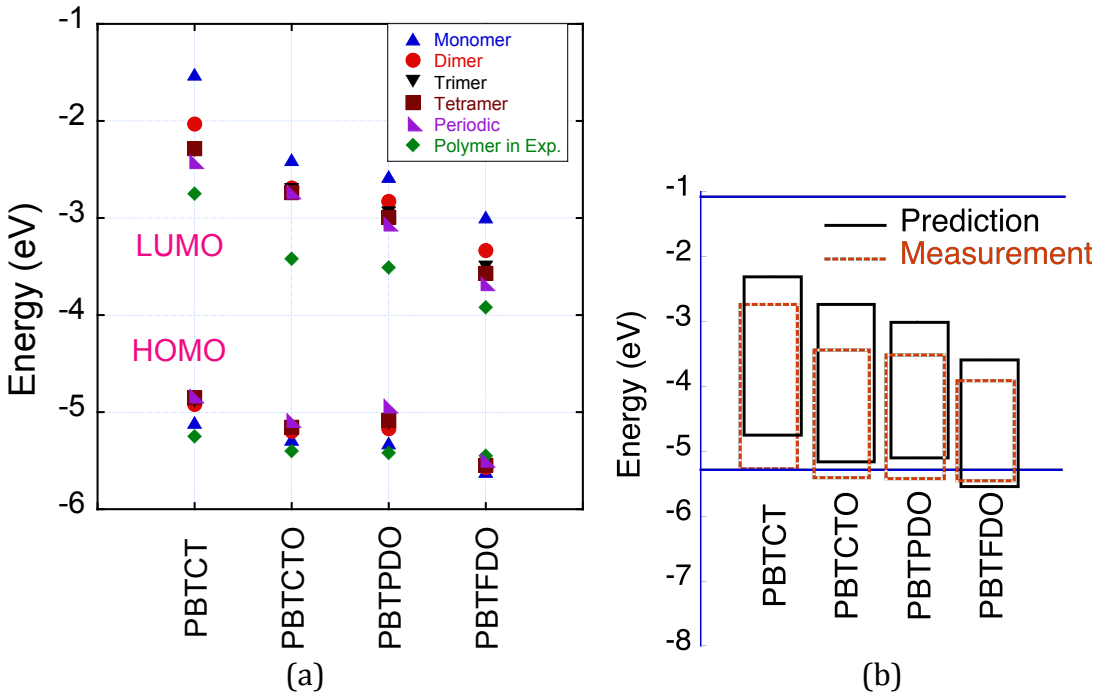

Figure 4.7. (a) Experimental and calculated energy levels, and (b) energy gaps for the CPs. The calculated energy gaps are based on the energy levels of periodic unit cells.

In order to elucidate this trend, the frontier orbitals for the various CPs are shown in Figure 4.8. For CP tetramers, the HOMO orbitals are generally less localized than the LUMO orbitals, but no clear trend is apparent for the variation in the HOMO-LUMO gap. Also, a strong size effect appears where the LUMO orbital is restricted on the right part of the PBTCT tetramer. After eliminating the size effect by applying periodic boundary conditions to create CP periodic unit cells, we found that HOMO orbitals remain uniformly delocalized while LUMO orbitals increasingly localize on acceptor units as the elements in this moiety become more electronegative. Taking PBTCT and

PBTFDO as the extreme examples, while a fair amount of LUMO density of PBTCT polymer can still be found within the thiophene part of the donor units, the LUMO density of PBTFDO polymer is completely concentrated on the acceptor units. A similar trend has been observed for other D-A polymers: as the degree of polymerization (or

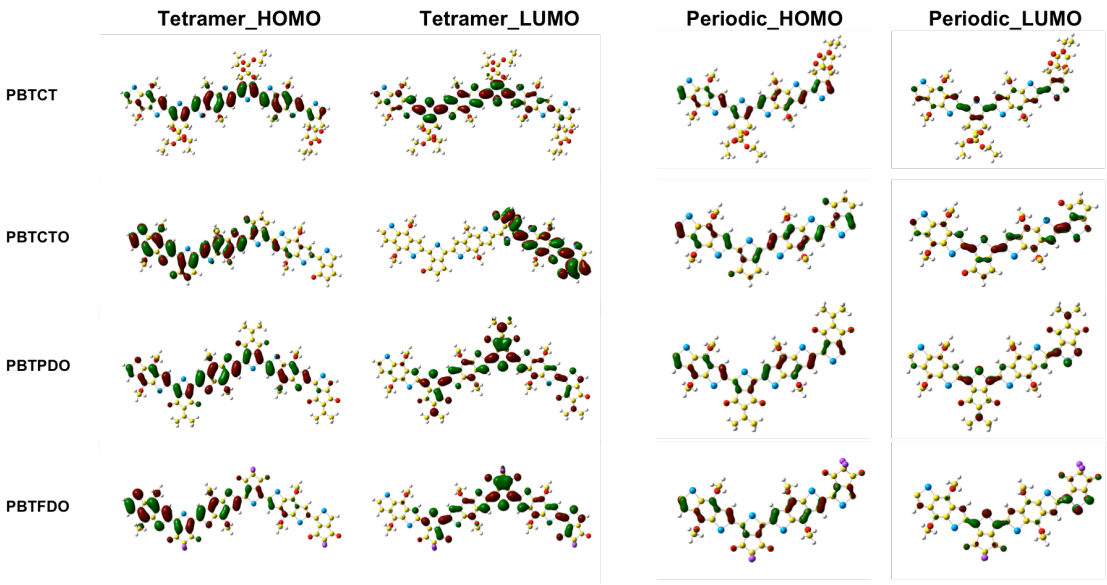

Figure 4.8. The frontier orbitals for CP tetramers and periodic unit cells (a unit cell consists of two D-A repeating units).

chain length) increases, the LUMO level decreases more rapidly than the HOMO level due to molecular orbital hybridization of each donor and acceptor unit, producing a narrowed energy gap.[12] This finding indicates that the LUMO localization plays an important role in controlling the energy gap for our CPs, in that the LUMO energy level is lowered when the LUMO is more localized. For our CPs, the donor unit essentially determines the HOMO levels.

As already alluded to earlier, the amount of intramolecular charge transfer between donor and acceptor appears to be a principal indicator for the extent to which of HOMO-

LUMO gap is reduced in CPs.[21] Particularly for our CPs, which all have the same donor in common, it is straightforward to evaluate the relative electron withdrawing strengths for the different acceptor units by simply comparing the charge differences between donor and acceptor. Mulliken charge analysis is performed to obtain the amount of intramolecular charge transfer upon combining the donor and acceptor units. Note that we only compare the sum of the non-hydrogenized part of the donor unit, as the π-

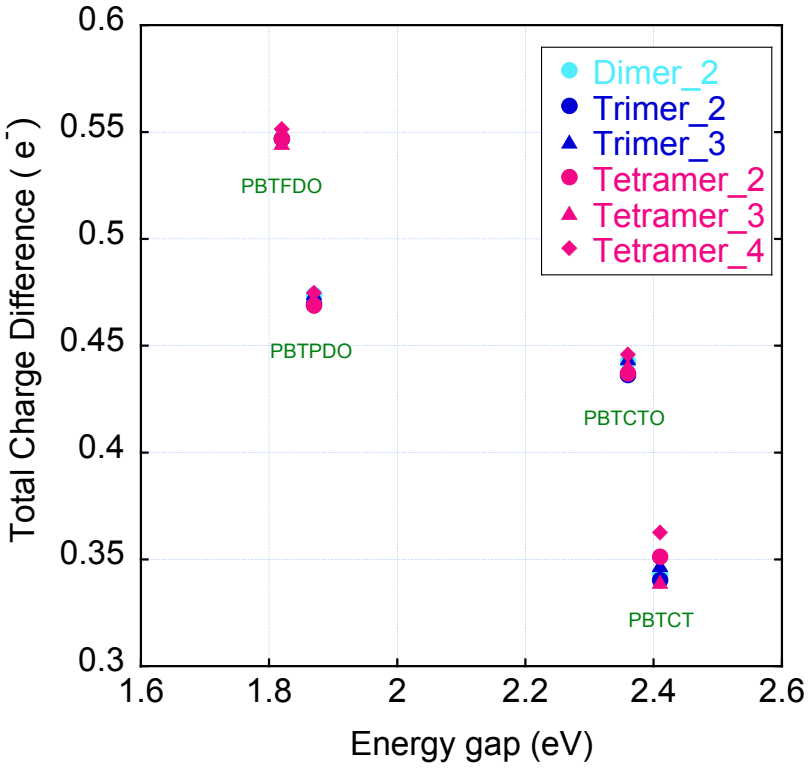

Figure 4.9. The total charge difference of the donor unit in the CPs as a function of energy gap. To eliminate any size effects, only the donor units in the middle of the molecules are considered, e.g. the second donor unit in the dimer is named as Dimer_2 and the third donor unit in the tetramer is named as Tetramer_3.

electrons on the conjugation backbone are dominant in the intramolecular charge transfer.[22] Figure 4.9 shows the total charge difference of the donor units as a result of the intramolecular charge transfer. A positive value indicates a departure of electrons.

The CP monomer is omitted because we only consider donor units that are in the middle of an oligomer to minimize any size effects. As expected, intramolecular charge transfer increases as the strength of electron withdrawing by the acceptor unit becomes more pronounced. Furthermore, a rough proportionality (with a correlation coefficient of R^2 = 0.78) between the amount of charge transfer and the decrease in energy gap is observed. We also notice that the amount of intramolecular charge transfer in PBTCT is more strongly dependent on the position of the donor unit in the oligomer, as reflected by the relatively large variation in the total charge increase in the donor units at different positions, particularly in the tetramer of this compound. In the stronger D-A oligomers, e.g. PBTCTO, PBTPDO and PBTFDO, the amount of intramolecular charge transfer is quite comparable irrespective of the donor-acceptor pair position along the extent of the oligomer. Interestingly, the less variation there is in the charge transfer as a function of the position in the oligomer, the stronger the localization of the LUMO orbitals on acceptor. Hence, we observe that the electron withdrawing strength of the acceptor and the degree of charge localization correlate with extent to which the LUMO level is lowered in these CPs.

4.3.2. Varying the donor in conjugated oligomers or polymer for a given acceptor

To further substantiate the trends observed with the variation of acceptor molecules, we investigated whether similar governing principles apply when altering the chemistry of the donor groups. To this end we conceived a series of systematic functionalizations and elemental substitutions within the donor unit of PBTFDO, creating molecular designs that presumably allow us to control the HOMO level while pinning the LUMO level. A further consideration, as before, was to maintain planar polymer conformations. After

exploring several chemistries, the best design strategy turned out to be elemental substitution in the PBTFDO compound. While maintaining its acceptor, we replace one or two of the sulfur atoms in the donor unit with Se or O to obtain a new donor unit,

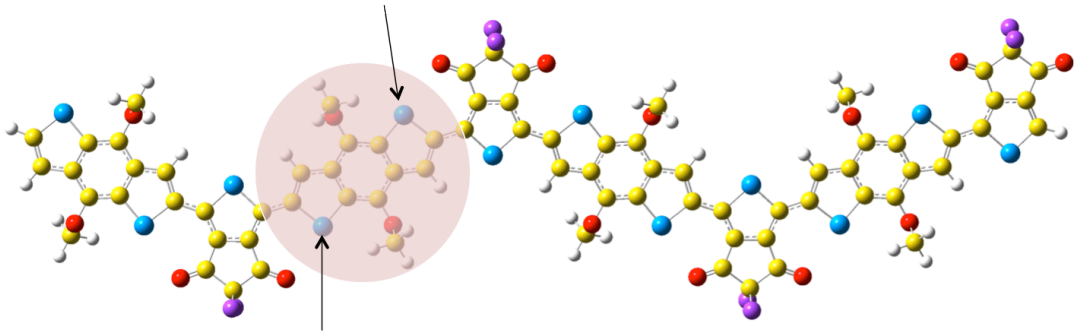

Figure 4.10. The structure of PBTFDO. While maintaining the acceptor unit of PBTFDO, one or two sulfur atoms in the donor unit is replaced by Se or O to obtain a new donor unit, corresponding to four newly designed CPs named as PBTFDO(Se), PBTFDO(2Se), PBTFDO(O), PBTFDO(2O) .

labeled as PBTFDO(Se), PBTFDO(2Se), PBTFDO(O), PBTFDO(2O), as is shown in Figure 4.10. The guiding principle was to changing the acceptor's electron withdrawing strength by introducing elements with different electronegativities. As reported, the energy gap of a furan-based CP is smaller than that of a thiophene-based CP with a similar structure.[23,24] This behavior is mainly caused by two factors: First, in comparison with thiophene, the five-membered ring of furan shows weaker steric hindrance to adjacent units, because of a smaller diameter of the oxygen atom. Therefore a planar structure and a well conjugated backbone is formed.[25] Second, the delocalization is not as extensive in furan because of high electronegativity of oxygen, so that the lone pair is held more tightly by the oxygen. Therefore, aromatic stabilization is weak in furan, which makes it more active in terms of electron donating.[26] Hence, we would expect to lower the energy gap for oxygen substitution, and raise it for selenium substitution.

All of the newly designed CPs have a similar zig-zag conformation as PBTFDO. The twist angles between the D-A repeating units are 1.6°, 1.1°, 16.1°, 12.5° for PBTFDO(2Se), PBTFDO(Se), PBTFDO(O), PBTFDO(2O), respectively. Compared to PBTFDO, selenium substitution does not affect the planarity of the conjugation backbone, while oxygen substitution compromises this planarity. Contrary to our expectations, the atomic sizes have no significant effect on the degree of conjugation along the oligomer backbone. In fact, the repulsive forces between the lone pair of the heteroatom (i.e., Se, S, O) in the donor unit and the lone pair of the ketone in the neighboring acceptor unit dominate the conformation of the conjugation backbone. The lone pair electrons are held more tightly by oxygen compared to sulfur or selenium,

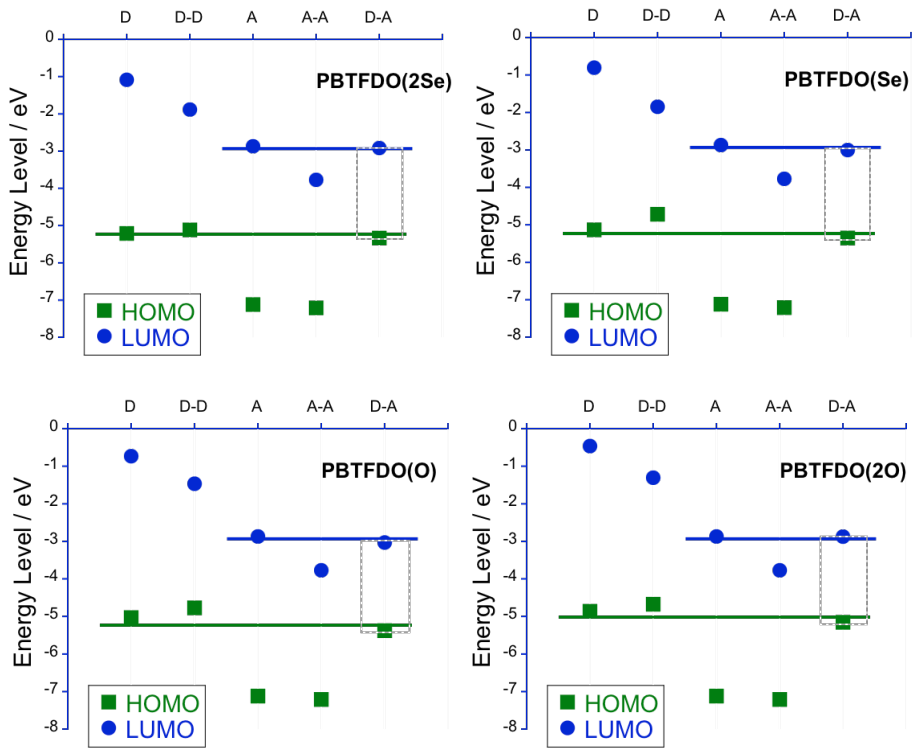

Figure 4.11. The frontier orbital energy levels of donor unit (D), donor-donor unit (D-D), acceptor unit (A), acceptor-acceptor unit (A-A) and CP monomer (D-A) for the newly designed CPs.

because the delocalization is not as extensive in furan as in thiophene or selenophene. Therefore, when the heteroatom in the donor unit is oxygen, the repulsive forces between the lone pair of this heteroatom and the lone pair of the ketone in the neighboring acceptor unit are maximized. Consequently, the D-A repeat units in PBTFDO(O) and PBTFDO(2O) form large twist angles.

Figure 4.11 shows the relationship of frontier orbital energy levels between the CP donor acceptor repeat unit (monomer), the isolated donor and acceptor units, and hypothetical donor-donor, and acceptor-acceptor pairs. The results obtained are consistent with our previous findings, in that the HOMO and LUMO of a monomer is determined by the HOMO of the isolated donor unit and the LUMO of the isolated acceptor unit, respectively. Furthermore, the frontier orbital energy levels of the CP oligomers with different lengths and periodic unit cells are shown in Figure 4.12. As we can see, by increasing the number of repeat units from one to four, for a given donor-acceptor pairing the LUMO decreases more prominently than HOMO, which represents the same trend as for the four CPs discussed above. On the

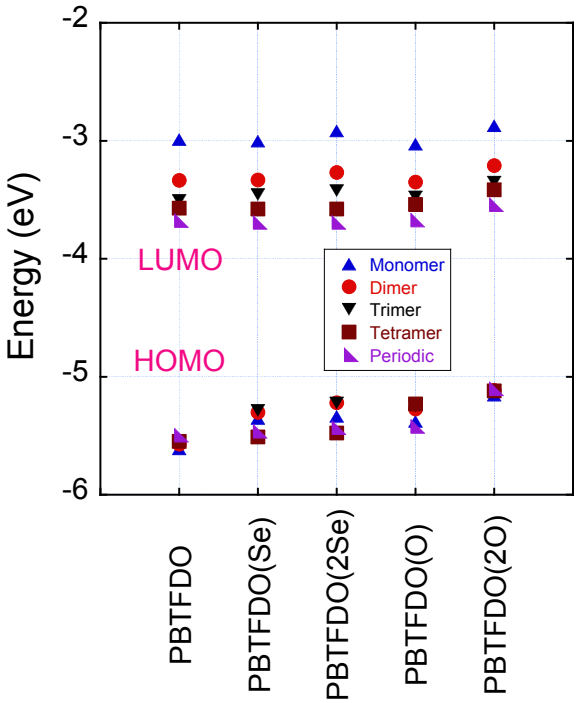

Figure 4.12. Calculated energy levels for the newly designed CPs. PBTFDO is also included for comparison.

other hand, when the donor unit is varied, the LUMO stays approximately constant, and more so for the longer configurations, whereas the HOMO increases in the sequence PBTFDO, PBTFDO(Se), PBTFDO(2Se), PBTFDO(O), PBTFDO(2O). Similarly, the calculated energy gaps these CPs follow essentially the same trend, except that PBTFDO(2Se) and PBTFDO(O) trade places and their energy gaps differ only minutely.

By examining the frontier orbitals of the newly designed CP periodic unit cells, as shown in Figure 4.13, we find that the LUMO orbitals are localized on the acceptor units to about the same degree for all the CPs. The HOMO orbitals withdraw increasingly from the acceptor unit and become more localized on the donors, as the sulfur is

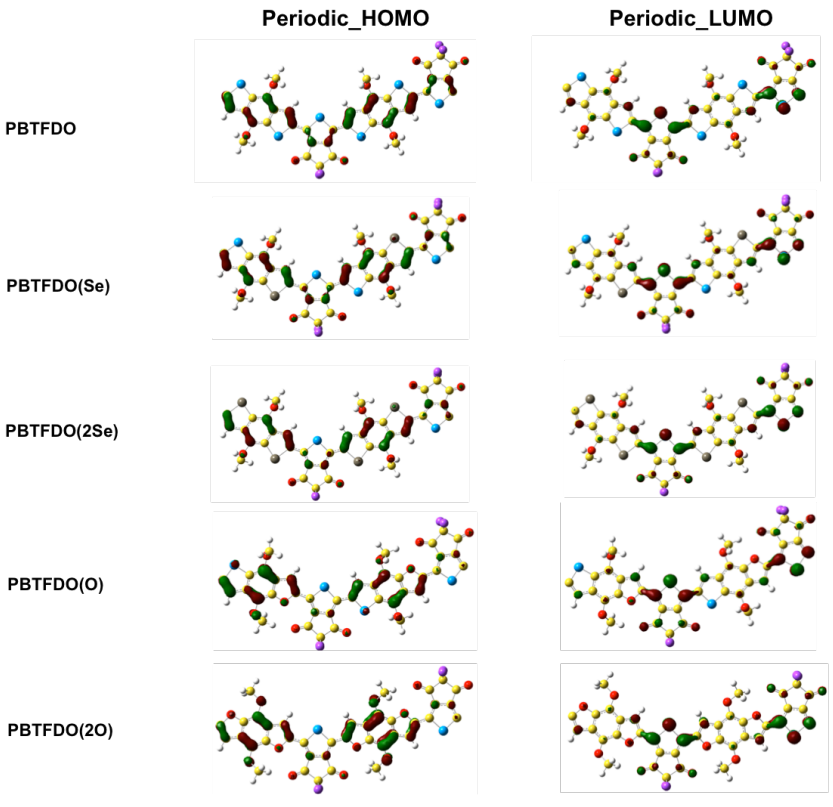

Figure 4.13. The frontier orbitals for the newly designed CP periodic unit cells (a unit cell consists of two D-A repeating units).

substituted with one Se, two Se, one O, and finally two O, i.e., the same sequence as that of the HOMO-LUMO gap decrease. This strongly supports our previous finding that the frontier orbital localization strongly correlates with the energy gap decrease for D-A type CPs,

Lastly, the amount of intramolecular charge transfer is calculated as the negative of the total charge difference associated with the acceptor unit, which common to all of our newly designed CPs. The negative value is necessary to be consistent with the charge increase on the donor, calculated earlier. In Figure 4.14, we plot the total charge difference for all the CPs, taking the average for all the donor-acceptor positions in the dimers, trimers and tetramers. As we can see, the larger the amount of intramolecular

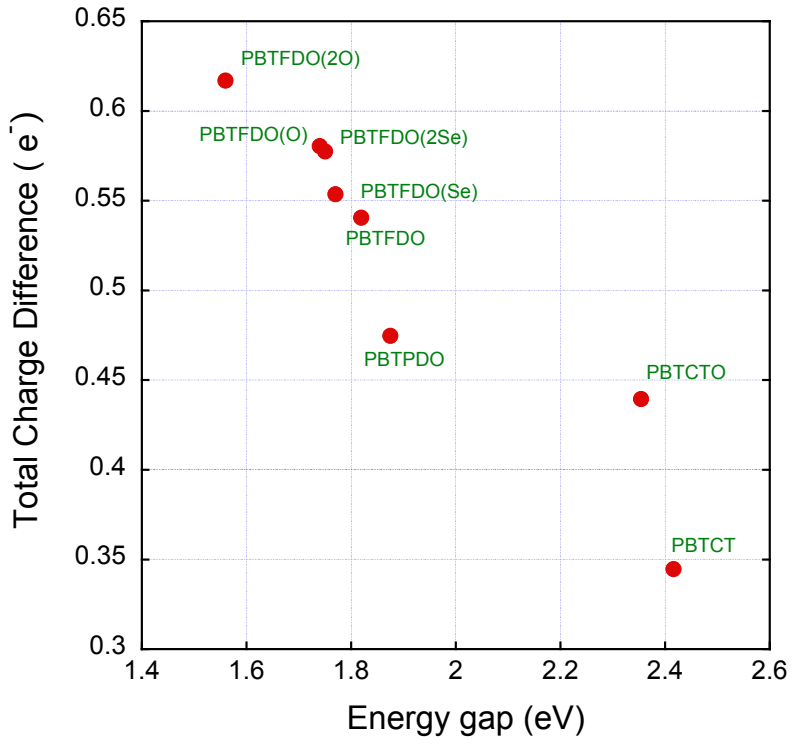

Figure 4.14. The total charge difference as a function of energy gap for all the CPs.

charge transfer, the smaller the energy gap, regardless of whether the donating strength of the donor or the withdrawing strength of the acceptor is manipulates. Moreover, the linear relationship is preserved when adding the newly designed CPs, with an improved correlation coefficient of 0.89. Interestingly, however, the electronegativity values for selenium, sulfur, and oxygen are 2.55, 2.58, and 3.44 respectively.[27] Yet, the electron donating strength of the molecular units these elements reside on behaves inversely proportional to what would be expected by the tendency of these elements to attract electrons. This leads us to conclude that the electron donating strength of molecular complexes depend in more complex ways on the electronegativity of specific constituents.

4.4. Conclusion

We studied the mechanism of energy level tuning in D-A conjugated polymers via first principle DFT calculations. We first investigated a series of synthesized CPs that are composed of a constant donor unit but different acceptor units. We observed that the HOMO of a monomer is determined by the HOMO of the isolated donor unit, and the LUMO of it is determined by the LUMO of the isolated acceptor unit. The introduction of stronger acceptor unit lowers the LUMO level, but leaves the HOMO level almost unchanged. This trend is in good agreement with the previous experimental results. This trend is strongly correlated with the extent of orbital localization, as the HOMO orbital is ubiquitously delocalized but LUMO orbital becomes more localized when using a stronger acceptor unit. Furthermore, we presented a linear relationship between the energy gap of a CP polymer and the amount of intramolecular charge transfer. We then designed another series of CPs, which have a constant acceptor unit but different donor

units. Similarly, the HOMO and LUMO of a monomer is determined by the HOMO of the isolated donor unit and the LUMO of the isolated acceptor unit, respectively. We observed that the introduction of stronger donor unit increases the HOMO level but keeping the LUMO level almost unchanged. The frontier orbital analysis showed that the LUMO orbital is ubiquitously localized but HOMO orbital becomes more localized when using a stronger donor unit. Also, the amount of intramolecular charge transfer for the synthesized CPs and the newly designed CPs shows a good linearity as a function of energy gap. Overall, the simulation results shine light on the computational prediction of tuning energy levels and energy gap for D-A conjugated polymers at molecular level.

Table 4.1 Energy gaps for the CPs (experimental measurement in parenthesis).

	energy gap (eV)
PBTCT	2.41 (2.50)
PBTCTO	2.36 (1.98)
PBTPDO	1.87 (1.91)
PBTFDO	1.82 (1.53)

Table 4.2 Energy gaps for the newly designed CPs. PBTFDO is also included for comparison. The calculated energy gap is based on the energy levels of periodic unit cells

	energy gap (eV)
PBTFDO	1.82
PBTFDO (Se)	1.77
PBTFDO (2Se)	1.74
PBTFDO (O)	1.75
PBTFDO (2O)	1.56

4.5. References

1. Zhang, Y. et al. Indacenodithiophene and Quinoxaline-Based Conjugated Polymers for Highly Efficient Polymer Solar Cells. *Chem. Mat.* **23**, 2289-2291 (2011).
2. Guenes, S., Neugebauer, H. & Sariciftci, N. S. Conjugated polymer-based organic solar cells. *Chem. Rev.* **107**, 1324-1338 (2007).
3. Huo, L., Chen, H.-Y., Hou, J., Chen, T. L. & Yang, Y. Low band gap dithieno[3,2-b:2 ‘,3 ‘-d]silole-containing polymers, synthesis, characterization and photovoltaic application. *Chem. Commun.* 5570-5572 (2009).
4. Gierschner, J., Cornil, J. & Egelhaaf, H.-J. Optical bandgaps of pi-conjugated organic materials at the polymer limit: Experiment and theory. *Adv. Mater.* **19**, 173-191 (2007).
5. van Mullekom, H. A. M., Vekemans, J. A. J. M., Havinga, E. E. & Meijer, E. W. Developments in the chemistry and band gap engineering of donor-acceptor substituted conjugated polymers. *Mater. Sci. Eng. R-Rep.* **32**, 1-40 (2001).
6. Zotti, G. et al. Polyconjugated polymers from anodic coupling of dipyrrolyl-ethylenes, -arylenes, and -heteroarylenes. Narrow potential windows of conductivity by alternation of electron-rich and electron-poor units. *Chem Mater* **9**, 2876-2886 (1997).
7. Ajayaghosh, A. Donor-acceptor type low band gap polymers: polysquaraines and related systems. *Chem Soc Rev* **32**, 181-191 (2003).
8. Colladet, K. et al. Low band gap donor-acceptor conjugated polymers toward organic solar cells applications. *Macromolecules* **40**, 65-72 (2007).
9. Kim, B.-G. et al. Energy Level Modulation of HOMO, LUMO, and Band-Gap in Conjugated Polymers for Organic Photovoltaic Applications. *Adv. Funct. Mater.* **23**, 439-445 (2013).
10. Frisch, M. J. et al. Gaussian 09. (2009).
11. Mulliken, R. S. Criteria for the Construction of Good Self‐Consistent‐Field Molecular Orbital Wave Functions, and the Significance of LCAO‐MO Population Analysis. *The Journal of Chemical Physics* **36**, 3428-3439 (1962).
12. Risko, C., McGehee, M. D. & Bredas, J.-L. A quantum-chemical perspective into low optical-gap polymers for highly-efficient organic solar cells. *Chem. Sci.* **2**, 1200-1218 (2011).
13. Oezen, A. S., Atilgan, C. & Sonmez, G. Noncovalent intramolecular interactions in the monomers and oligomers of the acceptor and donor type of low band gap conducting polymers. *J. Phys. Chem. C* **111**, 16362-16371 (2007).
14. Ko, S. et al. Tuning the Optoelectronic Properties of Vinylene-Linked Donor-Acceptor Copolymers for Organic Photovoltaics. *Macromolecules* **43**, 6685-6698 (2010).
15. Meier, H., Stalmach, U. & Kolshorn, H. Effective conjugation length and UV/vis spectra of oligomers. *Acta Polym.* **48**, 379-384 (1997).
16. Leclerc, M. Optical and electrochemical transducers based on functionalized conjugated polymers. *Adv. Mater.* **11**, 1491-149+ (1999).
17. Huser, T., Yan, M. & Rothberg, L. J. Single chain spectroscopy of conformational

dependence of conjugated polymer photophysics. *Proc. Natl. Acad. Sci. U. S. A.* **97**, 11187-11191 (2000).
18. Hung, Y.-C., Jiang, J.-C., Chao, C.-Y., Su, W.-F. & Lin, S.-T. Theoretical Study on the Correlation between Band Gap, Bandwidth, and Oscillator Strength in Fluorene-Based Donor-Acceptor Conjugated Copolymers. *J. Phys. Chem. B* **113**, 8268-8277 (2009).
19. ZHOU, Z. H. et al. UNIQUE OPTICAL AND ELECTROCHEMICAL PROPERTIES OF PI-CONJUGATED ELECTRICALLY CONDUCTING COPOLYMERS CONSISTING OF ELECTRON-WITHDRAWING PYRIDINE UNITS AND ELECTRON-DONATING THIOPHENE UNITS. *J. Chem. Soc.-Chem. Commun.* 1210-1212 (1991).
20. Zhang, G. & Musgrave, C. B. Comparison of DFT methods for molecular orbital eigenvalue calculations. *J. Phys. Chem. A* **111**, 1554-1561 (2007).
21. Deng, L. et al. Molecular designing and DFT investigation of novel alternating donor-acceptor dibenzo[b,d]thiophen-based systems: from monomer to polymer. *Struct. Chem.* **23**, 97-106 (2012).
22. Schwartz, B. J. Conjugated polymers as molecular materials : How chain conformation and film morphology influence energy transfer and interchain interactions. *Annu. Rev. Phys. Chem.* **54**, 141-172 (2003).
23. Huo, L. et al. Conjugated and Nonconjugated Substitution Effect on Photovoltaic Properties of Benzodifuran-Based Photovoltaic Polymers. *Macromolecules* **45**, 6923-6929 (2012).
24. Huo, L. et al. Synthesis of a 4,8-dialkoxy-benzo[1,2-b:4,5-b ']difuran unit and its application in photovoltaic polymer. *Chem. Commun.* **48**, 3318-3320 (2012).
25. Bunz, U. H. F. alpha-Oligofurans: Molecules without a Twist. *Angew. Chem.-Int. Edit.* **49**, 5037-5040 (2010).
26. Acheson, R. M. introduction to the chemistry of heterocyclic compounds. (1967).
27. Patra, A., Wijsboom, Y. H., Leitus, G. & Bendikov, M. Synthesis, Structure, and Electropolymerization of 3,4-Dimethoxytellurophene: Comparison with Selenium Analogue. *Org. Lett.* **11**, 1487-1490 (2009).

Chapter 5. The effects of extended conjugation length of purely organic phosphors on their phosphorescence emission properties

5.1. Introduction

Organometallic phosphorescence has attracted much interest for application as organic light emitting diodes, because it offers theoretically 4 times better efficiency than fluorescence counterparts.[1-4] However, it is challenging to identify new metallic elements and strict ligand design for color tuning in organometallic phosphors. Also, organometallic phosphors for higher energy emission in the blue and near UV regions have poor stability, which results in limited lifetime.[5,6] Purely organic phosphors offer an attractive alternative in terms of synthesis flexibility, good stability, and relatively easy color tuning by controlling the optical electron energy gap and electron density. However, they are rarely reported because spin-orbit coupling is not efficiently activated in the absence of a heavy atom, such as a transition metal, which promotes spin-flipping and phosphorescence emission against dominant vibrational losses.[7,8]

To achieve bright purely organic phosphorescent materials, there are two critical requirements: (i) promoting intersystem crossing (ISC) from excited singlet states to triplet states and (ii) radiative decay via a second ISC event from the triplet states to ground states. Aromatic ketones exhibit efficient spin-orbit coupling at the carbonyl oxygen due to energy proximity between S_1 and T_2.[9] Therefore aromatic ketones are unique moieties in designing organic phosphorescent materials. Even though triplets are

generated from aromatic ketones through ISC, they inevitably experience non-radiative decay during the second ISC. More specifically, enhancing spin-orbit coupling is the most important and challenging aspect of creating purely organic phosphorescent materials.

Organic phosphorescence is mostly observed under cryogenic conditions or for well-confined inorganic crystals, where vibrational pathways are minimized.[10-13] Kabe et al. have shown enhanced phosphorescence in dibenzophosphole chalcogenide mixed crystals at low temperature.[14] Room temperature phosphorescence (RTP) from crystals was detected in slowly grown halogenated benzophenone crystals and Boc and N,N′-dicyclohexylurea capped γ-amino acid crystals grown in a common organic solvent.[15,16] Bolton *et al*. designed well-defined phosphorescent crystals by incorporating a directed intermolecular halogen bonding reaching up to 55% efficient quantum yield in an ambient condition at room temperature.[17] However, these materials are still impractical because the required crystallinity can only be achieved and preserved under limited conditions. Accordingly, achieving phosphorescence in amorphous structures would be desirable, especially in view of practical applications such as OLED, solid-sate lighting, and bio imaging. Even though RTP has been observed in amorphous materials in which strong hydrogen bonding is incorporated between phosphors and matrix polymers, the absolute quantum yield was very low (~ 1%) or not even reported.[18-20] More efficient amorphous RTP was reported by Lee et al. by embedding a bromobenzaldehyde derivative in a glassy poly(methyl methacrylate) (PMMA) matrix.[21] They demonstrated that the degree of β-relaxation of PMMA, which depends on the tacticity, strongly affects phosphorescence efficiency of the embedded organic phosphors. The ensuing

temperature dependence of this property provides the basis for an optical temperature sensor integrated into microfluidic devices. Recently, more efficient RTP with 24% of quantum yield was achieved by introducing rationally designed hydrogen bonding and halogen bonding with amorphous polymer matrix.[22] Hirata *et al*. showed that, by acting as an oxygen barrier and by providing mechanical rigidity, β-estradiol as a host material minimizes the nonradiative decay pathways of highly deuterated fluorene derivatives.[23] They realized persistent RTP with a long lifetime (> 1 s) and high quantum yield (> 10%) at ambient conditions. However, thus far, all efforts have been focused on reducing vibrational decay pathways by imparting interactions between an organic phosphor and an amorphous host material. Going forward, we should optimize the design principle for molecular structures of organic phosphors to achieve RTP in a more practical and controllable condition, e.g. solution state. Compared to the complex systems discussed above, phosphorescence in a simple system is of more practical use.

In organometallic phosphorescence, a few studies were carried out to elucidate the structure-property relationship, mainly for platinum containing phenyl-ethynyl oligomers.[24,25] For example, Rogers *et al*. investigated the effects of increased conjugation and the influence of the platinum atom on the electronic structure by varying ligand length. However, there is no systematic study about the effect of extended conjugation in purely organic phosphors. In this contribution, we focus on the first ISC event, triplet harvesting, which is one of the key processes in order to realize bright phosphorescence emission. To investigate the effect of the conjugation length on phosphorescence, we explored a series of organic phosphors with varied conjugation lengths using computational techniques. By comparing our calculation results to a parallel experimental

investigation carried out by close collaborators at this university, we are able to obtain a better understanding for the ISC mechanism in phosphorescence emission.

5.2. Experimental background

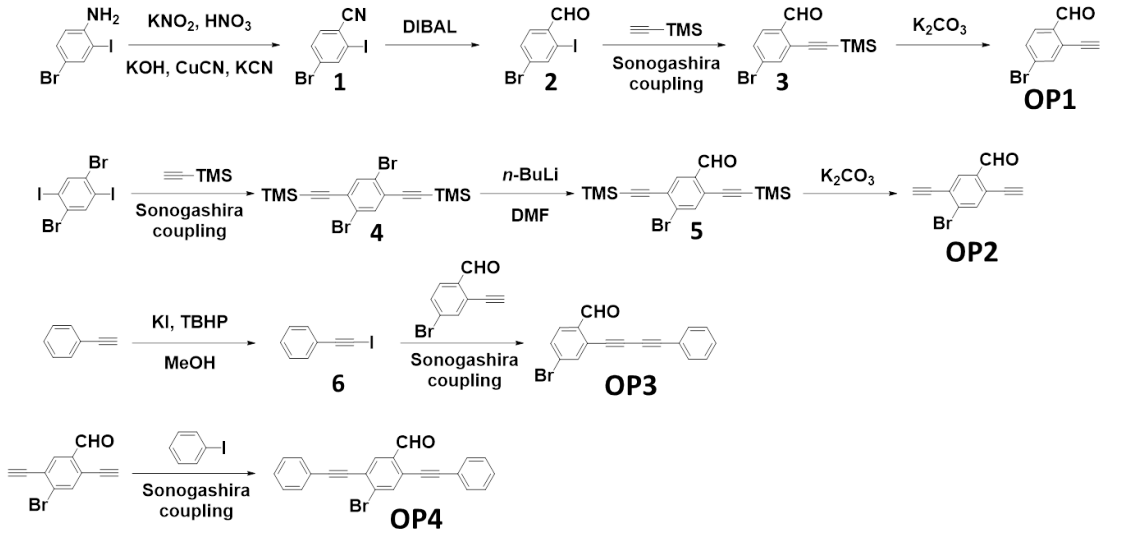

Figure 5.1. Synthetic routes for purely organic phosphors.

Figure 5.1 shows the investigated phosphors with increased conjugation lengths from OP1 to OP4. Experimental UV absorption spectra are depicted together with extinction coefficients in Figure 5.2(a). As the conjugation length increases, the absorption wavelength red-shifts from 310 nm for OP1 to 360 nm for OP4 and the extinction coefficient increases in the S_0-S_1 transition region. Figure 5.2(b) shows steady-state phosphorescence spectra collected at 77 K and ambient pressure. Each solution was diluted to around 10^{-5} M with chloroform and excited at its respective maximum excitation wavelength. The emission intensity was calibrated so as to clearly show the change in phosphorescence intensity for different molecules at the same absorbance. The fluorescence emission spectra due to the S_1-S_0 transition were cut off to clearly see phosphorescence emission. As the conjugation length increases, emission is red-shifted

from OP1 to OP4. More importantly, the phosphorescence intensity dramatically decreases with increasing conjugation length. We conclude that triplet generation via the first ISC is somehow diminished with increasing conjugation length because vibrational decay pathways have been effectively turned off at the liquid nitrogen temperature of 77 K and thereby the second ISC from T_1 to S_0 should be efficient. The purpose of the computational investigation is to elucidate why this is the case, and based on this understanding develop molecular design criteria for materials with targeted properties.

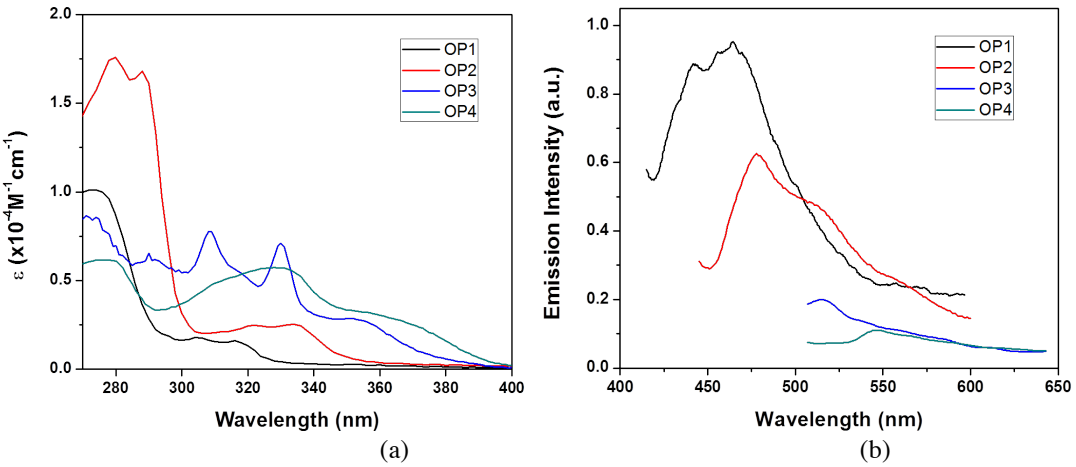

(a) (b)

Figure 5.2. (a) UV absorption spectra were measured in chloroform solution (diluted to 10^{-5} M) at room temperature and plotted with extinction coefficient. (b) Phosphorescence spectra were measured at 77 K with same absorbance. Each molecule was excited at 320, 336, 350, and 360 nm respectively.

5.3. Computational methodology

5.3.1. Spin selection rule

We first present a short illustration of spin selection rule, by which only spin-allowed transitions exist. To simplify, we consider a two-electron system with a total spin *S* equal to either 0 or 1, corresponding to two spins being anti-parallel or parallel, respectively.

The spin degeneracy is given as $2S+1$. For $S=0$, the spin wavefunction is anti-symmetric and expressed as

$$\Psi = \frac{1}{\sqrt{2}}\left[\alpha_1\beta_2 - \beta_1\alpha_2\right] \tag{5.1}$$

where α and β represents the possible spin states of either electron denoted by subscripts. For $S=1$, three possible spin wavefunctions exist, and are all symmetric,

$$\Psi = \alpha_1\alpha_2 \tag{5.2}$$

$$\Psi = \frac{1}{\sqrt{2}}\left[\alpha_1\beta_2 + \beta_1\alpha_2\right] \tag{5.3}$$

$$\Psi = \beta_1\beta_2 \tag{5.4}$$

As we can see, the symmetric and anti-symmetric wavefunction, Ψ_+ and Ψ_-, will satisfy

$$\Psi_{+12} = \Psi_{+21} \tag{5.5}$$

$$\Psi_{-12} = -\Psi_{-21} \tag{5.6}$$

The probability of an electronic transition is related to the dipole moment $\vec{\mu}$ of the system. For transitions between two states of different symmetries, we obtain the following equations,

$$P_{12} = \left\langle \Psi_{+12} \left| \vec{\mu} \right| \Psi_{-12} \right\rangle \tag{5.7}$$

$$P_{21} = \left\langle \Psi_{+21} \left| \vec{\mu} \right| \Psi_{-21} \right\rangle \tag{5.8}$$

where P_{12} denotes the probability of transition from the symmetric state to the anti-symmetry state for the system of electron 1 and 2; P_{21} denotes the probability of transition from the symmetric state to the anti-symmetric state for the system of electron 2 and 1. Since the transition probability cannot depend on the labeling of the electrons, we have

$$P_{12} = P_{21} \tag{5.9}$$

By using the relation 5.5 and 5.6, we will also find

$$P_{12} = -P_{21} \tag{5.10}$$

As a result, this makes the transition probability of different spin states equal to 0. To summarize, the spin component of the initial and final state must have similar symmetry, i.e. the spin-allowed transitions are singlet->singlet and triplet->triplet.

5.3.2. Intersystem crossing (ISC) rate

In phosphorescence, triplet states are populated by a non-radiative transition from a singlet to a triplet $S_k \rightarrow T_n$, i.e. the intersystem crossing. The underlying driving force is spin orbit coupling that overcomes the spin-forbidden barrier and facilitate the transitions between singlets and triplets. Several formalisms are given in the literature for estimating the ISC rate, k_{ISC}. The most simplified form is given as,[26]

$$k_{ISC} \propto \frac{\left\langle S_k \left| H_{SO} \right| T_n \right\rangle^2}{(\Delta E)^2} \tag{5.11}$$

where H_{SO} is the spin-orbit operator for calculating the coupling between k^{th} singlet S_k and n^{th} triplet T_n, and ΔE is the energy difference between the two excited states. It provides an estimate of the ISC rate for simple comparison. In order to perform a full ISC rate calculation, we will use the Fermi's golden rule expression for non-radiative transitions by considering Franck-Condon effect,[27]

$$k_{ISC} = \frac{2\pi}{\hbar}\langle S_k|H_{SO}|T_n\rangle^2[FCWD], \tag{5.12}$$

where *FCWD* is the Franck-Condon weighted density of states. There are two main computational methodologies for determining Franck-Condon factor, either by applying displaced-oscillator model[28] or by considering the Duschinsky rotation effect.[29] In this work, we use the displaced-oscillator model to calculate the intersystem crossing rate:

$$k_{ISC} = \frac{\langle S_k|H_{SO}|T_n\rangle^2}{\hbar^2}\int_{-\infty}^{\infty} dt \exp\left\{\frac{i\Delta Et}{\hbar} - \sum_j S_j[(2n_j+1) - n_j e^{-iw_j t} - (n_j+1)e^{iw_j t}]\right\} \tag{5.13}$$

where $n_j = 1/(\exp(\hbar w_j / k_B T) - 1)$ is the occupation number of j^{th} intramolecular phonon mode with frequency w_j, and S_j is the Huang-Rhys factor measuring the electron-vibration coupling strength (Table 5.1). Note that the displaced-oscillation model is widely used in transition rate calculation between two states, e.g. simulating charge transfer reactions. Nan *et al.*[30] and Wang *et al.*[31] have found good agreement between experiments and calculations of charge mobility in organic crystals, e.g. pentacene and rubrene, by including the displaced-oscillator model.

5.3.3. Computational detail

The excited energy levels, normal mode and electron density of the molecules were calculated using Gaussian09[32] and we visualized the results using GaussView 05 or Multiwfn.[33,34] All calculations were carried out using B3LYP exchange correlation function, and 6-311G* contracted Gaussian basis set with polarization functions. The molecular geometries for both ground and excited states were optimized in the Cartesian coordinate system without any symmetry constraints (maximum degrees of freedom). Following that, a dynamic analysis of the optimized structures was performed to confirm their stability by ascertaining the absence of imaginary frequency modes. Next, the excited energy levels were calculated using a single-point time-dependent density functional theory (TDDFT) calculation based on the ground state geometry. The Huang-Rhys factors corresponding to different normal mode frequencies were obtained using the DUSHIN program developed by Reimers.[35] Finally, The electron density distribution of the ground and excited states were generated based on the optimized structure in that state. The spin orbit coupling strength between two different excited states were calculated using the Dalton program.[36] The double residue of the quadratic response function was applied when the two states were both excited states, while the single residue of the linear response was applied when one of the two states was ground state.

5.4. Results and Discussion

5.4.1. Structural and electronic properties

For each phosphor molecule, the π-conjugated part of ground state structure optimized using DFT calculations adopts a planar configuration, which allows us to unequivocally

define and compare their conjugation lengths. The CHO functional group lies in the same plane as the conjugated backbone, with the C=O bond pointing away from the triple bond. This is due to the repulsive interaction between the lone pair of electrons on the oxygen atom and the π-electrons in the triple bonds. In the OP1 molecule, for example, when the C=O double bond and the C-C triple bond are close to each other, the local optimal state is raised by 108 meV above the ground state.

Next, we calculated the excited state energy levels of S_1, T_1 and T_2. Comparing the excited states energy levels obtained from TDDFT calculations with experimental measurements (Figure 5.3), we observe a good match for both S_1 and T_1 energy levels relative to the respective S_0 levels. We also note that the energy levels for S_1 and T_1 consistently, albeit slightly, decrease with increasing conjugation length, but for each state keep close to each other within a narrow range. From OP1 to OP4, S_1 only decreases by 0.53 eV in experiments and 0.26 eV in calculations, and T_1 by 0.42 eV in experiments and 0.66 eV in calculations. Hence, we can expect that the optoelectronic properties of these molecules are dominated by the interplay between their conjugation backbones and CHO or Br functional groups, and that the conjugation length plays more subtle role. Conversely, the calculated T_2 energy level for every molecule is lower than its S_1 level, which would favor the intersystem crossing if this process was solely controlled by the singlet-to-triplet energy difference. To complete the assessment, however, we need to account for the spin orbit coupling strength, as discussed below.

5.4.2. Spin orbit coupling (SOC) matrix elements and ISC rate

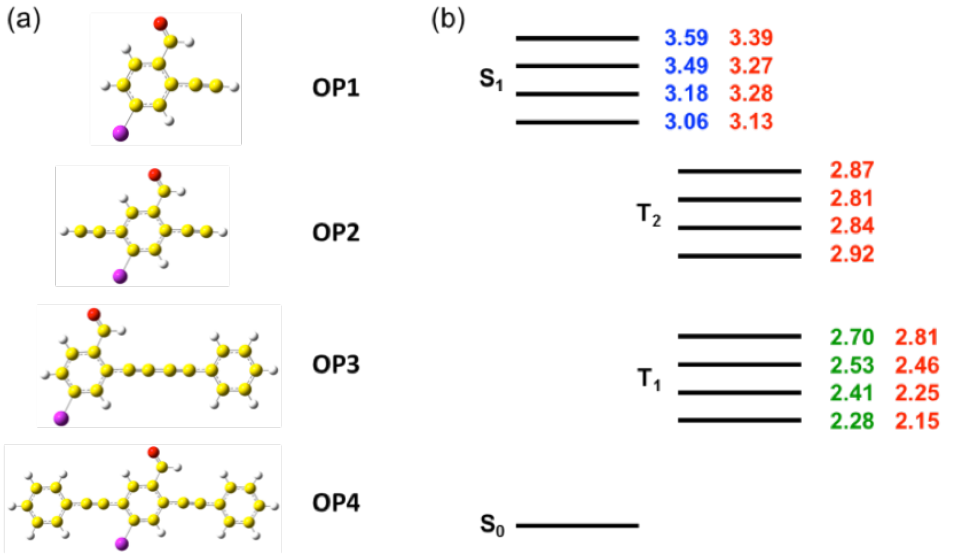

Figure 5.3. (a) Chemical structure of organic phosphors. (yellow) carbon (white) hydrogen (red) oxygen (purple) bromine; (b) Excited energy levels relative to the corresponding ground state energy level for OP1 to OP4 in the top-down order; blue: experimental data measured by UV absorption; green: experimental data measured by max. PL emission; red: calculated data by TDDFT calculation.

Perturbation theory suggests that for the transition between spin states to occur efficiently the energy difference between the two states must be small.[37] Therefore, based on the energy level diagrams of Figure 5.3, given that injected electrons predominantly create S_1 singlet states, the ISC can occur from S_1 to T_1 or from S_1 to T_2. TDDFT based methods are used to calculate the ISC rate constants for comparison with experimental findings. In Table 5.2 we show the SOC matrix elements for the $S_1 \rightarrow T_1$ and $S_1 \rightarrow T_2$ transitions. We use x, y, z to represent different polarizations of the spin orbit coupling, which leads to differently polarized light when electrons are quenched from triplet to ground states.[38] As we can see, the $S_1 \rightarrow T_1$ coupling is more than an order of magnitude

stronger than the $S_1 \rightarrow T_2$ coupling, yielding mainly the x- and y-polarized light for the phosphorescence emission.

The ISC rate is then calculated using equation 5.13. To obtain the total rate constant, we add the contributions from all three polarization directions. Figure 5.4(a) shows the rate constants for $S_1 \rightarrow T_1$ and $S_1 \rightarrow T_2$ transitions plotted versus the type of molecule in the order of increasing conjugation length. We also calculated a dimensionless factor

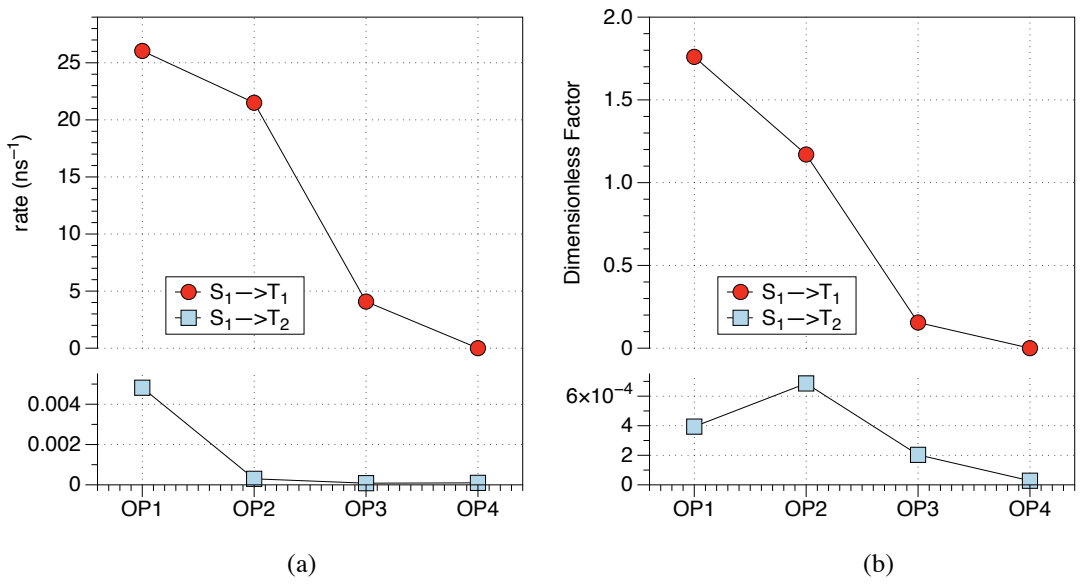

(a) (b)

Figure 5.4. (a) The rate constants (ns^{-1}) of intersystem crossing for $S_1 \rightarrow T_1$ and $S_1 \rightarrow T_2$ transitions calculated using equation 5.13; (b) The dimensionless factor ($*10^{-5}$) contributing to rate constants calculated using equation 5.11.

contributing to ISC rate constants according to equation 5.11, as shown in the Figure 5.4(b). First, we observe that the intersystem crossing rate for $S_1 \rightarrow T_1$ is much larger than that for $S_1 \rightarrow T_2$ (Note the different scales for the rates of the two processes). The dominant factor for this behavior is the large discrepancy in SOC between the two transitions, compared to the slight change in the energy difference. This finding strongly

suggests that, at least at low temperatures, the phosphorescence efficiency is mostly determined by the $S_1 \rightarrow T_1$ ISC rate. Secondly, our simulation results perfectly parallel the experimentally observed dependence of phosphorescence efficiency on the conjugation length, in that the $S_1 \rightarrow T_1$ ISC rate decreases as the conjugation length increases from OP1 to OP4. Hence, the additional insight derived from simulations implies that increasing conjugation compromises the phosphorescence efficiency by slowing down the dominant $S_1 \rightarrow T_1$ ISC process. We also noticed that the $S_1 \rightarrow T_1$ rate of OP3 and OP4 has been much lower than the first two molecules. This is perfectly consistent with the much weakened emission spectrum of OP3 and OP4, as shown in Figure 5.2(b). Finally, comparison of the ISC rate from equation 5.13 and the dimensionless factor from equation 5.11, as shown in Figure 5.4(b), demonstrates that the Franck Condon effect is not as influential as the spin-orbit coupling and energy difference in our study, because both quantities exhibit the same trend as a function of the conjugation length.

5.4.3. Steric aspects of ISC

To further investigate the mechanism by which conjugation length affects the ISC process, we calculated the electron densities surrounding the molecular constituents for the ground state and for different excited states of the four molecules under consideration. The electron density of the ground state serves as a reference, and by subtracting it from that of the excited states, we obtain the electron density difference that pinpoints the locations populated by electrons as a direct consequence of the excitation. For this spatially resolved electron density difference to be meaningful, we must ascertain that the geometries of the molecules do not change significantly between the ground and excited

states. Indeed, upon optimizing the atomic positions of the molecules in their excited states atoms shift from their ground state positions by less than 0.4Å for all molecules as shown in Figure 5.5.

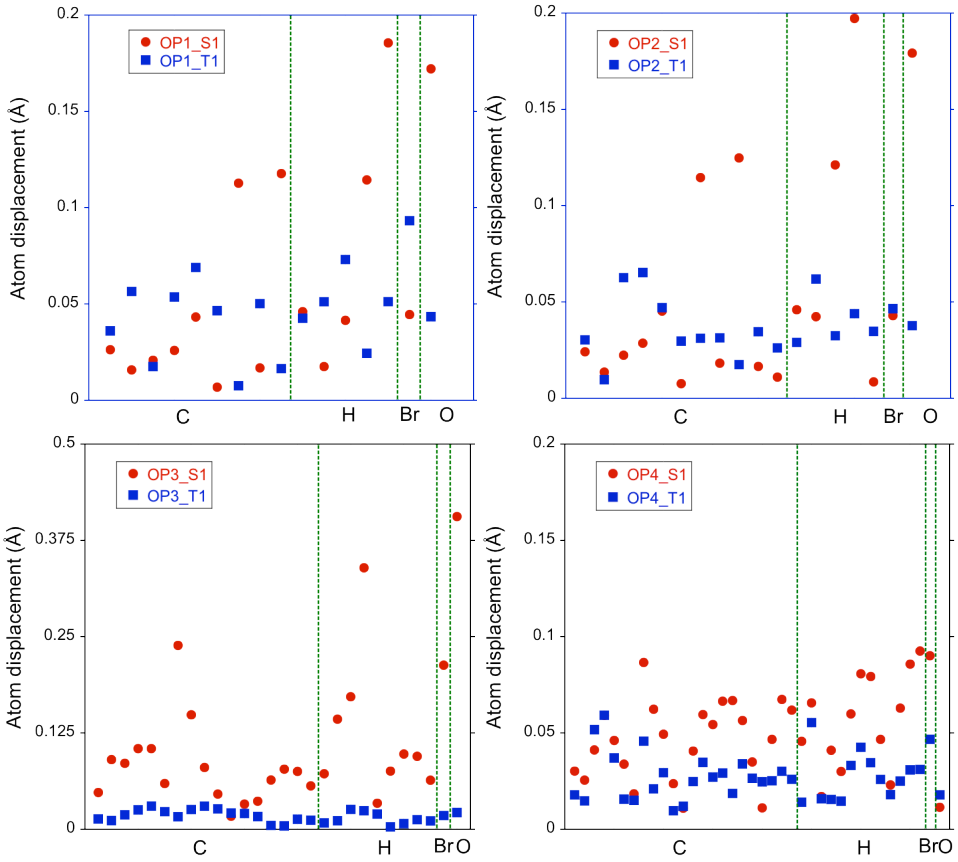

Figure 5.5. The atom displacements of OP1-OP4 between excited states (S_1, T_1) and ground state (S_0). The x-axis is divided into four regions, each containing the same atom type.

Figure 5.6 shows the electron density differences for the $S_0 \rightarrow S_1$ and $S_0 \rightarrow T_1$ transitions. Two different iso-density surfaces are shown to provide a measure for the spatial definition of the charge distribution. The blue color depicts regions with a net gain in electron density upon transition, whereas pink identifies regions that incur an electron density loss. For the $S_0 \rightarrow S_1$ transition at the lower iso-density value, a distinctly large singlet-populated space can be identified around the CHO functional group and to a small

extent, singlets are manifest in other region on the conjugation backbone. Conversely, at the higher iso-density value, the singlets appear only on the CHO functional group.

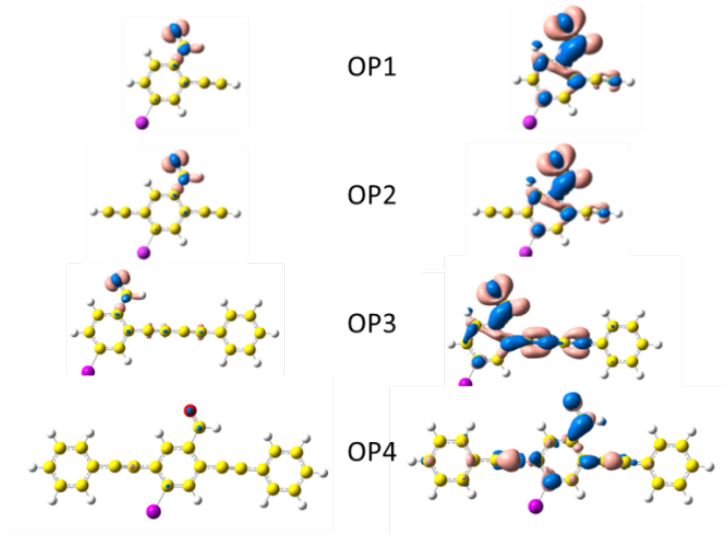

Figure 5.6. Plot of the total electron density difference between ground state and excited states, isovalue is in the unit of electrons/Å^3 (a) $S_0 \rightarrow S_1$, left: isovalue = 0.01, right: isovalue = 0.002 (b) $S_0 \rightarrow T_1$, left: isovalue = 0.01, right: isovalue = 0.002. The pink represents where loses electrons during the transition, and the blue represents where gains the electrons during the transition.

From this comparison we conclude that the singlet excited states are strongly localized on CHO functional groups, and this is consistently the case for all four molecules. Carrying out the same analysis for the $S_0 \rightarrow T_1$ transition, on the other hand, we find excited electrons evenly distributed over the conjugated backbone, for both low and high iso-density values, which means that the T_1 excited state is delocalized. Importantly, the degree of delocalization is stronger as the conjugation length gets longer. Delocalization is most pronounced in OP4, where the triplet population is spread over the entire conjugation backbone. Hence, while the singlet states remain localized regardless of the conjugation length, triplet states become increasingly delocalized with growing conjugation length. Consequently, for large conjugation lengths orbitals that host electrons excited into triplet states are spatially further removed from those that host electrons in the singlet state, leading to reduced spin orbit coupling strength and thus low ISC rates and resulting low phosphorescence emission efficiency. This finding can explain our experimental results, and indeed, is consistent with observations for other molecular systems reported in the literature.[24]

The conjugation length effect is more extensively studied using different kinds of functional groups such as hexyloxy and acetylene moieties to vary the conjugation length of bromobenzaldehyde derivatives (See Appendix A). Our data implies that extended conjugation causes red-shifted phosphorescence with decreased intensity and it is also attributed to decreased S_1 to T_1 ISC rate calculated using equation 5.11 and 5.13 in the same way as with the previous molecule set. The total electron density difference shows that singlet excited states are localized on the aldehyde group while triplet states are delocalized along the conjugated backbone. This finding implies that our hypothesis is

generally applied regardless of polarity effect from different functional groups such as hexyloxy, acetylene, and benzene ring.

5.5. Conclusions

We explored a series of purely organic phosphors for which the conjugation length is systematically varied. We found that the phosphorescence efficiency decreases and the emission color is red-shifted with increasing conjugation length. These observations are interpreted based on results from first-principles electronic structure calculations. The ISC rates are dominated by the SOC strength and not by the energy difference between lowest lying singlet and triplet states. Computations revealed that the $S_1 \rightarrow T_1$ transition rate is the highest for all molecules. Furthermore, while the singlet state remains localized for all molecules, the triplet state becomes progressively more delocalized with increasing conjugation length in the molecule. The ensuing spatial separation between singlet and triplet orbitals in molecules with longer conjugation length reduces the SOC strength and consequently the $S_1 \rightarrow T_1$ ISC rate. In combination, our findings also revealed that the ISC rate determines the phosphorescence efficiency in these molecules.

Table 5.1 Vibrational frequencies ω and Huang-Rhys factors S for $S_1 \rightarrow T_1$ and $S_1 \rightarrow T_2$ transitions for OP1-OP4.

OP1($S_1 \rightarrow T_1$)				OP1($S_1 \rightarrow T_2$)			
S_1		**T_1**		**S_1**		**T_2**	
$\omega(cm^{-1})$	**S**	**$\omega(cm^{-1})$**	**S**	**$\omega(cm^{-1})$**	**S**	**$\omega(cm^{-1})$**	**S**
119	0.363	111	1.479	119	0.355	98	1.294
150	1.721	144	0.056	150	1.734	144	0.004
298	0.216	259	0.019	252	0.001	258	0.026
438	0.168	300	0.039	298	0.218	298	0.027
461	0.073	431	0.030	438	0.166	428	0.060
634	0.067	453	0.106	461	0.073	454	0.117
672	0.002	603	0.117	634	0.069	602	0.107
771	0.470	622	0.067	672	0.002	620	0.091
864	0.019	659	0.003	771	0.471	723	0.346
1079	0.071	725	0.406	864	0.020	872	0.008
1111	0.041	871	0.008	1079	0.071	993	0.094
1169	0.002	996	0.092	1111	0.040	1088	0.121
1212	0.227	1076	0.170	1169	0.002	1154	0.031
1232	0.172	1142	0.024	1212	0.226	1194	0.036
1289	0.014	1197	0.015	1232	0.168	1211	0.080
1422	0.139	1214	0.104	1289	0.014	1251	0.021
1450	0.280	1252	0.037	1422	0.138	1304	0.058
1504	0.075	1305	0.070	1450	0.276	1405	0.001
1562	0.160	1399	0.032	1504	0.074	1455	0.293
1611	0.008	1433	0.337	1562	0.156	1475	0.064
2172	0.066	1477	0.047	1611	0.007	1545	0.108
2904	0.003	1528	0.055	2172	0.065	1630	0.006
3485	0.001	2091	0.060	2904	0.002	2103	0.071
		2971	0.001	3485	0.001	2987	0.001
		3477	0.001			3477	0.001
OP2($S_1 \rightarrow T_1$)				OP2($S_1 \rightarrow T_2$)			
S_1		**T_1**		**S_1**		**T_2**	
$\omega(cm^{-1})$	**S**	**$\omega(cm^{-1})$**	**S**	**$\omega(cm^{-1})$**	**S**	**$\omega(cm^{-1})$**	**S**
52	0.073	33	0.003	52	0.064	70	0.138
100	0.170	93	3.223	100	0.147	139	0.198
118	0.452	118	0.001	118	0.448	142	1.450
119	0.255	121	0.212	119	0.256	150	0.110
149	0.933	126	0.045	149	0.936	186	1.145
167	0.147	161	1.146	167	0.129	247	0.615
226	0.033	165	0.005	226	0.028	304	0.002
247	0.202	211	0.001	247	0.204	327	0.563
291	0.396	245	0.198	291	0.398	394	0.037
308	0.061	270	0.555	308	0.051	410	0.983
376	0.249	287	0.442	376	0.203	426	0.027
389	0.152	335	0.712	389	0.151	456	0.001
440	0.025	382	0.129	440	0.025	502	0.041
505	0.076	432	0.024	505	0.239	516	0.041
522	0.010	434	0.010	522	0.011	561	0.003
526	0.088	444	0.010	526	0.013	576	0.022
594	0.043	554	0.035	594	0.043	583	0.349
597	0.001	572	0.537	597	0.001	627	0.293
647	0.044	588	0.080	647	0.021	654	1.350

648	0.057	616	0.003	648	0.057	659	0.416
672	0.052	630	0.016	672	0.051	674	0.114
690	0.168	647	0.211	690	0.168	724	0.087
716	0.001	660	0.122	785	0.001	756	0.086
785	0.001	672	0.235	788	0.218	906	0.004
788	0.218	802	0.237	996	0.029	914	0.028
925	0.001	884	0.007	1130	0.075	937	0.056
996	0.029	930	0.004	1176	0.012	1055	0.003
1130	0.075	946	0.043	1206	0.038	1101	0.314
1176	0.012	1070	0.031	1236	0.447	1132	0.013
1206	0.038	1082	0.420	1275	0.270	1239	0.172
1236	0.448	1208	0.024	1339	0.023	1250	0.004
1275	0.269	1264	0.153	1380	0.042	1295	0.162
1339	0.023	1305	0.093	1441	0.458	1368	0.020
1380	0.042	1369	0.001	1495	0.010	1425	0.075
1441	0.462	1437	0.260	1557	0.231	1510	0.138
1495	0.010	1481	0.554	1590	0.858	1562	1.007
1557	0.232	1543	0.265	2168	0.059	1656	0.067
1590	0.854	1731	0.197	2227	0.098	2085	0.027
2168	0.059	1857	0.024	2898	0.003	2159	0.099
2227	0.097	2003	0.104	3485	0.001	2930	0.001
2898	0.003	2970	0.003	3490	0.002	3205	0.001
3485	0.001	3475	0.001			3480	0.001
3490	0.002						
OP3($S_1 \rightarrow T_1$)				OP3($S_1 \rightarrow T_2$)			
S_1		**T_1**		**S_1**		**T_2**	
ω(cm^{-1})	**S**	**ω(cm^{-1})**	**S**	**ω(cm^{-1})**	**S**	**ω(cm^{-1})**	**S**
21	1.616	20	1.514	21	0.070	21	0.070
66	0.809	60	0.622	66	0.037	66	0.036
127	0.972	136	1.064	127	0.112	128	0.108
183	0.422	179	0.473	183	0.040	184	0.040
227	0.232	232	0.106	227	0.005	225	0.002
269	0.044	263	0.067	269	0.001	268	0.002
293	0.224	298	0.915	293	0.068	298	0.076
413	0.021	415	0.006	413	0.001	416	0.006
471	0.075	472	0.047	471	0.012	470	0.011
500	0.007	480	0.004	632	0.004	631	0.008
636	0.013	546	0.003	636	0.020	636	0.014
653	0.019	599	0.078	682	0.007	684	0.006
682	0.041	644	0.005	776	0.002	778	0.004
845	0.005	691	0.106	1002	0.007	1003	0.003
1002	0.072	790	0.100	1009	0.001	1086	0.003
1009	0.073	847	0.244	1052	0.013	1118	0.024
1052	0.106	963	0.040	1058	0.021	1172	0.010
1058	0.248	1004	0.013	1073	0.004	1205	0.001
1073	0.012	1102	0.063	1167	0.001	1211	0.047
1167	0.055	1151	0.021	1219	0.021	1228	0.001
1206	0.022	1187	0.066	1298	0.010	1291	0.005
1219	0.073	1220	0.029	1339	0.003	1326	0.002
1234	0.144	1277	0.215	1381	0.004	1379	0.004
1298	0.002	1331	0.041	1385	0.010	1425	0.025
1339	0.004	1350	0.015	1507	0.001	1457	0.007
1381	0.413	1402	0.047	1603	0.004	1519	0.002

1385	0.227	1448	0.179	2097	0.002	1530	0.013
1457	0.003	1472	0.019	2810	0.005	1537	0.001
1500	0.017	1512	0.026			2200	0.006
1507	0.276	1539	0.017			2258	0.006
1536	0.004	1544	0.064			3023	0.002
1603	0.009	1584	0.061				
1647	0.023	1735	0.004				
2097	0.048	1881	0.008				
2189	0.071	2021	0.439				
2810	0.045	2958	0.001				
OP4($S_1 \rightarrow T_1$)				OP4($S_1 \rightarrow T_2$)			
S_1		**T_1**		**S_1**		**T_2**	
$\omega(cm^{-1})$	**S**	**$\omega(cm^{-1})$**	**S**	**$\omega(cm^{-1})$**	**S**	**$\omega(cm^{-1})$**	**S**
16	0.029	18	0.026	16	0.028	17	0.047
32	0.143	33	0.159	32	0.434	33	0.410
106	0.004	107	0.005	106	0.074	106	0.065
111	0.001	111	0.001	111	0.062	112	0.052
142	0.035	142	0.038	142	0.172	145	0.155
166	0.043	167	0.049	166	0.211	162	0.303
243	0.002	242	0.003	243	0.055	245	0.032
275	0.043	276	0.045	275	0.149	277	0.158
350	0.001	411	0.001	350	0.015	348	0.016
413	0.002	498	0.001	413	0.019	406	0.017
495	0.001	550	0.001	495	0.014	495	0.025
526	0.001	603	0.002	511	0.016	517	0.028
546	0.001	628	0.002	526	0.021	533	0.035
607	0.004	641	0.049	546	0.029	642	0.006
630	0.002	656	0.010	625	0.001	669	0.002
642	0.031	742	0.003	630	0.001	739	0.004
665	0.017	805	0.011	642	0.007	789	0.015
742	0.003	854	0.003	665	0.006	827	0.004
810	0.013	963	0.001	742	0.002	950	0.031
865	0.001	1002	0.004	810	0.008	963	0.062
990	0.001	1076	0.003	990	0.058	1027	0.001
1004	0.001	1134	0.005	1004	0.009	1116	0.002
1009	0.001	1161	0.071	1009	0.015	1171	0.005
1123	0.033	1199	0.008	1043	0.003	1181	0.015
1151	0.004	1200	0.007	1123	0.007	1250	0.001
1185	0.044	1212	0.009	1151	0.010	1315	0.002
1187	0.001	1423	0.040	1185	0.001	1320	0.004
1202	0.003	1439	0.002	1202	0.004	1362	0.008
1208	0.009	1445	0.002	1208	0.018	1397	0.025
1250	0.029	1505	0.053	1312	0.001	1413	0.001
1312	0.003	1520	0.010	1321	0.004	1474	0.006
1323	0.001	1531	0.002	1323	0.003	1499	0.008
1326	0.001	1558	0.132	1326	0.006	1516	0.008
1400	0.076	1583	0.001	1400	0.003	1562	0.002
1411	0.018	1584	0.032	1404	0.016	1590	0.075
1478	0.018	1617	0.007	1411	0.023	1706	0.007
1479	0.004	1751	0.005	1454	0.010	2188	0.004
1481	0.086	1926	0.010	1481	0.001	2471	0.047
1494	0.018	2138	0.039	1494	0.016		
1527	0.009			1527	0.008		

1533	0.009			1533	0.002		
1643	0.005			1629	0.023		
1681	0.003			1643	0.052		
2178	0.003			1681	0.019		
2244	0.026			2178	0.004		
				2244	0.004		

Table 5.2 Spin orbit coupling (SOC) matrix elements (10^{-5}*a.u.) for $S_1 \rightarrow T_1$ and $S_1 \rightarrow T_2$ transition in different polarization directions.

	$\langle S_1 \lvert H_{SO}^k \rvert T_1 \rangle_{k=x,y,z}$			$\langle S_1 \lvert H_{SO}^k \rvert T_2 \rangle_{k=x,y,z}$		
	x	y	z	x	y	z
OP1	1.6	-8.8	0	0	0	-0.12
OP2	3.1	9.7	0	0	0	0.14
OP3	4.69	-0.665	0	-0.002	0	-0.073
OP4	0	0	-0.006	0	0	0.013

5.6. References

1. Adachi, C., Baldo, M. A., Forrest, S. R. & Thompson, M. E. High-efficiency organic electrophosphorescent devices with tris(2-phenylpyridine)iridium doped into electron-transporting materials. *Appl. Phys. Lett.* **77**, 904-906 (2000).
2. Baldo, M. A. et al. Highly efficient phosphorescent emission from organic electroluminescent devices. *Nature* **395**, 151-154 (1998).
3. TANG, C. W. & VANSLYKE, S. A. ORGANIC ELECTROLUMINESCENT DIODES. *Appl. Phys. Lett.* **51**, 913-915 (1987).
4. You, Y. et al. Phosphorescent Sensor for Robust Quantification of Copper(II) Ion. *J. Am. Chem. Soc.* **133**, 11488-11491 (2011).
5. Kawamura, Y., Yanagida, S. & Forrest, S. R. Energy transfer in polymer electrophosphorescent light emitting devices with single and multiple doped luminescent layers. *J. Appl. Phys.* **92**, 87-93 (2002).
6. Sivasubramaniam, V. et al. Fluorine cleavage of the light blue heteroleptic triplet emitter FIrpic. *J. Fluor. Chem.* **130**, 640-649 (2009).
7. Kohler, A., Wilson, J. S. & Friend, R. H. Fluorescence and phosphorescence in organic materials. *Adv. Mater.* **14**, 701-707 (2002).
8. Turro, N. J. *Modern molecular photochemistry* (University Science Books, 1991).
9. KIRITANI, M., YOSHII, T., HIROTA, N. & BABA, M. INTRAMOLECULAR RADIATIONLESS TRANSITIONS IN SUBSTITUTED BENZALDEHYDES. *J. Phys. Chem.* **98**, 11265-11268 (1994).
10. SCHULMAN, E. M. & WALLING, C. PHOSPHORESCENCE OF ADSORBED IONIC ORGANIC-MOLECULES AT ROOM-TEMPERATURE. *Science* **178**, 53-5& (1972).
11. LOVE, L. J. C., SKRILEC, M. & HABARTA, J. G. ANALYSIS BY MICELLE-STABILIZED ROOM-TEMPERATURE PHOSPHORESCENCE IN SOLUTION. *Anal. Chem.* **52**, 754-759 (1980).
12. Mitchell, C. A., Gurney, R. W., Jang, S. H. & Kahr, B. On the mechanism of matrix-assisted room temperature phosphorescence. *J. Am. Chem. Soc.* **120**, 9726-9727 (1998).
13. Kahr, B. & Gurney, R. W. Dyeing crystals. *Chem. Rev.* **101**, 893-951 (2001).
14. Kabe, R., Lynch, V. M. & Anzenbacher, P., Jr. Enhanced phosphorescence in dibenzophosphole chalcogenide mixed crystal. *Crystengcomm* **13**, 5423-5427 (2011).
15. Yuan, W. Z. et al. Crystallization-Induced Phosphorescence of Pure Organic Luminogens at Room Temperature. *J. Phys. Chem. C* **114**, 6090-6099 (2010).
16. Maity, S. K., Bera, S., Paikar, A., Pramanik, A. & Haldar, D. Halogen bond induced phosphorescence of capped gamma-amino acid in the solid state. *Chem. Commun.* **49**, 9051-9053 (2013).
17. Bolton, O., Lee, K., Kim, H.-J., Lin, K. Y. & Kim, J. Activating efficient phosphorescence from purely organic materials by crystal design. *Nat. Chem.* **3**, 205-210 (2011).
18. Al-Attar, H. A. & Monkman, A. P. Room-Temperature Phosphorescence From Films of Isolated Water-Soluble Conjugated Polymers in Hydrogen-Bonded Matrices. *Adv. Funct. Mater.* **22**, 3824-3832 (2012).
19. Yong, G., She, W. & Zhang, Y. Room-temperature phosphorescence in solution

and in solid state from purely organic dyes. *Dyes Pigment.* **95**, 161-167 (2012).
20. Gahlaut, R. et al. Luminescence characteristics and room temperature phosphorescence of naphthoic acids in polymers. *J. Lumines.* **138**, 122-128 (2013).
21. Lee, D. et al. Room Temperature Phosphorescence of Metal-Free Organic Materials in Amorphous Polymer Matrices. *J. Am. Chem. Soc.* **135**, 6325-6329 (2013).
22. Kwon, M. S., Lee, D., Seo, S., Jung, J. & Kim, J. Tailoring Intermolecular Interactions for Efficient Room-Temperature Phosphorescence from Purely Organic Materials in Amorphous Polymer Matrices. *Angew. Chem.-Int. Edit.* **53**, 11177-11181 (2014).
23. Hirata, S. et al. Efficient Persistent Room Temperature Phosphorescence in Organic Amorphous Materials under Ambient Conditions. *Adv. Funct. Mater.* **23**, 3386-3397 (2013).
24. Rogers, J. E., Cooper, T. M., Fleitz, P. A., Glass, D. J. & McLean, D. G. Photophysical characterization of a series of platinum(II)-containing phenyl-ethynyl oligomers. *J. Phys. Chem. A* **106**, 10108-10115 (2002).
25. Jones, S. C. et al. Delocalization in platinum-alkynyl systems: A metal-bridged organic mixed-valence compound. *J. Am. Chem. Soc.* **126**, 11782-11783 (2004).
26. Chen, Y. L. et al. Switching luminescent properties in osmium-based beta-diketonate complexes. *ChemPhysChem* **6**, 2012-2017 (2005).
27. Beljonne, D., Shuai, Z., Pourtois, G. & Bredas, J. L. Spin-orbit coupling and intersystem crossing in conjugated polymers: A configuration interaction description. *J. Phys. Chem. A* **105**, 3899-3907 (2001).
28. Lin, S. H. et al. Ultrafast dynamics and spectroscopy of bacterial photosynthetic reaction centers. **121**, 1-88 (2002).
29. Peng, Q., Niu, Y., Shi, Q., Gao, X. & Shuai, Z. Correlation Function Formalism for Triplet Excited State Decay: Combined Spin-Orbit and Nonadiabatic Couplings. *J. Chem. Theory Comput.* **9**, 1132-1143 (2013).
30. Nan, G., Yang, X., Wang, L., Shuai, Z. & Zhao, Y. Nuclear tunneling effects of charge transport in rubrene, tetracene, and pentacene. *Phys. Rev. B* **79**, (2009).
31. Wang, L., Li, Q., Shuai, Z., Chen, L. & Shi, Q. Multiscale study of charge mobility of organic semiconductor with dynamic disorders. *Phys. Chem. Chem. Phys.* **12**, 3309-3314 (2010).
32. Frisch, M. J. et al. Gaussian 09. (2009).
33. Lu, T. & Chen, F. Multiwfn: A multifunctional wavefunction analyzer. *J. Comput. Chem.* **33**, 580-592 (2012).
34. Lu, T. & Chen, F. Quantitative analysis of molecular surface based on improved Marching Tetrahedra algorithm. *J. Mol. Graph.* **38**, 314-323 (2012).
35. Reimers, J. R. A practical method for the use of curvilinear coordinates in calculations of normal-mode-projected displacements and Duschinsky rotation matrices for large molecules. *J. Chem. Phys.* **115**, 9103-9109 (2001).
36. Aidas, K. et al. The Dalton quantum chemistry program system. *Wiley Interdiscip. Rev.-Comput. Mol. Sci.* **4**, 269-284 (2014).
37. Zhao, J., Wu, W., Sun, J. & Guo, S. Triplet photosensitizers: from molecular design to applications. *Chem. Soc. Rev.* **42**, 5323-5351 (2013).

38. Jansson, E., Minaev, B., Schrader, S. & Agren, H. Time-dependent density functional calculations of phosphorescence parameters for fac-tris(2-phenylpyridine) iridium. *Chem. Phys.* **333**, 157-167 (2007).

Chapter 6. Summary and outlook

6.1. Summary

In this thesis research, we explored the efficient molecular design principles for organic semiconductors by means of computational methods. We designed and predicted new molecular crystals for desired structural properties based on a number of computational methods, developed a multi-scale hopping model based on Fermi's golden rule to investigate charge transport in designed organic crystals, studied the energy level tuning mechanism in donor-acceptor conjugated polymers (CPs), and identified underlying principle of altered phosphorescence emission intensity with varied conjugation lengths.

In chapter 2, we design hybrid molecules by functionalizing a Octasilsesquioxanes (SQ_8) with one or two pentacene segments attached to the SQ_8 cage, yielding monopentacene-SQ_8 and dipentacene-SQ_8 . The purpose of this design is to change the pentacene packing from the celebrated herringbone pattern, i.e. the neighboring molecules forming V-shape, to a parallel configuration that facilitates carrier transfer. The predicted crystals, which are generated by the commercial package, Polymorph in Materials Studio, and further confirmed by other computational methods including molecular dynamics (MD) and density functional theory (DFT), indicate both hybrid molecules possess a parallel-pentacene configuration in which neighboring pentacene segments achieve better π-π stacking.

In chapter 3, in order to characterize the charge transport property in the designed crystals, we develop a hopping model based on Fermi's golden rule. According to this model, the charge transfer rate is mainly determined by charge transfer integral and intramolecular normal modes. The charge transfer integral characterizes the extent of orbital overlap between hopping sites. Our designed hybrid molecules tend to have a large charge transfer integral due to an enhanced π-π stacking, which is preferred for a higher charge transfer rate. Intramolecular normal modes are crucial to charge transport by incorporating the nuclear tunneling effect through electron-phonon coupling. After obtaining the charge transfer rate for a single hopping, kinetic Monte Carlo method is used to simulate the charge transport in crystals. The simulated hole mobility of pentacene crystal successfully reproduces the previous experimental result, confirming the reliability of our model. The simulated hole mobility in dipentacene-SQ_8 crystal is about two orders of magnitude larger than that in pentacene, reaching 11775 cm^2/Vs at 300K. However, the simulated hole mobility of monopentacene-SQ_8 does not show good enhancement of hole mobility compared to that in pentacene, which is mainly due to the 1-D bottleneck effect. Going forward, we investigate the thermal disorder effect in these crystals, in which we find quite different behaviors. For pentacene, it facilitates the formation of band-like behavior of hole mobility as well as the Marcus inverted region. For dipentacene-SQ8, it decreases the hole mobility in the most favored direction for hole hopping by balancing the probability of hole hopping in different directions; for monopentacene-SQ8 , it increases the hole mobility in the most favored direction for hole hopping by breaking the bottleneck effect. Overall, these simulation results confirm the succeed of the material design based on computational and modeling.

In chapter 4, we first study a series of synthesized CPs that are composed of a constant donor unit but different acceptor units. DFT calculations determine that the introduction of stronger acceptor unit lowers the LUMO level, but leaves the HOMO level almost unchanged, which is in good agreement with the previous experimental results. Further investigation on frontier orbital localization indicate that while the HOMO orbitals are ubiquitously delocalized for all CPs, LUMO orbitals become more localized when using a stronger acceptor unit. Moreover, a linear relationship is presented between the band gap of a CP polymer and the amount of intramolecular charge transfer. Based on the findings above, we then design another series of CPs that have a constant acceptor unit but different donor units. Conversely, we observe that the introduction of stronger donor unit increases the HOMO level but keeping the LUMO level almost unchanged. The frontier orbital analysis shows that the while LUMO orbitals are localized to the same extent for all CPs, HOMO orbital becomes more localized when using a stronger donor unit. Overall, the amount of intramolecular charge transfer for the synthesized CPs and the newly designed CPs shows a good linearity as a function of band gap.

In chapter 5, we explore a series of purely organic phosphors for which the conjugation length is systematically varied. It is found in experiments that with increasing conjugation length, the phosphorescence efficiency of these molecules decreases and the emission color is red-shifted. By using time-dependent density functional theory (TDDFT), we first obtain consistent results on the energy levels of excited states including S_1, T_1 and T_2 compared to the experimental data. Next, we aim to interpret the experimental findings by investigating the efficiency of intersystem crossing (ISC). A similar model based on Fermi's golden rule used in Chapter 3 is developed to quantify

the ISC rate for $S_1 \rightarrow T_1$ and $S_1 \rightarrow T_2$. Computations reveal that the $S_1 \rightarrow T_1$ transition rate is much higher than that $S_1 \rightarrow T_2$ of for all molecules. Moreover, we observe a decreased $S_1 \rightarrow T_1$ rate when increasing conjugation length. To further elucidate this phenomenon, we examine the excited states orbitals by TDDFT calculations. We observe that while the singlet state remains localized for all molecules, the triplet state becomes progressively more delocalized with increasing conjugation length in the molecule. The ensuing spatial separation between singlet and triplet orbitals in molecules with longer conjugation length reduces the spin orbit coupling strength and consequently the $S_1 \rightarrow T_1$ ISC rate. In combination, our findings also reveal that the ISC rate determines the phosphorescence efficiency in these molecules.

Overall, this thesis provides useful insights to computational modeling on a variety of optoelectronic properties and offers new directions for advanced molecule designs in organic semiconductors

6.2. Outlook

One possible extension from this thesis is to use hopping model to simulate the charge transport in amorphous and polycrystalline organic materials, which are the two main forms of thin films in experiments. Our hopping model can access the dependence of charge mobility on domain size, impurity/defects, temperature, and electric field (intensity and direction). Though complicated, a multi-variable study on the hopping process will give a more thorough picture on the factors limiting the charge mobility. As a result, we can provide solutions to tune the charge mobility by controlling experimental conditions for designing new materials.

On the other hand, our hopping model has its main detrimental drawback by neglecting the external polarization and the contributions of surrounding molecules and only assuming a hopping dimer model. Also, we simulate the hopping path of a single electron to represent the macroscopic charge transfer of many electrons. There is clearly still considerable work needed to better model charge transport in organic materials.

To design better metal-free organic phosphors, we need tackle the non-radiative conversion in which a large quantity of excitation energy is wasted through vibrational loss. In chapter 4, we have discussed many ways in literature to circumvent this issue by using complex supporting structures. However, evaluating this vibrational loss computationally remains a challenge.

Appendix A. Conjugation length effect for other organic phosphors

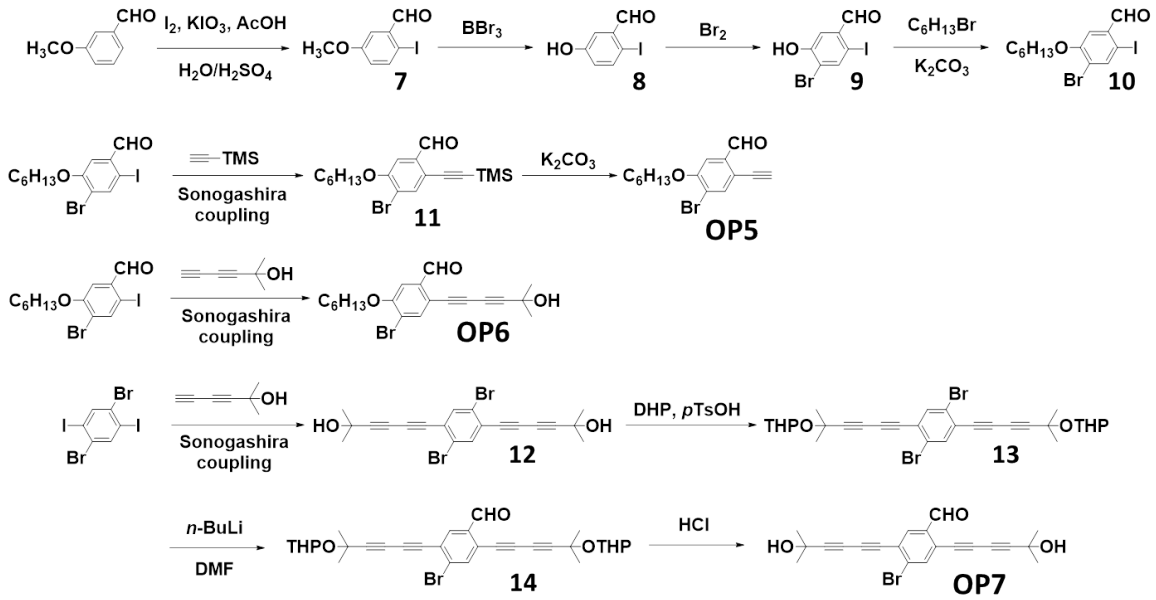

Figure A.1. Synthetic routes for organic phosphors with different functional groups.

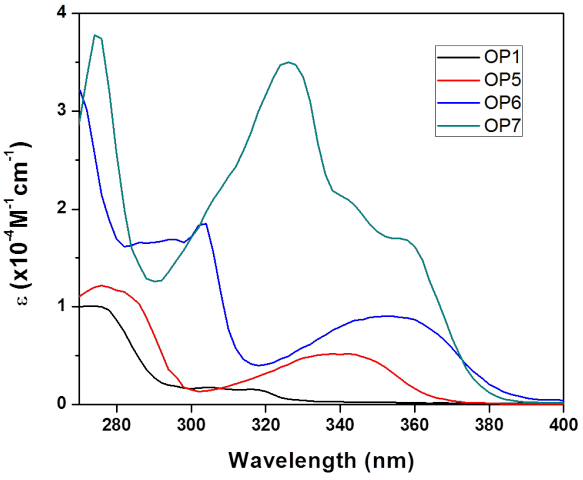

Figure A.2. UV absorption spectra for OP5-OP7 were measured in chloroform solution at room temperature and plotted with extinction coefficient.

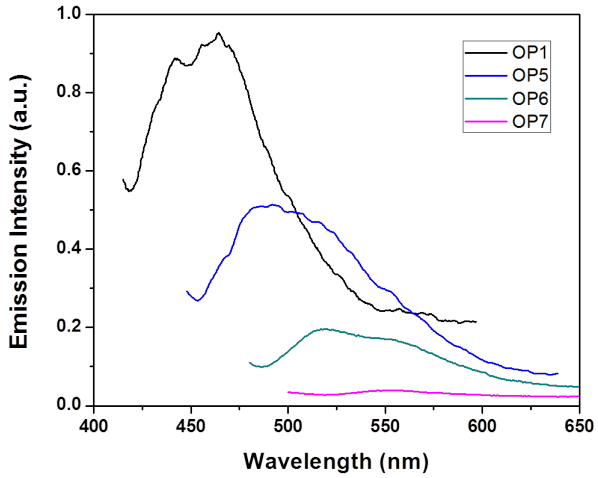

Figure A.3. Phosphorescence spectra were measured at 77 K with same absorbance. Each molecule was excited at 320, 350, 362, and 360 nm respectively.

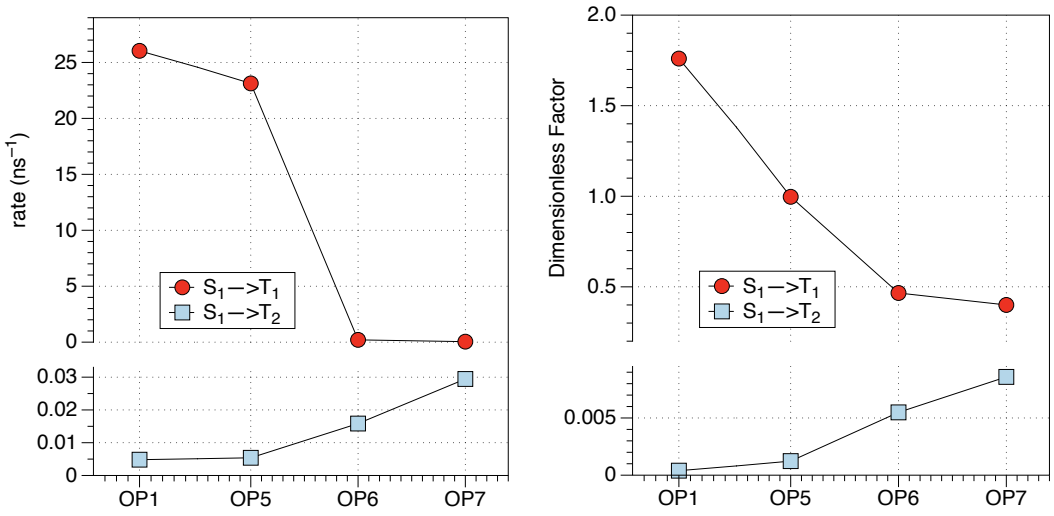

(a) (b)

Figure A.4. (a) The rate constants (ns^{-1}) of intersystem crossing for $S_1 \rightarrow T_1$ and $S_1 \rightarrow T_2$ transitions according to equation 5.13 (b) the dimensionless factor ($*10^{-5}$) contributing to rate constants according to equation 5.11.

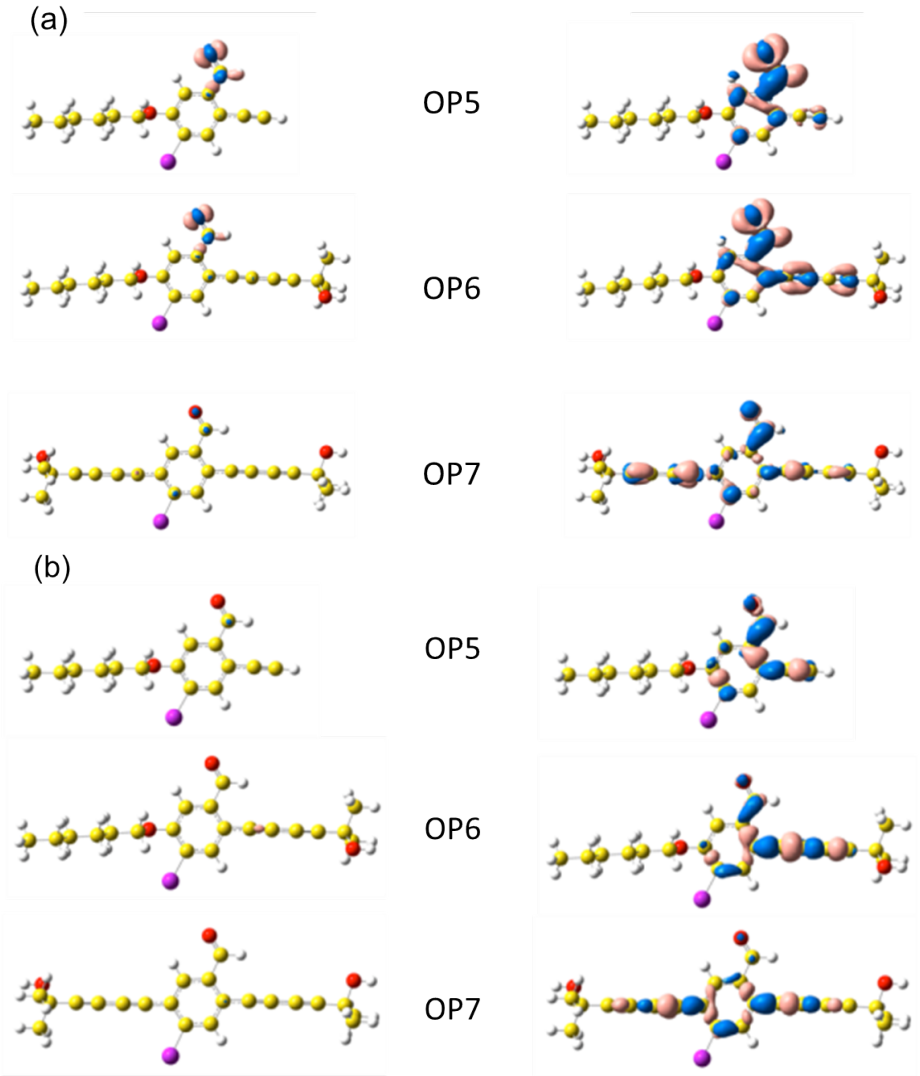

Figure A.5. Plot of the total electron density difference between ground state and excited states, isovalue is in the unit of electrons/Å^3 (a) $S_0 \rightarrow S_1$, left: isovalue = 0.01, right: isovalue = 0.002 (b) $S_0 \rightarrow T_1$, left: isovalue = 0.01, right: isovalue = 0.002. The pink represents where loses electrons during the transition, and the blue represents where gains the electrons during the transition.

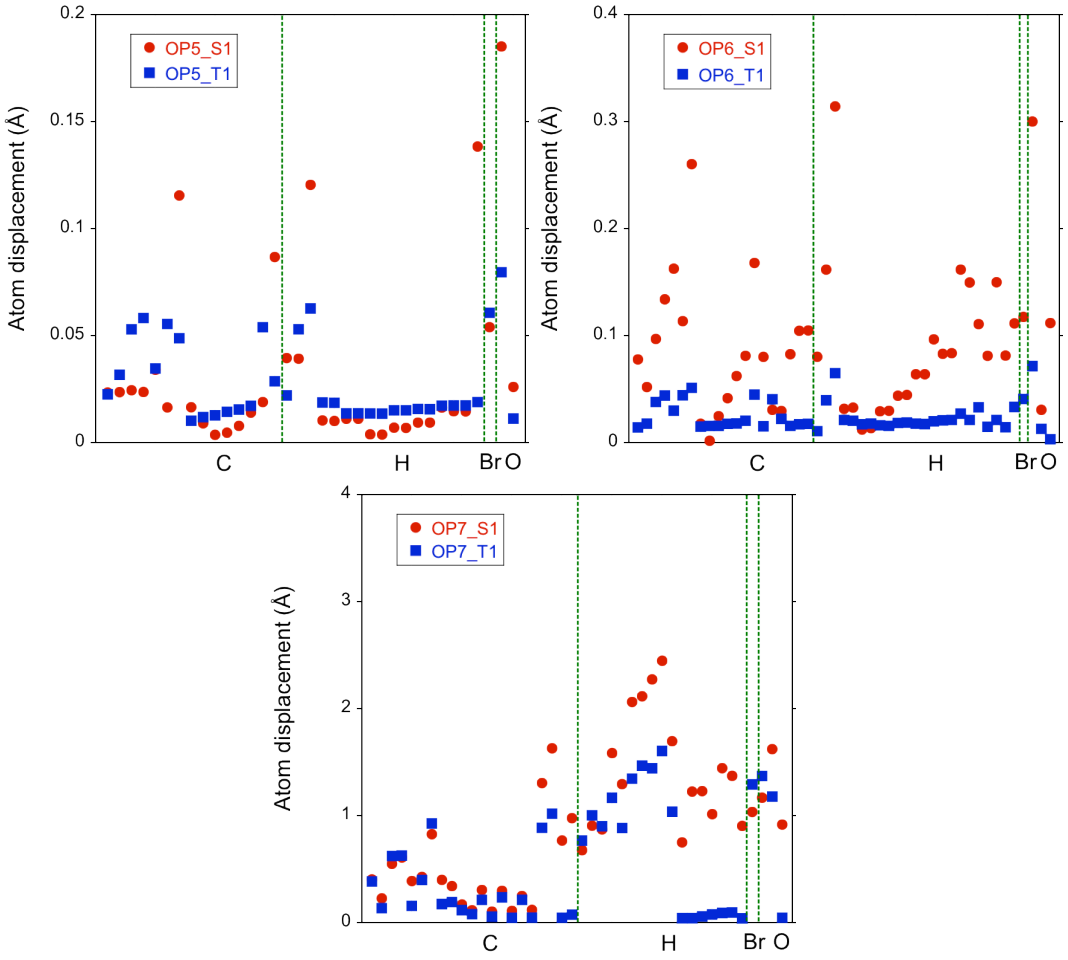

Figure A.6. The atom displacements of OP5-OP7 between excited states (S_1, T_1) and ground state (S_0). The x-axis is divided into four regions, each containing the same atom type.

Table A.1. SOC matrix elements (10^{-5}*a.u.) for $S_1 \rightarrow T_1$ and $S_1 \rightarrow T_2$ transition in different polarization directions for OP5-OP7.

	$\langle S_1 \lvert H_{SO}^k \rvert T_1 \rangle_{k=x,y,z}$			$\langle S_1 \lvert H_{SO}^k \rvert T_2 \rangle_{k=x,y,z}$		
	x	y	z	x	y	z
OP5	-7.4	4.8	0	0	0	0.20
OP6	-5.5	4.3	0.001	0.008	-0.001	0.31
OP7	-5.6	-4.6	0.053	0.28	0.066	-0.19

Table A.2. Vibrational frequencies ω and Huang-Rhys factors S for $S_1 \rightarrow T_1$ and $S_1 \rightarrow T_2$ transitions for OP5-OP7.

OP5($S_1 \rightarrow T_1$)				OP5($S_1 \rightarrow T_2$)			
S_1		**T_1**		**S_1**		**T_2**	
$\omega(cm^{-1})$	**S**	**$\omega(cm^{-1})$**	**S**	**$\omega(cm^{-1})$**	**S**	**$\omega(cm^{-1})$**	**S**
15	11.120	15	9.249	15	10.557	20	0.117
30	0.003	21	0.017	30	0.002	54	0.050
45	0.098	35	0.001	45	0.101	64	2.138
57	0.657	53	0.859	57	0.635	76	8.845
65	0.002	68	0.032	65	0.003	80	0.069
92	0.007	87	0.011	92	0.007	112	1.285
116	0.165	103	0.150	116	0.188	133	0.079
120	0.492	119	0.076	120	0.565	140	0.015
130	0.779	131	0.038	130	0.808	147	0.008
139	0.060	143	0.045	139	0.063	179	0.594
148	0.506	150	0.987	148	0.509	186	0.276
164	0.030	165	0.853	164	0.032	198	0.192
196	0.339	182	0.009	196	0.325	222	0.095
212	0.080	206	0.127	212	0.082	233	0.040
218	0.245	233	0.090	218	0.220	266	0.296
243	0.026	256	0.116	243	0.024	297	0.003
250	0.002	276	0.014	250	0.001	363	0.006
265	0.322	284	0.018	265	0.329	399	0.097
305	0.041	326	0.020	305	0.042	422	0.031
348	0.055	383	0.073	348	0.053	427	0.019
397	0.085	391	0.027	397	0.082	439	0.013
431	0.165	419	0.204	431	0.141	441	0.166
433	0.087	441	0.001	433	0.085	467	0.104
460	0.004	457	0.003	460	0.004	493	0.032
470	0.008	485	0.024	470	0.008	594	0.143
492	0.133	499	0.095	492	0.133	630	0.120
508	0.001	576	0.004	508	0.002	636	0.067
526	0.001	606	0.073	526	0.001	654	0.001
618	0.027	611	0.011	618	0.024	672	0.077
640	0.067	637	0.134	640	0.076	703	0.181
651	0.073	662	0.086	651	0.071	726	0.086
672	0.088	714	0.198	672	0.122	758	0.030
704	0.078	792	0.223	704	0.077	760	0.067
754	0.131	879	0.019	754	0.132	910	0.006
760	0.003	915	0.008	760	0.003	945	0.062
790	0.261	940	0.022	790	0.264	981	0.007
814	0.005	954	0.001	814	0.005	1021	0.001
907	0.003	981	0.001	907	0.003	1049	0.001
920	0.004	1013	0.015	920	0.004	1106	0.141
982	0.007	1016	0.071	982	0.007	1139	0.095
1013	0.001	1025	0.065	1013	0.001	1171	0.001
1019	0.008	1050	0.011	1019	0.008	1195	0.011
1044	0.005	1067	0.001	1044	0.004	1233	0.017
1053	0.001	1077	0.001	1053	0.001	1243	0.087
1132	0.082	1146	0.002	1132	0.081	1276	0.007
1147	0.001	1173	0.061	1147	0.001	1288	0.013
1179	0.009	1187	0.001	1179	0.009	1309	0.112

1196	0.003	1236	0.005	1196	0.003	1324	0.024
1207	0.126	1263	0.001	1207	0.128	1331	0.005
1235	0.008	1284	0.084	1235	0.008	1338	0.001
1262	0.021	1297	0.092	1262	0.021	1390	0.001
1265	0.140	1301	0.022	1265	0.139	1395	0.046
1272	0.230	1325	0.009	1272	0.229	1417	0.020
1289	0.006	1343	0.001	1289	0.006	1422	0.056
1321	0.001	1350	0.203	1321	0.001	1430	0.001
1334	0.001	1368	0.089	1334	0.001	1451	0.031
1380	0.044	1390	0.015	1380	0.045	1494	0.186
1391	0.003	1416	0.020	1391	0.003	1509	0.001
1429	0.001	1421	0.031	1429	0.001	1518	0.004
1434	0.023	1430	0.005	1434	0.024	1525	0.005
1459	0.467	1432	0.099	1459	0.469	1531	0.007
1506	0.043	1469	0.057	1506	0.044	1566	0.197
1536	0.001	1489	0.030	1536	0.001	1639	0.052
1555	0.167	1532	0.001	1555	0.167	2105	0.070
1608	0.099	1589	0.088	1608	0.098	2963	0.001
2174	0.082	1921	0.053	2174	0.086	3477	0.001
2911	0.002	2985	0.005	2911	0.002		
3485	0.003			3485	0.003		

OP6($S_1 \rightarrow T_1$)				OP6($S_1 \rightarrow T_2$)			
S_1		**T_1**		**S_1**		**T_2**	
ω(cm^{-1})	**S**	**ω(cm^{-1})**	**S**	**ω(cm^{-1})**	**S**	**ω(cm^{-1})**	**S**
4	1.702	8	2.581	4	0.061	10	0.084
10	1.379	11	0.076	10	0.008	12	0.814
13	1.003	19	1.615	13	0.001	17	0.088
16	0.690	25	0.614	16	0.793	26	0.296
25	0.491	35	0.004	25	0.137	31	0.153
38	0.006	39	0.001	45	0.026	40	0.031
45	0.007	51	0.017	56	0.002	53	0.028
56	0.029	60	0.026	63	0.001	62	0.026
63	0.008	74	0.010	83	0.067	87	0.082
83	0.318	79	0.401	88	0.005	90	0.148
88	0.166	96	0.050	107	0.026	105	0.143
107	0.239	122	0.158	121	0.006	119	0.189
121	0.023	138	0.278	132	0.385	123	0.003
132	1.309	141	1.374	137	0.051	137	0.002
137	0.086	148	0.001	164	0.001	165	0.002
164	0.027	165	0.071	166	0.003	167	0.001
166	0.390	182	0.106	189	0.086	185	0.002
189	0.667	189	0.538	194	0.001	197	0.043
194	0.039	203	0.091	226	0.043	207	0.004
207	0.025	218	0.080	239	0.002	230	0.031
226	0.016	236	0.003	251	0.001	236	0.003
239	0.001	240	0.006	253	0.005	241	0.001
251	0.002	280	0.211	288	0.004	256	0.001
253	0.005	283	0.199	310	0.008	258	0.003
261	0.001	290	0.384	380	0.020	287	0.001
280	0.001	322	0.010	405	0.006	377	0.006
288	0.079	355	0.016	417	0.015	382	0.007
310	0.099	377	0.132	426	0.003	406	0.003

334	0.007	397	0.020	461	0.002	436	0.012
363	0.016	401	0.091	468	0.003	454	0.004
380	0.048	404	0.011	472	0.004	470	0.002
405	0.019	455	0.001	536	0.001	540	0.001
417	0.038	470	0.002	541	0.003	562	0.001
426	0.011	497	0.035	607	0.002	610	0.009
461	0.008	515	0.002	622	0.019	625	0.024
468	0.314	577	0.015	630	0.044	626	0.022
487	0.007	598	0.018	769	0.014	683	0.004
536	0.010	609	0.252	820	0.003	766	0.008
541	0.002	616	0.150	864	0.002	865	0.003
607	0.085	623	0.202	1051	0.002	1061	0.010
630	0.058	634	0.133	1053	0.007	1092	0.008
687	0.024	689	0.098	1096	0.008	1154	0.001
731	0.001	737	0.296	1155	0.001	1250	0.005
749	0.011	759	0.002	1248	0.010	1272	0.005
759	0.002	812	0.001	1267	0.004	1302	0.001
769	0.335	858	0.267	1302	0.003	1379	0.001
864	0.206	902	0.008	1378	0.002	1390	0.001
883	0.005	925	0.003	1390	0.001	1409	0.012
903	0.010	935	0.002	1408	0.015	1417	0.001
926	0.003	955	0.012	1443	0.005	1448	0.005
960	0.024	959	0.017	1489	0.001	1504	0.001
977	0.001	1003	0.002	1519	0.009	1518	0.005
1016	0.001	1023	0.002	1525	0.008	1526	0.002
1024	0.005	1024	0.004	1602	0.006	1527	0.001
1041	0.002	1046	0.015	2125	0.068	1606	0.005
1053	0.018	1050	0.004	2228	0.058	2034	0.053
1096	0.541	1078	0.001	2820	0.008	2125	0.068
1147	0.001	1119	0.008			3011	0.010
1180	0.001	1145	0.005				
1192	0.002	1146	0.002				
1196	0.001	1176	0.341				
1199	0.005	1182	0.001				
1234	0.008	1195	0.013				
1248	0.178	1229	0.007				
1262	0.001	1248	0.011				
1267	0.014	1281	0.001				
1302	0.054	1290	0.001				
1320	0.001	1322	0.002				
1354	0.062	1386	0.008				
1378	0.075	1405	0.036				
1390	0.016	1417	0.005				
1408	0.264	1425	0.001				
1417	0.006	1427	0.001				
1433	0.007	1436	0.155				
1443	0.117	1451	0.010				
1489	0.011	1461	0.076				
1491	0.001	1488	0.025				
1500	0.002	1492	0.001				
1507	0.009	1500	0.002				
1509	0.002	1508	0.003				

1519	0.076	1509	0.004				
1525	0.066	1517	0.003				
1526	0.001	1523	0.024				
1534	0.001	1530	0.005				
1602	0.083	1546	0.088				
2125	0.085	1680	0.080				
2228	0.010	1884	0.365				
2820	0.020	1963	0.039				
3014	0.012	2960	0.005				
3016	0.001	3013	0.005				
3026	0.004	3017	0.001				
3037	0.002	3024	0.003				
3038	0.006	3027	0.006				
3045	0.002	3038	0.002				
3047	0.071	3038	0.006				
3124	0.068	3047	0.017				
3150	0.001	3047	0.058				
3227	0.001	3123	0.068				
		3152	0.001				
		3216	0.001				
		3228	0.001				
OP7($S_1 \rightarrow T_1$)				OP7($S_1 \rightarrow T_2$)			
S_1		**T_1**		**S_1**		**T_2**	
ω(cm^{-1})	**S**	**ω(cm^{-1})**	**S**	**ω(cm^{-1})**	**S**	**ω(cm^{-1})**	**S**
8	0.005	6	2.283	8	0.005	6	1.166
10	0.032	16	0.575	10	0.032	13	1.187
13	0.011	18	4.234	13	0.011	13	3.115
15	0.048	29	0.022	15	0.048	15	0.938
23	2.014	41	0.613	23	2.014	20	5.220
29	0.001	61	0.026	29	0.001	29	0.058
42	0.015	72	0.020	42	0.015	43	0.106
57	0.004	76	0.250	57	0.004	59	0.029
81	0.003	88	0.166	81	0.003	81	0.041
83	0.068	143	0.148	83	0.068	84	0.046
88	0.001	151	0.041	88	0.001	91	0.005
132	0.205	157	0.051	132	0.205	115	0.010
179	0.006	168	0.003	179	0.006	130	0.204
189	0.040	175	0.037	189	0.040	156	0.001
204	0.003	192	0.016	204	0.003	190	0.033
247	0.001	233	0.224	247	0.001	206	0.002
256	0.001	233	0.322	256	0.001	232	0.001
280	0.052	246	0.008	280	0.052	239	0.001
286	0.005	247	0.023	286	0.005	245	0.002
305	0.013	258	0.075	305	0.013	247	0.004
338	0.005	261	0.003	338	0.005	258	0.007
350	0.002	264	0.126	350	0.002	265	0.003
370	0.012	307	0.018	370	0.012	279	0.006
382	0.029	314	0.038	382	0.029	280	0.020
408	0.010	350	0.003	408	0.010	291	0.013
418	0.022	388	0.006	418	0.022	306	0.009
463	0.001	402	0.016	463	0.001	309	0.014
498	0.011	415	0.056	498	0.011	352	0.004

518	0.001	431	0.001	518	0.001	363	0.003
529	0.001	491	0.001	529	0.001	386	0.012
545	0.001	512	0.018	545	0.001	410	0.006
550	0.001	523	0.009	550	0.001	425	0.028
617	0.001	529	0.004	617	0.001	472	0.002
628	0.002	545	0.017	628	0.002	486	0.011
642	0.010	568	0.007	642	0.010	498	0.007
668	0.006	625	0.007	668	0.006	531	0.004
678	0.001	636	0.010	678	0.001	551	0.002
702	0.002	657	0.002	702	0.002	619	0.004
769	0.001	674	0.001	769	0.001	629	0.010
827	0.032	678	0.056	827	0.032	636	0.004
862	0.006	683	0.003	862	0.006	636	0.005
932	0.071	724	0.002	932	0.071	671	0.004
959	0.007	727	0.071	959	0.007	706	0.001
963	0.013	856	0.001	963	0.013	768	0.004
977	0.022	875	0.008	977	0.022	848	0.001
1022	0.001	927	0.003	1022	0.001	871	0.002
1072	0.021	963	0.001	1072	0.021	964	0.001
1078	0.004	985	0.018	1078	0.004	977	0.001
1158	0.001	1050	0.010	1158	0.001	1137	0.088
1218	0.008	1143	0.008	1218	0.008	1155	0.014
1294	0.001	1151	0.001	1294	0.001	1161	0.020
1331	0.028	1198	0.001	1331	0.028	1186	0.019
1350	0.002	1224	0.022	1350	0.002	1201	0.001
1364	0.008	1261	0.003	1364	0.008	1278	0.009
1386	0.007	1272	0.008	1386	0.007	1316	0.018
1418	0.003	1335	0.016	1418	0.003	1337	0.016
1426	0.003	1380	0.002	1426	0.003	1377	0.017
1447	0.003	1391	0.010	1447	0.003	1398	0.018
1470	0.007	1401	0.006	1470	0.007	1417	0.005
1501	0.002	1413	0.050	1501	0.002	1425	0.001
1590	0.021	1425	0.001	1590	0.021	1426	0.001
2743	0.002	1426	0.002	2743	0.002	1452	0.042
		1430	0.020			1502	0.001
		1435	0.002			1522	0.006
		1465	0.020			1523	0.002
		1519	0.050			1528	0.031
		1523	0.005			1588	0.012
		1880	0.023			2199	0.015
		2167	0.003			2288	0.021
		2196	0.003			3017	0.008
		3035	0.022				

Appendix B. Matlab code for kinetic Monte Carlo simulation

```
%%%% Constants and pre-defined variables %%%%
hbar=0.6582e-15;%Planck constant over 2 pi in eV s
k=8.617e-5;%Boltzmann constant in eV/K
DIS=2e5;%maximum distance for a trajectory, in Å
T=300;%temperature, in Kelvin
N_traj=500;%maximum trajectories studied
N_mol=32;%number of unique molecules in the simulation box
N_nei=6;%number of neighboring hopping sites for one molecule

box(:,:,1)=[3.353      -4.405  4.62]*4; %vector OA
box(:,:,2)=[20.184      -0.433  -2.723]*2; %vector OB
box(:,:,3)=[-4.045      15.317  5.171]*2; %vector OC
EF_Dir=box(:,:,1)/norm(box(:,:,1));
E_value=2e-5;
EF=EF_Dir*E_value; %electric field in V/Å along normalized OA

%cumulative ktot, next hopping site, x_diff, y_diff, z_diff,
count
for i=[1:N_mol]
    info(:,:,i)=zeros(N_nei,6);
end

%%%% KMC %%%%
fid=fopen('result.txt', 'a');% output file
m=zeros(N,1);
for=(1:N_traj),
    p=ceil(rand*N_mol);% determine the init position of carrier
    time=0; % cumulative time
    dis=0; % cumulative distance in terms of vector
    while dis < DIS
      r=rand;
      for j=(1:N_nei)
           if (info(N_nei,1,p)*r <= info(j,1,p)) break;
           end
      end
      time=time+1/info(N_nei,1,p);
      dis=dis+dot(info(j,3:5,p),EF_Dir);
      p=info(j,2,p);
    end
    m(traj)=dis/time/E_value*1e-16;  % in the units of cm^2/V*s
    fprintf(fid,'%8.4E\n', m(traj));
 end
```